UNIVERSITÀ
DEGLI STUDI
DI BRESCIA

DOTTORATO DI RICERCA IN TECHNOLOGY FOR HEALTH

ING-INF/07

XXXV Cycle

SENSORS DESIGN FOR E-SKIN BY PRINTED AND FLEXIBLE ELECTRONICS

Ph.D. Candidate:
Fapanni Tiziano

Supervisor: Mauro Serpelloni, University of Brescia

Abstract

In the modern era where the overall living conditions improve, the population increases and ages, the need for a new paradigm of smart healthcare is arising where the need to monitor and track the changes in the physiological status of patients or sports professionals represents the main objective of the scientific community. In this frame, e-skin devices, defined as flexible devices that embed arrays of sensors, are cutting-edge technology that is promising to monitor different physiological parameters from the human body in a non-invasive way thanks to their reduced size and bulkiness. Thanks to these characteristics, e-skins are promising in a plethora of applications and fields other than the clinical one such as the industrial environment and prosthesis. Their wide applicability is enabled by the vast amount of sensors that allow precise and distributed data collection. In this frame, sensors become central to transduce from the body the signals of interest such as temperatures, pressures, deformations, biopotentials and biochemical markers (e.g. ions, metabolites, heavy metals, amino acids, hormones, drugs...). This last class of markers is lately attracting huge interest from the scientific community since they allow the quick detection of a plethora of physiological conditions. Currently, biosensors are researched to detect those signals as they are valid, cheaper and easier to use than standard in-lab analysis methods (e.g ELISA protocols, chromatography, ...). Moreover, among the possible transduction principles currently employed for biosensors, the electrochemical one presents, according to the literature, many advantages such as low cost, high sensitivity and simple instrumentation. In this thesis, different approaches for the development and improvement of printed electrochemical sensors for e-skin application will be investigated. Exploiting the opportunities offered by novel printing technologies, such as Aerosol Jet Printing, the main focus was to improve the metrological characteristics as well as to evaluate, monitor and mitigate the uncertainty sources that could affect the devices. Before going into the experimental detail, the first part of the thesis will be dedicated to provide a description of the transducing principle behind the electorchemical measurements investigated. Further, literature will be deepened in order to expose the general concepts about e-skins and biosensors, including opportunities and limitations. Then, a prototype of a multi-sensing e-skin patch

for unobtrusive and personalized fatigue assessment, that uses both an 8-channel electromyographic (EMG) sensor and an electrochemical sensor, will be presented. As for the experimental frame, the achieved results were promising for both the kinds of sensors with EMG electrodes that are capable to monitor the changes of EMG features during fatigue processes. Regarding the electrochemical sensor, it consists in a lactate sensor, which can monitor the lactate concentration changes within the physiological range (10-100 mM) of interest for fatigue, presenting however sensitivities around 0.35 $\mu A \cdot mM^{-1}$ that are not completely satisfactory and thus have to be improved. Starting from these cues, the next two projects that will be presented are focused on the scientific evidence to try to improve the sensitivity and the limit of detection of printed electrochemical sensors using both micro- and nano- structures. The former solution explores aerosol jet printing as a means to achieve a micro-structuration towards the third dimension. The proposed process is able to achieve linear micro-structures that permit increasing the electrode/electrolyte surface area up to 130% without changing the substrate occupancy. These also showed that this solution increased the sensitivity of the electrodes, on average, by 2.3 times with respect to bare electrodes. Then a second approach that employs nano-structured allotropes of carbon as functionalization layers will be exposed. The two selected materials are multi-walled carbon nanotubes (CNT) and graphene as they are widespread in industry, relatively cheap and are suitable in electrochemistry. The different tests that were carried out aimed at detecting the stable potential window, the stability and the ability to detect hydrogen peroxide of each selected nanomaterial in an electrochemical setup. The measurements reveal that both the sensors present similar limits of detections (7.3 μM for CNT and 8.8 μM for graphene) and increase the electrode-electrolyte interface area up to over 100 times. The final part of the thesis will focus on all those elements that can introduce uncertainty on the overall measured signals in order to better understand the quality and the reliability of the proposed aerosol jet printed electrochemical sensors. In this, a wide set of uncertainty components can be identified. Those include high-frequency interferences, the ones introduced by the instrumentation and the intrinsic noise of the sensor were identified. At first, the noise of sample resistors, whose noise sources are well known in the literature, are evaluated to have a comparison between the noise levels introduced by the instrumentation and the ones obtained in the electrochemical experiments. Moreover, the obtained electrochemical noise is evaluated in frequency calculating its power spectral density. This shows clear evidence of the superposition of effects that generates a low frequency ($f < 0.9Hz$) plateau generated by thermal and shot noise and a flicker-like noise at a higher frequency where the mass transport processes limit the noise spectrum. Since the former part of the spectrum underlines how the temperature is one of the most relevant components of noise (and thus

uncertainty) on those kinds of sensors, its effects were better explored in a new experiment. This showed how the standard deviation of the measurements increased as a result of increasing the temperature and how it acts as one of the main influence parameters that can change the average output current of the sensors. Then, to improve the reliability of these devices, a set of studies that aim to compensate for the effects of temperature through a reliable, in-situ temperature measurement will be presented. A new set of temperature sensors to be embedded in e-skin devices and in close proximity to the previously described electrochemical sensors are analyzed pursuing two different research paths; at first two different geometries are analyzed and compared to reduce the surface occupancy of the devices as well as reduce their sensitivity to bending. The main results reveal that both geometries present similar sensitivities to temperature ($TCR \approx 2.5 \cdot 10^{-3}\,°C^{-1}$) that produce resistance variations up to 12% (that are way more consistent than the variations related to substrate deformation $\approx 1\%$). The second research topic that is deepened regards the materials and their curing processes. In this latter work, both the macroscopic and microscopic characteristics are evaluated and compared in order to obtain relevant information to be used in the development of new and improved temperature sensors. The main results reveal how the increasing curing temperatures change the mean particle size of the used materials. This has different effects on the macroscopic characteristics that include a reduction of over 70% of the room temperature resistance as well as a strong decrease in the coefficient of variation (or relative standard deviation) up to 95%. The behavior of the sensors with regards to temperature is evaluated by means of a climatic chamber in the range $[-10; 70]$ °C.

Sommario

Il miglioramento delle condizioni di vita ottenuto negli ultimi anni ha generato un aumento e un invecchiamento della popolazione, creando il bisogno di un nuovo paradigma di sanità intelligente dove sia possibile monitorare da remoto la variazione dello stato fisiologico dei pazienti. In questo contesto, gli e-skin, definibili come dispositivi flessibili che incorporano array di sensori, rappresentano una tecnologia all'avanguardia che permette il monitoraggio di differenti parametri fisiologici direttamente dal corpo umano in modo non invasivo grazie alle loro ridotte dimensioni. Per via di queste loro caratteristiche, gli e-skin sono promettenti in varie applicazioni come quello industriale, la prostetica e al già citato campo clinico. Questa loro grande applicabilità è resa possibile dai molteplici sensori che permettono di acquisire dati in modo preciso e distribuito. In questo contesto infatti, i sensori hanno assunto un ruolo centrale dal momento che hanno come compito principale la trasduzione dei differenti segnali d'interesse come ad esempio temperature, pressioni, deformazioni, biopotenziali e marcatori biochimici (e.g. ioni, metaboliti, metalli pesanti, amminoacidi, ormoni, farmaci, stupefacenti, ...). Quest'ultimo gruppo di marcatori sta recentemente suscitando un enorme interesse da parte della comunità scientifica dal momento che permettono il veloce riconoscimento di molteplici stati fisiologici e patologici. Ad oggi, per la misura di questi marcatori biochimici, la ricerca si sta concentrando sui biosensori dal momento che sono un'alternativa valida, più economica e di uso più facile rispetto ad altre tecniche di analisi di laboratorio (e.g. protocolli ELISA, cromatografia, ...) ad oggi usate come gold standard. Fra i possibili principi di trasduzione adottati correntemente per i biosensori in letteratura, l'elettrochimica presenta molteplici vantaggi fra cui un basso costo, un' alta sensibilità e l'uso di strumentazioni relativamente semplici. In questa tesi, verranno descritti differenti approcci per lo sviluppo e il miglioramento di sensori elettrochimici stampati applicati agli e-skin. La discussione partirà da una breve descrizione del principio di trasduzione di questi sensori e si focalizzerà in seguito prima su differenti approcci per il miglioramento delle caratteristiche metrologiche e poi sulla valutazione, monitoraggio e mitigazione delle componenti d'incertezza che possono influire sui dispositivi proposti. In questo contesto, la tesi si aprirà con una revisione della letteratura per intro-

durre i concetti generali riguardanti gli e-skin e i biosensori, in modo tale da poter comprendere meglio sia il loro principio di trasduzione e le loro limitazioni attuali. In seguito, sarà presentato un primo prototipo di un e-skin multisensing per la misura non invasiva e personalizzata dell'affaticamento muscolare che comprende sia un sensore elettromiografico (EMG) a 8 canali sia un sensore elettrochimico. Brevemente, i risultati raggiunti sono promettenti per entrambi i sensori. Quelli EMG permettono il monitoraggio delle features EMG durante l'affaticamento. Per quanto riguarda il sensore elettrochimico, è possibile monitorare in modo continuo la variazione di concentrazione di lattato all'interno del range fisiologico (10-100 mM), ottenendo però sensibilità di circa 0.35 $\mu A \cdot mM^{-1}$ che non sono completamente soddisfacenti per l'applicazione e devono pertanto essere migliorate. Partendo da queste considerazioni, i successivi due progetti si concentrano sulle modalità di miglioramento della sensibilità e del limite di identificazione (limit of detection, LOD) sfruttando micro- e nano- strutturazione della superficie. La prima soluzione esplora la possibilità di sfruttare l'aerosol jet printing (AJP) per la realizzazione di microstrutture che dalla superficie si innalzano nella terza dimensione. Il processo che viene proposto permette infatti di fabbricare microstrutture che aumentano fino al 130% la superficie elettrodo/elettrolita senza cambiare l'area occupata del substrato. Parallelamente, l'aumento dell'area si ripercuote sulla sensibilità del sensore che risulta aumentata in media di 2.3 volte rispetto agli elettrodi senza microstrutturazione. Il secondo approccio seguito sfrutta allotropi nanostrutturati del carbonio come funzionalizzazione. I due materiali selezionati sono dei nanotubi di carbonio a parete multipla (CNT) e grafene dal momento che sono comuni in campo industriale, relativamente economici e adatti a lavorare in campo elettrochimico. I diversi test che sono effettuati mirano alla definizione delle finestre di potenziale stabile, alla valutazione alla stabilità nel tempo e della capacità di rilevare perossido d'idrogeno per ognuno dei nanomateriali selezionati. Le misure mostrano che entrambi i materiali presentano simili limiti di rivelazione (7.3 μM per i CNT e 8.8 μM per il grafene) e aumentano la superficie d'interfaccia elettrodo/elettrolita fino a 100 volte. In seguito, il lavoro si è concentrato su tutti gli elementi che possono introdurre incertezza sul segnale misurato in modo tale da comprendere meglio la qualità e l'affidabilità dei sensori elettrochimici stampati con AJP proposti. In questo ampio insieme di componenti d'incertezza possiamo distinguere fra interferenze in alta frequenza, quelle introdotte dalla strumentazione e il rumore intrinseco al sensore elettrochimico. Inizialmente, si è valutato il rumore di una resistenza standard che è ben noto in letteratura per avere un metro di paragone e comprendere i livelli di rumore introdotti dalla strumentazione di misura. Poi, il rumore ottenuto durante un esperimento di elettrochimica è stato valutato in frequenza calcolando la sua densità spettrale di potenza (PSD). In questa analisi sono emersi effetti sovrapposti che generano a basse frequenze

($f < 0.9Hz$) un plateau legato principalmente ad effetti termici e a frequenze più alte un rumore di tipo flicker legato ai fenomeni di trasporto di massa. Dal momento che la prima parte dello spettro evidenzia come la temperatura sia una delle più rilevanti componenti del rumore (e quindi dell'incertezza) su questa tipologia di sensori, si è proceduto a studiarne gli effetti in un nuovo esperimento. Questo mostra come la deviazione standard delle misure cresca all'aumentare della temperatura di lavoro e come questa agisca come uno dei principali parametri d'influenza che può cambiare la corrente d'uscita media dei sensori. Pertanto, al fine di migliorare l'affidabilità dei dispositivi proposti, un nuovo insieme di analisi sono state presentate per provare a compensare gli effetti della temperatura per mezzo di misure affidabili ed effettuate in prossimità del fenomeno d'interesse. A tal fine, si sono esplorati due possibili campi di ricerca per la realizzazione di sensori di temperatura che possano essere incorporati all'interno di dispositivi e-skin e in prossimità di un sensore elettrochimico. In prima battuta, si sono analizzate e confrontate due possibili geometrie che possano ridurre l'occupazione dell'area occupata e al contempo ridurre la dipendenza del sensore dalla deformazione del substrato. I risultati principali rivelano che entrambe le geometrie propose presentano sensibilità alla temperatura simile ($TCR \approx 2.5 \cdot 10^{-3}\,°C^{-1}$) con variazioni di resistenza fino al 12%, molto più rilevanti rispetto alle variazioni ottenute quando si è valutata la dipendenza dalla deformazione del substrato ($\approx 1\%$). Il secondo campo di ricerca che si è approfondito si concentra sui materiali e sul loro processo di cura. In quest'ultima parte, si valutano e confrontano le caratteristiche microscopiche e quelle macroscopiche al fine di ottenere informazioni che possano essere usate nella progettazione di nuovi e migliori sensori di temperatura. I risultati principali mostrano come al crescere della temperatura di cura ci sia una tendenziale aumento della dimensione media delle particelle del materiale depositato. Questo ha molteplici effetti sulle caratteristiche macroscopiche fra cui la riduzione di oltre il 70% della resistenza a temperatura ambiente e la diminuzione del suo coefficiente di variazione fino al 95%. Simili risultati si ottengono anche valutando il comportamento in temperatura dei sensori per mezzo di una camera climatica nel range di temperatura $[-10; 70]$ °C.

Contents

List of Figures

List of Tables

Chapter 1

Introduction

In the modern era where overall living conditions improve, the population increases and ages, the need for a new paradigm of healthcare is rising. In this frame, the need to monitor and track the changes in the physiological status of patients or sports professionals in an unobtrusive way, attracted huge interest from the scientific community starting in the 1950s [1] with the first wearable devices for human-machine interfaces in prosthetics.

Then starting in the 1970s, this idea evolved in order to develop flexible skin-like devices to improve the user comfort and usability of the devices [2]. This concept was then deepened at the beginning of the 21st century in the frame of personalized medicine that proposes the wide use of wearable sensors to improve the care for the elderly population and reduce medical costs making this technology a profitable deal [3].

In this frame, the miniaturization of those wearable devices is seen as a new frontier. This is leading the research to reduce the thickness of those devices and to distribute the sensors on a larger area to better monitor the physiological parameters of the human body. This trend is leading to the development of a new class of devices that mimic human skin and are called electronic skins or e-skins.

1.1 E-skins

In this section the concept of e-skin will be deepened, starting from the usual definitions provided and then discussing the usual implementation of the systems.

Even though a unique definition of e-skin is not provided, different literature works propose different definitions such as:

- "Electronic skin (e-skin), which mimics the functions of human skin, consists of a flexible pixel array in which the cells of each sensor can transform external stimuli, into electronic signal." [4]

- "large-area, flexible array of sensors with data processing capabilities, which can be used to cover the entire surface of a machine or even a part of a human body" [5]

- "E-skin is a kind of electronic device that simulates human skin to perceive subtle stimulus signals from the outside world. It is formed by integrating various high-performance functional sensors on a flexible substrate; the sensor becomes one of the key components" [6]

The common aspect that arises from all these definitions is the need to emulate human skin. In this sense, e-skin devices aim to be flexible to conform to the human body, to have a wide area and to be integrated with different kinds of sensors to collect data from the external environment. Moreover, the concept of e-skin can be extended to augment not only to replicate the functionalities of the human skin but also to introduce new ones such as magnetic fields [7], [8], the intensity of environmental light [9], [10], proximity [11], but also physiological data to retrieve the health status of the individual such as electrical biosignals [12]–[14] and the concentration of different analytes in sweat [15]–[17].

As stated in the definition provided in [6], the sensors are the "key components" of those devices. However, the whole e-skin system requires a whole architecture to work correctly. This architecture is similar to the one proposed for a wearable device (WD). In general, those are composed of two units depicted in figure 1.1. The external unit is a support device that allows the readout of the collected data, its processing, storage and visualization. On the other hand, the wearable unit is the one that embeds all the sensors, the conditioning electronics, the communication interfaces and logic controllers.

To this general architecture, a set of considerations must be added to fully understand the characteristics of these devices. At first, the main target should be kept into consideration: an e-skin aims at mimicking the human skin and to expand its characteristics in terms of sensing capabilities. Thus, those devices should at first be flexible and stretchable in order to adhere to the human body [6], [18]. This first characteristic also affects the wearability of the devices and thus the final user comfort. In evaluating comfort, other factors such as aesthetic appeal and user-friendliness should also be taken into consideration [19].

Moreover, the possibility to embed in a single device a whole set of sensors on a flexible substrate is highly demanded both to better control the physiological status of the individual [8] and to improve the reliability of the system through the compenastion of influencing variables (e.g. temperature) [20]. However, multi-sensing systems must be carefully designed to avoid crosstalk between the different sensors and their electrical interfaces and to optimize their production process [8], [21].

Other important characteristics can be found in the field of material science. An example is the device's biocompatibility [22] and its self-healing capabilities [23]. The former is relevant to avoid skin rashes and further improve the user experience, while the latter allows to automatically restore the functionalities of the device after mechanical damage.

To summarize, e-skins are an interdisciplinary topic that involves researchers from different fields and backgrounds. The potential of those devices is relevant in a plethora of applications ranging from the industrial environment for quality assessment towards the clinical yards to monitor the physiological state of patients.

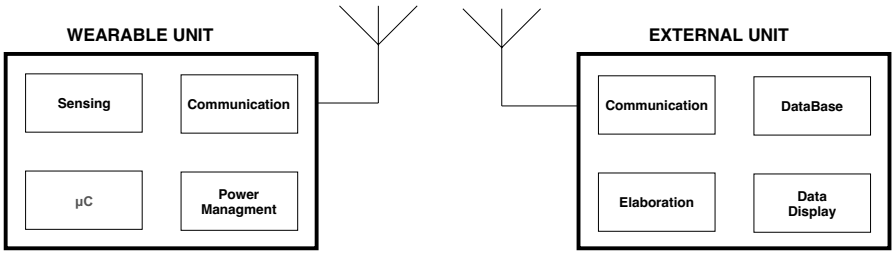

Figure 1.1: Generic Block diagram of an e-skin device

1.2 Possible applications of E-skins

E-skins are a family of devices that can be used in a broad set of applications and fields.

In the industrial environment, for example, e-skins can be mounted on robots to improve their capabilities in terms of object recognition, and feedback from the environment. [24]

In a similar way, e-skins can be mounted on prosthesis to provide different kinds of feedback to the users such as haptic and temperature. A different kind of e-skins used in prosthetics is related to the collection of biosignals from the limbs of the user to control the prosthesis using for example EMG signals [25].

Another key application of e-skins is related to human health monitoring both in the clinical environment [26]–[28] and in sports medicine [29]. In this frame, biomarkers attracted huge interest in the scientific community since it expands the diagnostic capabilities of the devices allowing to detect a wider set of pathologies as well as to monitor different behaviors [30].

Moreover, due to their distributed nature on the human skin, they can help collect enormous datasets to feed artificial intelligence (A.I.) algorithms to further deepen the current knowledge in all the aforementioned fields, but also in the entertainment industry providing novel human-machine interfaces [2], [7], [31].

1.3 E-skin Sensors

1.3.1 Sensor Typologies

Among the many kinds of sensors available in the literature, the most proposed in e-skin devices cover a wide subclass that is able to detect many different physical quantities.

In order to provide haptic feedback, soft pressure sensors are necessary. They are mostly developed as capacitive pressure sensors (CPS) on soft and flexible substrates. Those are able to achieve good sensitivity at low applied pressures, that however declines at higher applied pressure values.[32] Other common kinds of pressure sensors are based on piezoresistive and triboelectric materials. [33]

Moreover, to provide better tactile feedback, the use of strain sensors was introduced. Both standard metallic wire-based strain gauges and capacitive ones are currently employed and are promising in a plethora of applications such as detecting human complex motion and/or movement of the joints. [34]–[38]

Another important class of sensors used in e-skins is temperature sensors. They are used to improve the tactile feedback both in robots and prostheses and in the medical field such as for infective diseases and illness control [28], [39], [40].

Four main kinds of temperature sensors were developed for e-skin application [41]: resistive (e.g. thermistors and thermoresistances) [4], [42] capacitive [43], transistor-based [44], PN-junction based [45] Among them, resistive-type temperature sensors are the most promising for e-skins thanks to their advantages in terms of production processes, sensitivity and stability.

In the matter of human well-being tracking, health monitoring and rehabilitation processes, biopotentials such as electromyographic (EMG) and electrocardiographic (ECG) signal represent a highly investigated and discussed field. Two main kinds of electrodes are currently employed: wet electrodes and dry electrodes. [13] The former class is mainly represented by pre-gelled silver/silver-chloride (Ag/AgCl) electrodes. Those are widely used to measure biopotentials thanks to their low contact impedance which eases the measurement process and increases the quality of the signal. This kind of electrode is based on a sensing silver area that is interfaced with the skin through a conductive gel. even though they present good characteristics, they are usually not suitable for long-term monitoring since they can cause allergic reactions and irritate the skin. The second possibility is to use dry electrodes (e.g. [12]). Those are usually made of metal or conductive inks and they seem promising in long-term monitoring since they can adhere solidly to the skin even when the patient moves.

1.3.2 Employed Materials

The characteristics of the e-skin devices shown in the previous sections impose a set of specifications to be followed in terms of materials to be used. Briefly they must be flexible and conformable even on complex and soft 3D structures such as the human body, be resistant to wear and tear and being able to withstand all the chemical and physical production processes. [2], [46]

The employed materials can be divided in three main groups that will be analyzed in the following pages: substrates, conductive materials and dielectrics.

1.3.2.1 Substrates

The substrates are the main materials that need to be investigated when looking at the flexibility and bendability of the whole e-skin device since they provide its mechanical support.[2], [47]

The literature is moving towards using low-cost and recyclable materials as substrates such as paper[1], but recently the most used substrates are composed by standard polymers such as polycarbonate (PC), Poly(dimethylsiloxane) (PDMS), polyethylene (PEN), Polyethylene terephthalate (PET), polyimide (PI), polyurethane (PU) [1], [48] thanks to their exceptional mechanical properties as well as their fitness to withstand most chemical/physical processes.

PDMS, for example, is robust, has an high flxibility and it is biocompatible. Moreover it is relatively light and presents good stability both under the thermal and the electrical point of view.

Another group of materials that is attracting the researcher attentions is fabric textiles and fiber-based substrates thanks to their flexibility and stretchability that allows them to be easily embedded in clothes.[21]

1.3.2.2 Conductive Materials

Conductive materials are the ones used to prepare interconnection and they are often used in may parts of the sensors design. Under an additive manufacturing point of view, those materials are mostly proposed as functional inks that can be directly printed on a substrate. The most common conductive inks can be divided in three sub groups: metallic nanomaterials, carbon allotropes and conductive polymers.

Metal Nanomaterials Metal nanoparticles are often chosen thanks to their exceptional conductivity and their versatility. The most used are based on noble metals such as silver and gold. [6], [38] The bare metallic nanoparticles are often mixed with different solvents and additives (e.g. methanol, isopropyl alcohol,

polyvinylpyrrolidone, ...) in different proportions in order to increase the printability of the overall ink, avoid the agglomeration of the nanoparticles and ease the adhesion between the nanoparticles and the substrate. [49] Even though the use of such noble metals is widespread thanks to their outstanding conductivity and their stability to oxidation, different less-noble metals such as copper, aluminum or nickel are often chosen as cheaper alternatives. The use of these different materials is however conditional to the process to avoid their excessive oxidation during the device fabrication. [50]

Carbon Allotropes This group of materials include all the inks that are carbon based. It includes all the inks based on carbon powder as well as the ones based on the carbon nanostructures such as carbon nanotubes (CNTs and MWCNTs for instance), carbon black and graphene. [38] Usually carbon based inks have an high processability, low-toxicity, flexibility and low production cost as well as an acceptable conductivity that however changes according to the used allotrope. [6], [51]

Conductive Polymers These are the last group of conductive materials that are widely used in the literature. They are usually organic polymers such as polypyrrole (PPy), polyaniline (PANI), and poly(3,4-ethylenedioxythiophene) (PEDOT) that doped into a conducting state and they are mostly used as interconnections and electrodes. [38], [49] PEDOT-based polymers in particular have been widely used in stretchable and biocompatibles eskin since it is stable in ambient conditions and it can be doped (for example) with poly(-styrenesulfonate) (PSS) to achieve high conductivity. [52] In general, these conducting polymers that are easily processable and printable on diverse substrates and, since their conductivity can be tuned with doping, they can be used as semiconductors to fabricate active components such as transistors. [53]

1.3.2.3 Dielectrics

This set of materials is usually employed in the production of sensors, protection layers as well as part of active sensors. For instance, Dielectric materials are used in capacitive sensors to separate the two plates of the devices and, increasing the dielectric constant, to increase the overall capacitance of the device [47]. In a similar way, dieletrics materials are used in the production of active components such as transistors to insulate the gate[49]. Moreover, the use of dielectric materials in conjunction with additive manufacturing techniques can allow the production of functional parts of other sensors such as microfluidic channels. [54] Another application, shown for instance in [55], is to protect the printed tracks and stack different conductive layers on top of the others. Among the most common dieletric

materials inorganic materials such as silicon dioxide (SiO_2), silicon nitride (Si_3N_4), and Magnesium oxide (MgO) can be found. Those are often used to produce nanoparticles that can be employed in functional inks. Other common printable organic materials (e.g. PVA, cellulose, and silk) have been explored as well as other polymers. [49]

1.3.3 Hints on Production Processes

The production of an e-skin device is a challenging factor since they require the integration of different sensing materials and sensors in a limited physical dimension. In literature the different technologies that are explored to produce those kinds of devices can be divided into two macro-areas: classical microelectronic technologies and additive manufacturing ones. [30]

The latter is a promising and quickly spreading set of technology that uses computer-aided design (CAD) data to build different kinds of components and sensors in a fully digital manner adding materials layer by layer. [56]

The most used and commercialized additive technologies for the fabrication of e-skins are maskless (they require no masks) and axis movements as well as the material ejection are controlled according to a digital file program. One major difference between the technologies is the ability to print on 2D (e.g. inkject printing, IJP) or non-planar/3D (e.g,. aerosol jet printing, AJP) substrates.[57]

1.4 Challenges for E-skins Development

Even though those e-skin devices are promising, a set of challenges must be faced in all levels of the design process. Among them, the main challenges involve biocompability issues, user comfort, metrological issues and design related ones (data transmission, power supply, architecture, production process...). [46], [58]

Biocompatibility is the characteristics of a material that does not cause any adverse response (both topical or systemical) on the final user. This theme of biocompability of the whole e-skin device is prominent to avoid rashes, skin irritation or other harmful effects to the user. [38] This issue is usually addressed selecting materials that are tested to be biocompatible.

Moreover to improve the user comfort, the devices must be mechanically compatible with the human body and able to easily conform even while performing their sensing tasks. [46] The conformability of e-skin devices can be divided in three different aspects: flexibility, stretchability and permeability. Those aspects can be improved with an accurate materials selection (e.g. selecting porous films or fabrics to increase the permeability) as well as reducing the thickness and the size of the device. [38]

However, reducing the size of the devices is a restrictive specification that complicates the overall design process as it introduces crosstalk and response time issues as well as data transmission and power supply problems. [26], [48], [59]

The data transmission is important to retrieve data from the e-skin device and to send setting data. Since wired communication can be unsuitable due to the lack of user comfort, wireless technologies needs to be implemented. One of the solution currently used is to develop system based on commercial wireless chips such as Bluetooth, radio frequency identification (RFID) and near-field communication (NFC). However those chips are often rigid and can cause discomfort to the users limiting his/hers movements [59], [60]. Another possible solution is the use of electromagnetic coupling to transmit information towards an external readout unit. In most situations, the e-skin is based on resonant RLC circuits, while the external unit is composed by a coil and a readout circuit. While designing the system the inductance in the e-skin device must be carefully considered since its size mostly dictates the resonant frequency as well as the detection range. [61]

Another important design specification is the power consumption and in general the power supply. Even though some of the above-mentioned communication systems can transfer the energy needed both for the data transmission ad to collect the data itself [59], in many applications this method is not feasible.

The majority of e-skin devices are then often provided with power storage systems such as batteries and super capacitors. Those however are often bulky and weighty and thus reduce the final user comfort. [15]

Another open research field is energy harvesting. Those self-powered devices integrate energy storage or transducing functions, which can work without another external supply for instance working thorough photovoltaic, thermoelectric, and mechanical energy (e.g. triboelectric nanogenerators or TENGs, piezoelectric nanogenerators) harvesting methods. [2], [26], [48] Another possibility are fuel cells, green and environmentally friendly batteries that convert the energy released from chemical reactions into electrical energy. Biofuel cells are a particular subclass, which uses microorganisms and/or enzymes to catalyze the reactions that generate the energy. Depending upon the type of catalyst, it can be divided into microbial fuel cells and enzymatic biofuel cells. Those devices are promising since they can work at room temperature, are safe, low cost and present good biocompatibility. [26]Moreover, bio fuel cells can use metabolites to produce power and some of those metabolites can be relevant in the clinical practice. Following this line, some researchers produced a set of devices capable both to detect analytes and supply power. [31], [62] This opportunity is appealing since it allows expanding the sensing capabilities of the e-skin devices towards a new frontier of chemical and biological analytes.

1.5 Biochemical Markers Detection

Biochemical Markers such as ions, metabolites, heavy metals, amino acids, hormones and drugs (including as an example licit, illicit ones and alcohol) are currently used in the clinical practice to monitor both physiological, pathological and altered states of the human body [17], [30], [62], [63].

In order to continuosly monitor those biomarkers different biofluids (saliva, blood, tears, sweat, interstitial fluids, etc...) are explored in the literature [64], [65]. Among those biofluids, sweat is one of the most easily accessible as well as the least invasive to sample from the human skin [16], but its sampling is still a challange for sedentary individuals whose transpiration is limited. In this frame the sensor must be able to work with small samples and also measure the sweat rate to be re-calibrated continuously [58], [61], [64]. The re-calibration issue has to be addressed to take into account the drift effects and the one of all the possible influence variables. To do so one promising pathway is the development of multi-sensing platform to monitor many influence variables as well as different interfering analytes in order to improve the accuracy and the selectivity of the devices as well as to allow the compensation of the different effects [16], [63]. Similar considerations may be done on the topic of shelf life and stability of those kind of sensors. Those are mainly affected by the biological components that are prone to degrade under certain environmental conditions related for example to pH, temperature and ionic strength that are variable and unpredictable in e-skin applications [63].

1.6 Thesis Aim and Outline

This thesis will focus on the design and improvement of electrochemical biosensors for e-skins. In chapter 2 the theme of biosensors is introduced and deepened, with a specific focus on the transduction principle of electrochemical ones. Then in chapter 3, a first prototype of a multi-sensing patch for fatigue detection using both electromiographic and electrochemical sensor is presented. This first work provided the initial cues to the development of improved fully printed electrochemical sensors empowered by both micro- and nano- structures (chapter 4 and 5 respectively). Then, in chapter 6 the uncertainty sources that affect those kind of sensors are experimentally evaluated. Moreover, the effects of temperature are presented and different studies on temperature sensors to be integrated in e-skin devices are presented. Lastly, the general conclusions and the future outlooks are presented in chapter 7.

Chapter 2

Biosensors

2.1 Introduction

In recent years, the detection of different kinds of analytes attracted a great interest in many fields as cellular processes, food control, clinical practice and environmental control [66]–[68].

Those operations are currently performed using standard in-lab methodologies such as chromatography, spectrometry and ELISA protocols[69]–[72]. Even though those techniques allow excellent sensitivity and limit of detection (LOD), they often require long and complex sample preparation that must be executed by trained and skilled professionals.

On the other hand, a biosensor is an analytical device that can be used to detect an analyte employing a biological sensing element and a transducer. The former acts a bio-recognition element that interacts with the analyte, while the latter transduces the information to a different (usually electrical) physical domain. The advantages of electrical over chemical signals are countless since the former type present a well known behavior and many established elaboration and analysis techniques both in digital and analogue domain and will not deepened in this work. Comparing these devices to standard chemical analysis techniques, different advantages can be underlined. Among them the main advantagesis that biosensors can be designed to work in out-of-lab conditions and operated by unskilled operators.

2.2 Biosensor Classification

In this section, two different biosensors classifications are exposed. At first, according to the bioreceptor used, and then according to their transducers. So, the main difference between the two classifications regards which part of the overall

sensor is taken into account. Those two kinds of classifications are represented in figure 2.1.

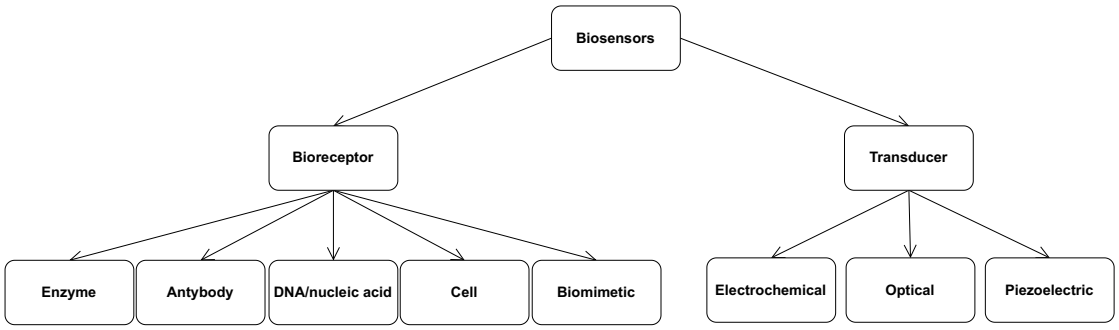

Figure 2.1: Schematic rapresentation of the two main kind of biosensor classification.

2.2.1 Classification by Bioreceptor

In this first type of characterization the biological part that recognizes the analyte of interest is taken into account. Their main task is to insure specificity and selectivity towards the target analytes avoiding cross-talk between different species [142]. This is achieved through a selective affinity between the bioreceptor and the target analyte.

To achieve these functionalities both natural and synthetical elements are used. The most common are:

- **Antibodies**: Y-shaped natural complexes that bind the analytes in specific sites permitting a selective detection [73].

- **Enzymes**: They uses non-covalent bonds to bind the analytes in active sites and catalyze chemical reactions. Are best used within electrochemical biosensors [73], [74].

- **DNA/nucleic acids**: unique complementary binding pattern of DNA to a target analyte. It can be designed artificially and immobilized on the surface of the biosensor [73].

- **Molecularly Imprinted Polymers (MIPs)**: patterned polymer matrix used to achieve analyte specificity through patterns of non-covalent bonding, electrostatic interactions, or size inclusion/exclusion [74].

- **Ion-selective membrane (ISM)**: porous membrane used as a recognition element that allows the passage of the target ion to get in contact with the electrode. It is responsible for the selectivity of the biosensor for the target ion from various interfering ions present in the test sample [75].

All those biorecognition elements are usually immobilized to the surface of the biosensors to improve their durability. To do so, a set of different methods are employed [76]:

- **Adsorption**: the biorecognition element bonds with the electrode surface. It may be chemical adsorption (covalent bonds) or physical (van der Waals bonds).
- **Covalent bonding**: the electrode surface is treated to present functional groups that binds the biological material.
- **Matrix entrapment**: a polymeric gel matrix is used to trap biomolecules. It causes a barrier to the diffusion and thus slows down the reaction.
- **Encapsulation**: an inert membrane is used to entrap the biorecognition element.
- **Cross-linking**: biomolecules are intermolecularly cross-linked using bi-functional or multi-functional reagents.

2.2.2 Classification by Transduction Principle

A second possibility to classify biosensors considers the transduction principles that convert the signal from the process of interest to an electrical-detectable one [77]. Even though different kinds of transducers are presented in the current literature, the three most common kind of transducers for biosensors are optical, piezoelectric and electrochemical.

Optical Biosensors are currently used by many biosensors due to the different types of spectroscopy that can be carried on. This class of biosensor is able to provide label free, real time and parallel detection of the target analytes and it is performed by exploiting the interaction of the optical field with a biorecognition element[77], [78].

Piezoelectricity is an interaction between the mechanical and electrical domain in a device. A piezoelectric based biosensor works on the principal that an oscillating crystal resonates at a certain frequency that is controlled by an external electrical system. When the target analyte's molecules interface the biosensors a reaction occurs and they bind to the sensor itself changing the resonant mass and thus the resonant frequency of the sensors[77], [79].

An electrochemical biosensor can be defined as an integrated device capable of providing quantitative information keeping in contact a biological recognition element (biochemical receptor) with an electrochemical transduction element. Between the two elements a set of chemical reactions take place and those generate or suppress electrons and thus an electrical signal that can be easily measured.[1] In the literature, many studies have revealed that this class of biosensor presents many advantages over the previously presented ones such as detection speed, low cost, high sensitivity, and relatively simple instrumentation [77].

2.3 Transduction Principle of Electrochemical Biosensors

In a biosensor analytes are usually biological molecules that can be modified by an enzymatic layer. In the case of L-lactate, for example, it can be sensed using an enzymatic layer based on L-Lactate Oxidase that produces hydrogen peroxide (H_2O_2) according to reaction 2.1.

$$L - lactate + O_2 \rightarrow Pyruvate + H_2O_2 \tag{2.1}$$

It can be then oxidized according to reaction 2.2 using different electrochemical methods applying around 0,6 V. This voltage could however oxidize different analytes that could interfere with the measurement. To avoid those issues, a mediator layer, usually made of Prussian blue, is introduced to reduce the potential needed to oxidize the hydrogen peroxide.

$$H_2O_2 \rightarrow O_2 + 2H^+ + 2e^- \tag{2.2}$$

Even though the overall transduction principle here presented and summed up in figure 2.2 is complex and has different steps, its core relies in the oxide-reduction reaction 2.2 that generates the output current. This kind of reaction happens usually in an electrochemical cell whose basic principles will be discussed in the following sections.

Most of those theories are well known in electrochemistry and are here reported to introduce the topic and to ease the understanding of the whole work. The hereby information were retrieved from [80]

[1] An in-depth analysis of the transduction principle of the electrochemical biosensors is provided in the next section.

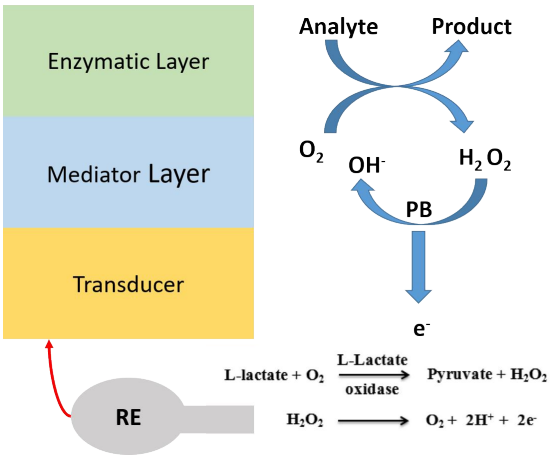

Figure 2.2: Overall transduction principle for a lactate enzymatic biosensor

2.3.1 Electrochemical Cell Basics

The electrochemical sensors are usually based on an electrochemical cell. It is a structure usually composed by three electrodes called working (WE), reference (RE) and counter (CE). WE is the functional electrode where all the reactions take place. This one may be functionalized and is usually composed by noble metals (gold, platinum, ...) or by inert materials like carbon. The RE is assumed as the point of reference for the voltage applied to the cell and it is usually composed by noble metals like platinum or silver. CE is an auxiliary electrode that is needed to provide electrons to the reaction. It should be geometrically larger than the WE not to limit the reaction that can occur on it. The electrochemical cell is used for different measurement techniques that could be divided in two main families: potentiometry and amperometry. The former measures the open circuit voltage on the cell and can be used to evaluate the kinetics of a chemical reaction 2.3 as modeled in the Nernst equation 2.4. Being A and B the reagents that produce C and D, and using the square brackets to describe their concentrations. R is the gas constant, F is the Faraday's constant, n is the number of electrons transferred in the semi-reaction and E_0 is the standard cell potential.

$$A + B \rightarrow C + D \tag{2.3}$$

$$E = E^0 - \frac{RT}{nF} \ln \frac{[C][D]}{[A][B]} \tag{2.4}$$

Amperometries on the other hand, are active measures since the operator controls the RE-WE potential and measure the resulting current flow between WE and CE. A classical setup is shown in figure 2.3.

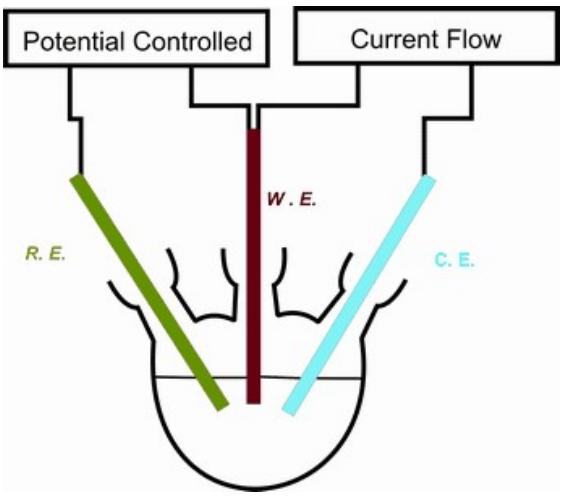

Figure 2.3: Classical setup for an amperometric experiment

2.3.2 Physical/Chemical Description

In order to fully understand how these systems generate a current, it is important to understand the physical and chemical processes that happens when an electrode is put into a solution. Those can be classified in three main branches: electrical double layer effects, charge transfer processes and mass transport processes.

2.3.2.1 Electrical Double Layer

When an electrode is submerged into an electrolyte solution, the electrical double layer is formed. At the electrode/electrolyte interface two layers of charge with opposing polarity form. The first one is inside the metal and the second, known as outer Helmholtz plane (OHP) is produced by ionic charges into the solution. Those two layers are divided by a single one of solvent molecules known as inner Helmholtz plane (IHP) that acts as dielectric in a capacitor. Inside the solution after the Helmoholtz planes, there is a diffuse layer where concentration of species are influenced by electrostatic and diffusion forces.

it is important to notice that when the potential at the electrode is changed, charge flows onto the electrode|electrolyte interface changing the capacity of the capacitor. The flow of charges is known as differential capacitive current.

2.3.2.2 Charge Transfer Processes

The charge transfer processes describe how electrons move from the solution to the electrodes generating a Faradic current. Those processes relies on reactions where chemical species gets oxidized or reduced freeing or adsorbing electrons. On

the electrodes we can describe the current density j on the electrode using the Bulter-Volmer equation 2.5 where:

- j_0: exchange current density, $\mathrm{A\,m^{-2}}$.
- η: activation overpotential, V. It is defined as the difference between the electrode potential E and the equilibrium potential E_{eq}.
- T: absolute temperature, K.
- R: universal gas constant.
- n: number of electrons involved in the electrode reaction.
- F: Faraday's constant.
- α_a: anodic charge transfer coefficient.
- α_c: cathodic charge transfer coefficient.
- c_o^*, c_r^*: bulk concentration of species to be oxidized/reduced.
- $c_o(0,t)$, $c_r(0,t)$: time dependent concentration of the species to be oxidized/reduced at distance 0 from the surface of the electrode.

$$j = j_0 \cdot \left\{ \frac{c_o(0,t)}{c_o^*} \exp\left(\frac{\alpha_a nF}{RT}\eta\right) - \frac{c_r(0,t)}{c_r^*} \exp\left(-\frac{\alpha_c nF}{RT}\eta\right) \right\} \tag{2.5}$$

It is important to notice that the concentration on the surface of the electrode varies due to reagents depletion and mass transport processes.

2.3.2.3 Mass Transport Processes

Mass transport processes are needed to describe the variation of analytes concentration over time. In literature are reported three main effects: convection, migration and diffusion. The first describes the movement due to hydrodynamics, as could be a stirred solution. On the other hand, migration describes the movements of charged particles (like ions for example) in an electric field. Lastly, diffusion is defined as the spontaneous movement of any material from where it is to where it is not. In general it's a pseudo-random, concentration-driven movement.

Considering now that most of the analytes that are taken into account are neutral molecules that are not affected by migration and that convection is relevant only far from the electrode surface (figure 2.4), diffusion is the main process that must be evaluated in most experiments.

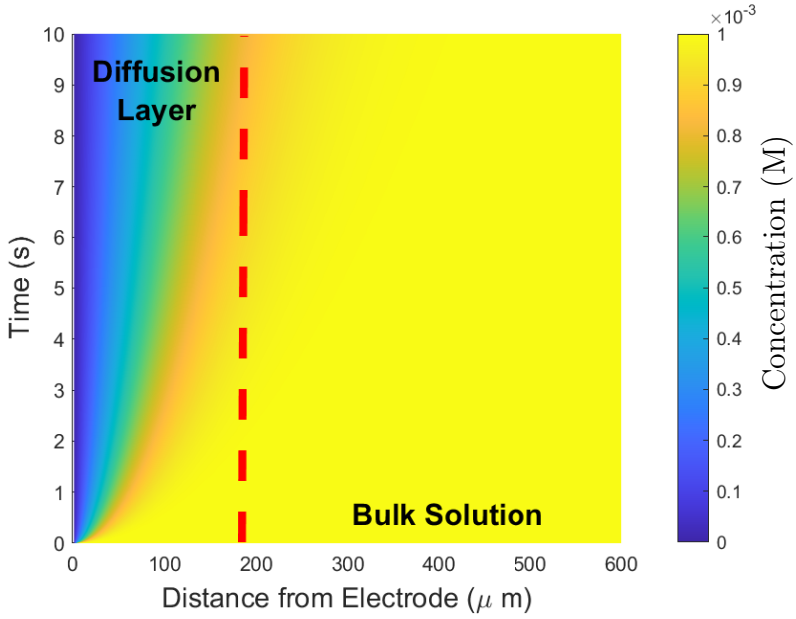

Figure 2.4: Typical concentration differences in a chronoamperometry experiment related to time (y-axis) and distance from the electrode (x-axis).

Diffusion can be described using Fick's Laws that relate the evolution of concentrations both to time and space. Those laws are reported[2] in 2.6 where:

- J: diffusion flux. It measures the amount of substance that flows through a unit of area during a unit interval.
- C: Analyte concentration.
- D: diffusion coefficient (or diffusivity).
- x: position related to the electrode surface.

$$\begin{aligned} J &= -D\frac{dC}{dx} \\ \frac{\partial C}{\partial t} &= D\frac{\partial^2 C}{\partial^2 x} \end{aligned} \tag{2.6}$$

[2]Here we present an mono-directional version to ease the understanding of the process, even though for a complete description vector equations have to be considered

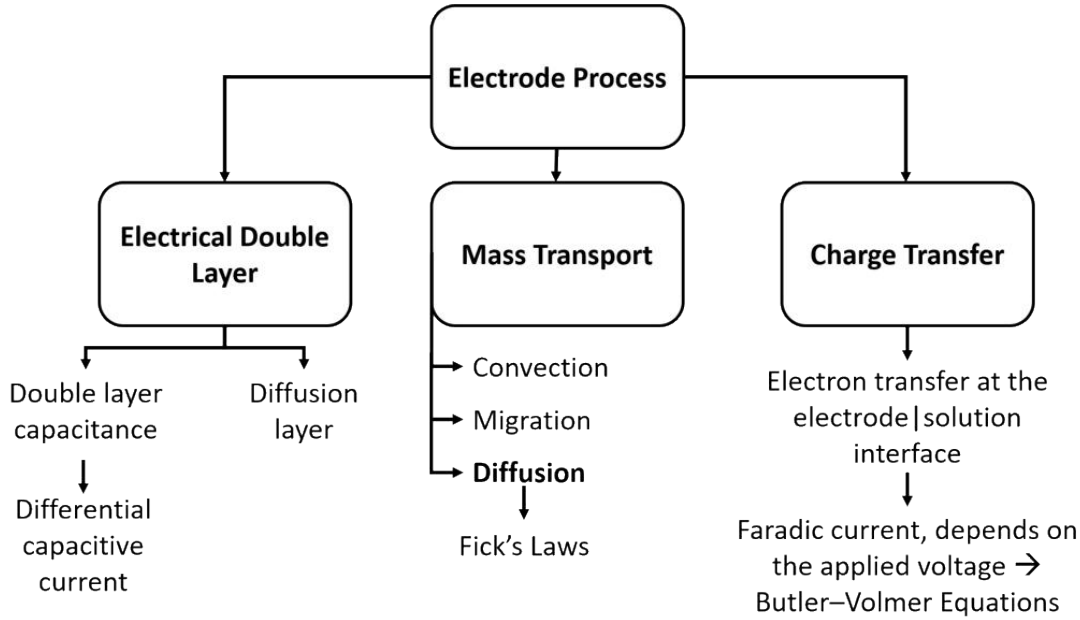

Figure 2.5: Summary of the electrode processes

2.3.2.4 Cumulative effect

In the previous sections we described the different processes, summarized in figure 2.5, that take place when an electrode is put in contact with an electrolyte. It is important to notice how those processes are not independent one another, but coexist and interact. The electrical double layer influences the dimensions of the diffusion layer where the mass transport is most relevant. At the same time, the mass transport processes influence the concentration of species and thus the faradic current produced by the charge transfer processes. In the majority of the situations the experiments are carried out assuming a diffusion controlled charge transfer process; that implies that the redox reaction speed is way higher than the effects of mass transfer and thus the latter is the one that is dominant for the faradic current generation.

Cell Equivalent Model All the aforementioned processes have a sensible impact on the impedance of an electrochemical cell that can be represented by the equivalent circuit in figure 2.6a. The usual module of the impedance spectrum is depicted in figure 2.6b.

At high frequencies, the solution characteristics dominates the impedance with an RC effect. The resistive tract is due to the solution resistance R_s that is dependent to the concentration (c) of ions in the supporting electrolyte and their mobility (μ) according to the simplified relation 2.7. The capacitive effect (C_s) is

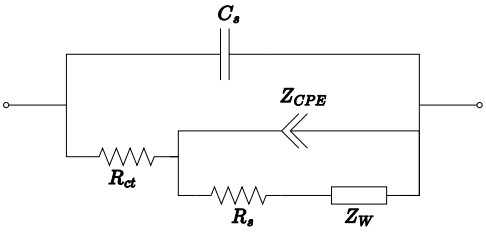

(a) Cell equivalent electric model

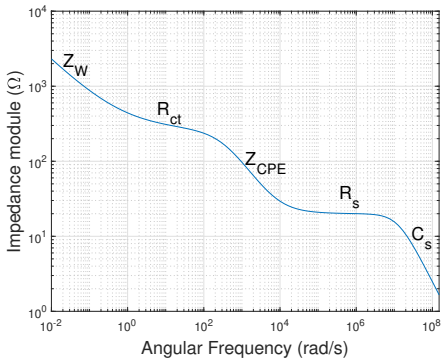

(b) Impedance of the cell equivalent electric model

Figure 2.6: Model of the cell impedance and its relative magnitude plotted versus the angular frequency ω in rad/s

due to the solvent dieletric constant. Both those quantities are dependant to the geometry of the cell.

$$R_s \propto \rho \propto \frac{1}{c\mu} \tag{2.7}$$

As already stated, the double layer capacitance can be modeled as a capacitor C_{dl} in series to R_s. This capacitor takes in consideration the effect of both the Helmontz planes (also known as compact layers) and the diffuse layer. It's possible to estimate the value of this capacitor according to 2.8 where:

- C_H: Compact layer capacitance
- C_D: Diffuse layer capacitance
- x_H: Dimension of the compact layer
- ε: Dielectric constant of the solvent
- ε_{sat}: dieletric constant of the solvent in case of high electric fields that cause the the orientation of the solvent's molecule. This phenomenon is called dieletric saturation
- L_D: Debye length. It is an estimation of the thickness of the diffusion layer that can be obtained from the Boltzmann statistics and the Poisson equation.
- n: number of charges of the ions in the solution
- q: elemental charge

- Φ_0: potential drop across the diffuse layer
- k: Boltzmann constant
- T: Absolute temperature
- A: Electrodes Area

$$C_{dl} = \frac{1}{C_H} + \frac{1}{C_D} = \frac{1}{A}\left(\frac{x_H}{\varepsilon_{sat}} + \frac{L_D}{\varepsilon \cosh\left(\frac{nq\Phi_0}{2kT}\right)}\right)^{-1} \tag{2.8}$$

It's important to notice how the double layer capacitance depends on the first few nanometers of the interface. As a matter of facts, the diffuse layer follows uniformly the surface if the superficial features have size much larger than the Debye lenght. Otherwise, if the surfaces presents defect geometrically comparable to the diffuse layer, the value of C_{dl} changes locally producing (with the solution resistances) different times constants in parallel. This overall produces an impedance that is not proportional to $\frac{1}{f}$, but in the order of $\frac{1}{f^\alpha}$ with $\alpha \approx 0.8-0.9$ for biological solutions. Thus, to take into account the surface non-idealities the constant phase element (CPE) (equation 2.9) is introduced. Q_0 represents the admittance of the double layer capacitance at $\omega = 1\mathrm{rad\,s^{-1}}$ and its impedance phase is constant at $(-90° \cdot \alpha)$.

$$Z_{CPE} = \frac{1}{Q_0(j\omega)^\alpha} \tag{2.9}$$

Moreover, it was shown how the charge transfer process allow transferring electrons from the electrode to the solution (or vice-versa) and how this is related to the applied potential in a non-linear way. A charge transfer resistance R_{ct} is usually defined as the derivative of the charge transfer relationship in the working point[3] to take into account all those processes.

In the end, it was shown how the charge transfer processes are usually limited by mass transport of the analytes in the proximity of the electrode-electrolyte interface. At low frequencies many molecules are required to sustain the current and thus an higher impedance is generated. This can be modeled by the Warburg impedance Z_W (eq. 2.10). The parameter σ takes into account the different diffusion rates (D_o and D_r for oxided and reduced forms) as well as the bulk concentration of the oxidized (c_o^*) and reduced (c_r^*) species that is in series to the charge transfer resistance and it is expressed in equation 2.11.

[3]It is important to notice that this is a differential quantity that is only valid in the proximity of the working point.

$$Z_W = \frac{\sigma}{\sqrt{\omega}} - j\frac{\sigma}{\sqrt{\omega}} \tag{2.10}$$

$$\sigma = \frac{RT}{n^2F^2A\sqrt{2}}\left(\frac{1}{c_o^*\sqrt{D_o}} + \frac{1}{c_r^*\sqrt{D_r}}\right) \tag{2.11}$$

2.3.3 Measurement techniques

In the literature, several techniques are reported to study electrochemical processes and for them are provided simplified, yet accurate, relations to describe the current resulting from the experiments [81], [82].

2.3.3.1 Electrochemical Impedance Spectroscopy

As reported in 2.3.2.4, the total impedance of the cell can be modeled an equivalent circuit in which each component can be related to a particular electrochemical process. The electrochemical impedance spectroscopic approach measures the impedance at different frequencies to evaluate different conditions in the electrochemical system. Usually, the results of those measurements are reported in a Nyquist plot from which many different parameters can be extracted. EIS can moreover be applied to evaluate the evolution of many electrochemical processes such as corrosion and electrodeposition.

2.3.3.2 Amperometric Techniques

It must be underlined that the sensor output current is composed by both the faradic current and the differential capacitive current. If the former is proportional to the analyte, the latter is not. In order to avoid measurements errors. In order to avoid measurements errors, in the next sections, some of the most common techniques are explained.

Chronoamperometry Chronoamperometry (CA) is an electrochemical method in which a step potential (figure 2.7a) is applied and the current is measured as a function of time. Assuming that the potential step the reaction proceeds at a diffusion-controlled rate. Under this condition we assume that before t_0 (the instant when the potential is stepped) the concentration is uniform and equal to the bulk concentration c^*. At t_0 all the analytes on the electrode surface ($x = 0$) are reduced and the ones at $x \neq 0$ are moved by diffusion. Fick's laws can be used then to derive the Cottrell equation 2.12 that describes the faradic current[4] related to the time t after the potential is stepped, the electrode's surface A, the diffusivity

[4]The Cottrell equation do not describe the differential capacitive current.

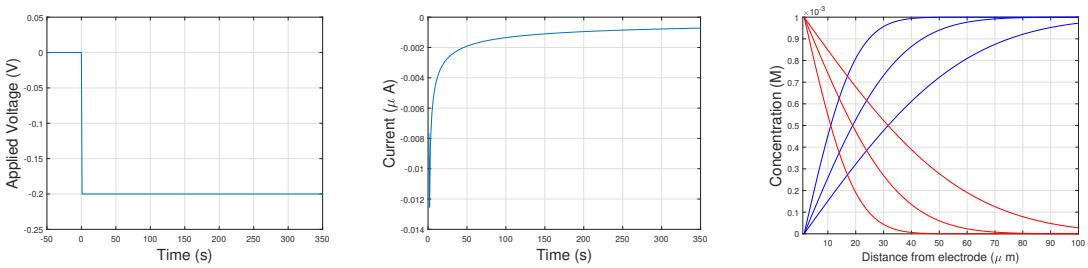

(a) (b) (c)

Figure 2.7: Theorical graphs that describe the various aspects of a chronoamperometry: the potential applied on the cell (a), the obtained current(b) and the local concentration of reduced (red) and oxidized (blue) analytes at three different times related to the distance from the electrode (c)

D of the species and the number of electrons n that take part into the reaction. As seen in figure 2.7b, the resulting current spikes at $t = t_0$ and then decreases in time. As suggested before this is due to the different analyte concentrations that are available at different times in the solution. As an example, three different instants (t_1, t_2, t_3) were simulated and the relative concentrations were plotted (figure 2.7c) related to the distance from the electrode.

$$i = \frac{nFAc^*\sqrt{D}}{\sqrt{\pi t}} \tag{2.12}$$

Chronoamperometry data are often plotted on a i-$t^{-\frac{1}{2}}$ plot that is called a Cottrell plot. It produces lines from theoretical data. Deviation from linearity may indicate that the redox event is associated to other processes like chemical reaction or to the differential capacitive current. The effects of the latter, that is neglected by the Cottrell equation, can be ignored considering only $t >> t_0$ because it has a faster dynamic than the overall faradic process.

Cyclic Voltammetry Cyclic voltammetry (CV) is ab electrochemical technique where the potential (E) between WE and RE is varied linearly at a set speed called scan rate (ν) as seen in figure 2.8a. The resulting CE-WE current (figure 2.8b is recorded and plotted in a i-E plot called voltammogram[5].

To understand the shape of the voltammograms must recall the Nernst equation 2.4 that describes how the concentrations varies on the electrode surface related to the electrode voltage. When the potential is scanned during the CV experiment the concentration of the species in solution near the electrode changes oxidizing or reducing the analytes and generating a current. The peak current is dictated

[5]In this work we adopted the IUPAC convention for axes directioning

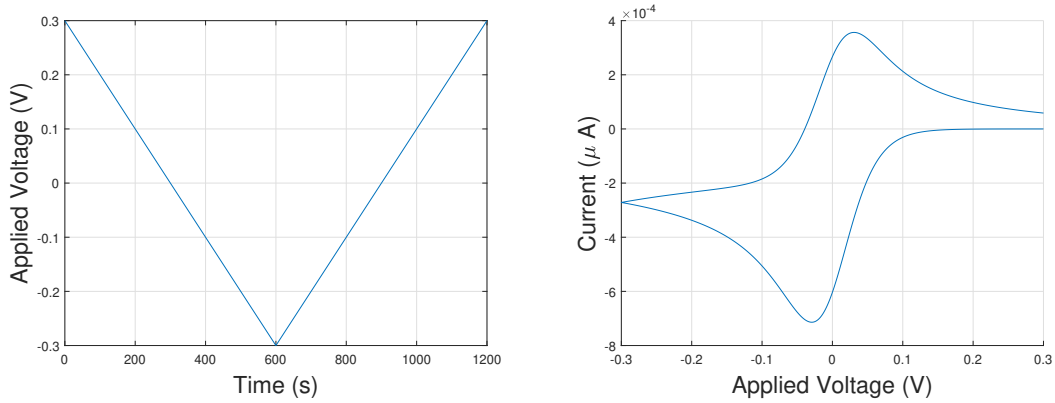

(a) (b)

Figure 2.8: Theoretical signals that compose the various aspects of a cyclic voltammetry. In (a) the potential applied to the cell over time is shown, while the obtained current (the voltammogram) is shown in (b).

by the delivery of additional analyte via diffusion from the bulk solution creating a diffusion layer that grows throughout the scan. Increasing diffusion layers slow the diffusion process and thus decrease the measured current.

Assuming a electrochemically reversibile electron transfer process involving freely diffusing redox species, the peak current (i_p) can be described by the Randles-Sevcik equation 2.13.

$$i_p = 0.446nFAc^* \left(\frac{nF\nu D}{RT}\right)^{1/2} \tag{2.13}$$

According to this equation, the peak current is related to the analyte's diffusion coefficient D, as well as the number of electron that are involved in the redox reaction n, the absolute temperature T and the scan rate ν of the experiment. Moreover, it is directly proportional to the bulk concentration c^* of the solution and to the surface area A. It's possible to estimate the surface area performing different voltammetries varying the scan rate and leaving still all the other parameters.

Differential Pulse Voltammetry This technique was developed to further improve the sensitivity of electrochemical methods and it employs a differential measurement process. The applied voltage is provided as a brief pulse and the output current is sampled in two different time instants before the rising and falling edges of the pulses. The two values are subtracted to obtain a differential measure. This differential measurements produces a peaked output rather than a voltammogram. This behavior can be qualitatively understood evaluating what happens at highly positives and negative overpotentials. When the potential is too low to stimulate

the faradic current flow, the pulse is to small to stimulate the faradic process itself and thus the current difference is almost negligible. On the other hand, when the electrodes work in diffusion controlled charge transfer (high overpotential), the voltage pulse is not able to further improve the current generation rate and thus the obtained current difference is again small. Only in potential regions where a small potential difference can make a sizable difference in current flow does the differential pulse technique show a response. The maximum produced by this measurement technique can be expressed with equation 2.14, where:

- $(\delta i)_{max}$: maximum value of the differential output current
- n: number of charges of the ions in the solution
- F: Faraday's constant
- D: Diffusion coefficient of the analyte
- c^*: Bulk concentration of the analyte
- $\tau - \tau'$: Time interval between the two current measurements
- A: Electrodes Area
- $\sigma = \exp \frac{nF}{RT} \frac{\Delta E}{2}$
- T: absolute temperature
- ΔE: applied voltage pulse

$$(\delta i)_{max} = \frac{nFAc^* \sqrt{D}}{\sqrt{\pi(\tau - \tau')}} \cdot \left(\frac{1 - \sigma}{1 + \sigma} \right) \tag{2.14}$$

Chapter 3

First Prototype

3.1 Introduction

Real-time measure of muscular fatigue during physical exercises is highly demanded in both hospital and home-based rehabilitative and physiotherapy sessions [83]. The possibility to provide patients and medical personnel with feedback on the intensity of the muscular effort can help to improve the outcomes of each specific session, thus avoiding overload and preventing injuries [84], in particular for more fragile patients (chronic patients or elderly) [85], [86]. The main parameters currently adopted to measure muscular fatigue are related to the estimation of changes in the mean and median frequency of electromyographic (EMG) spectrum. This information can be successfully obtained relying on well-established off-the-shelf solutions (e.g. adhesive pre-gelled surface electrodes, commercial dry electrodes), which allow the acquisition of electrical signals during muscular activity [87]. Recently, considering the extreme complexity of the metabolic processes involved with fatigue onset, an increasing interest has been addressed in the study of the biochemical profile of patients undergoing physical exercises, including both electrolytes and metabolites [88], whose balance is well-known to be altered during physical exercises [89]. Examples of biochemical markers investigated as possibly related with fatigue processes include electrolytes (potassium, sodium and chloride), amino acids and proteins (interleukin-8), metabolites (lactate) and, possibly according to more recent investigations, also urea and ammonium [90]. Among them, lactate is one of the most suitable candidate as a non-invasive biomarker of fatigue, since it is well-known to be formed and accumulated in the muscle under conditions of high energy demand [91] and insufficient supply of oxygen [89]. Confirmed correlations between the increment of blood and sweat lactate concentrations ensure the possibility to adopt lactate concentrations in the sweat as a reliable and non-invasive quantity easily measured with a non-invasive sensor, reflecting

changes within the organism [92]. Furthermore, the large concentration of lactate in the sweat (10-100 mM) and the large variation of this metabolite after physical exercises (up to 10-fold), enables the possibility to monitor fluctuation quite easily [88] with respect to other electrolytes or metabolites that, on the contrary, present lower sensibilities. Despite the mechanism of lactate production due to low level of muscular oxygenation is well-known, several aspects regarding the correlation of its variations with muscular fatigue-specific phases are still under investigation [84]. For this purpose, the simultaneous comparative analysis of lactate concentration levels and of the corresponding local muscular electrical activity could provide more in-depth knowledge of these physiological parameters that could really bring a revolution in smart rehabilitative devices, also outside medical laboratories and hospitals. Sensing devices currently commercially available for EMG and lactate monitoring present some limitations in terms of integration, personalization, invasiveness and possibility of a continuous and simultaneous recording of those signals. They often involve complex protocols for electrodes positioning that require the presence of medical personnel even in very simple treatments and analyses [93]. Furthermore, despite quite good results were obtained with novel printing technologies in terms of both conformability and sensitivity both for EMG [94] and lactate [95] monitoring are currently available as stand-alone measuring systems. Therefore, data obtained from these sensors require a careful temporal and spatial alignment, in order to enable a correct correlation between information obtained independently from these two kinds of sensors. This makes it particularly difficult to combine the different fatigue-related parameters extracted from the measurements performed with each single sensor [96]. Smart and totally customized multi-sensing printed wearable systems represent a great opportunity for better investigating the correlation between different biomarkers, exploiting machine learning techniques [97]. Furthermore, a real-time analysis of EMG and lactate concentration levels could enable suitable measure of fatigue even during exercise without medical personnel supervision, thus reducing the risk from low oxygenation of the muscles and maximizing the outcome of rehabilitative gestures [98]. Currently, the main challenge to develop a multi-sensing printed patch reliable for those medical evaluations is to ensure together with cost-effectiveness, user-friendliness, integration and unobtrusiveness also proper metrological performances (LOD, repeatability, selectivity, stability) during long-term applications. A relevant and novel opportunity is given by the most recently emerging non-contact printing techniques[94] (micro- or nano-pen printings, laser printing, Aerosol Jet Printing) that are aiming at optimizing conductivity, repeatability and stability of printed biosensors, reducing the dimensions of droplets, through a fine control of printed tracks or optimizing ink post-processing (e.g. photonic curing) are under investigation to optimize ink [99].

NOTE: The results presented in this chapter were published and summarized in [66], [100]

3.1.1 Aim

In this first prototype, a flexible multi-sensing platform realized by the emerging Aerosol Jet Printing technique [97], which allows integrating different transducing principles in the same device [99] and miniaturizing in a small wearable device both sensors and conditioning electronics is proposed. Here, a preliminary analysis of the design choices is presented as well as the first results. From those a set of further steps is then derived.

3.2 Multisensing System Design

3.2.1 Set Up Design

In this section, the geometrical design of the integrated EMG-lactate multi-sensing system is described. For what concerns the monitoring of electrical activity, EMG electrodes have been arranged in a matrix in order to monitor activation patterns as well as different fatigue conditions on different regions of the muscles, as validated in our previous research [101]. As previously mentioned in the introduction of this paper, to obtain further information on the physiological state of the muscle, an electrochemical enzymatic biosensor was introduced to sense lactate in sweat. We have chosen to integrate a lactate sensor in the middle of the EMG electrode matrix to collect punctual information on the analyte concentration in the whole surrounding area. One of the main requirements of the proposed multi-sensing system consists of enabling real-time monitoring of the considered physiological parameters. Therefore, it is very important to avoid possible sweat accumulation on the working electrode that could result in a sensor saturation. For this reason, the electrodes have been integrated with a simple paper-based microfluidic path, developed using Whatman chromatographic paper grade 1 (GE Healthcare, Little Chalfont, Buckinghamshire, U.K.). It comprises a sample pad and a reservoir. The sample pad is interfaced from one side with the surface of the working electrode with the layer of enzyme and mediator, and from the other with the skin collecting the sweat to be analyzed. The reservoir was designed with bigger dimensions thus to guarantee a continuous flux of sample onto the measuring point, driving away the excess of sample. Finally, particular attention was addressed to the multi-sensing system geometrical shape. In fact, if from one side a very small form factor is desirable to guarantee a high level of wearability, thus allowing the users to comfortably wear the device during physical exercises, on the other side crosstalk

interferences among the different signal paths due to parasitic capacitances may result in high signal degradation. A possible solution to overcome this problem consists in the choice of a double-layer architecture. On the top layer (L1), we have printed all the lines and the pads, while on the bottom layer (L2), we have printed the electrodes that will be directly in contact with the skin. The electrical connection between the two layers was realized through vias. This approach also eased the connection between the electrodes and the measurement systems thus improving both the electrode-skin contact and the overall user comfort.

3.2.2 Printing Process

Aerosol Jet Printing (AJP) technique allows a fast prototyping and optimization process that results to be particularly useful in the realization of customized sensors. We employed two different functional inks: Metalon HPS-108AE1 silver ink by Novacentrix (Austin, TX, USA) and EXP 2652-28 Carbon ink by Creative Materials Inc. (Ayer, MA, USA). The former was used to print all the conductive tracks, pads and electrodes, while the latter was used for working and counter electrode of the electrochemical sensor. We selected polyimide (Kapton) as a substrate, which presents outstanding chemical and mechanical characteristics that permit performing on it different curing and functionalizing processes [20]. Moreover, it is a lightweight and flexible material that well fits our needs as a comfortable patch. It is interesting to briefly consider the fabrication process for the integrated patch, which main steps are illustrated in the scheme of figure 3.1.

Firstly, the substrate is cleaned with ethanol (a). Then, the silver tracks are printed on the top layer L1 (b). The ink is oven-dried at 140 $°C$ for 5 minutes and then the vias are drilled in place (c). The subsequent silver deposition on the bottom layer L2 deposed both the electrodes and provides electrical connection to the other layer through the vias (d). After the oven-cure (200 $°C$ for 60 minutes) of the silver ink that concludes the fabrication of the EMG electrodes, the carbon layer was deposed on the working and counter electrode of the electrochemical sensor (layer L2) and cured at 140 $°C$ for 5 minutes (e). All the printing parameters adopted are detailed in table 3.1 and the resulting final prototype is shown in figure 3.2.

3.3 Multisensing System Preliminary Testing

EMG and lactate sensors rely on a very different transducing principle and for this reason, they need to be separately analyzed to address their most relevant and specific aspects. In this section, we provide the results obtained from impedance and EMG signal measurements performed to test EMG electrodes, and from elec-

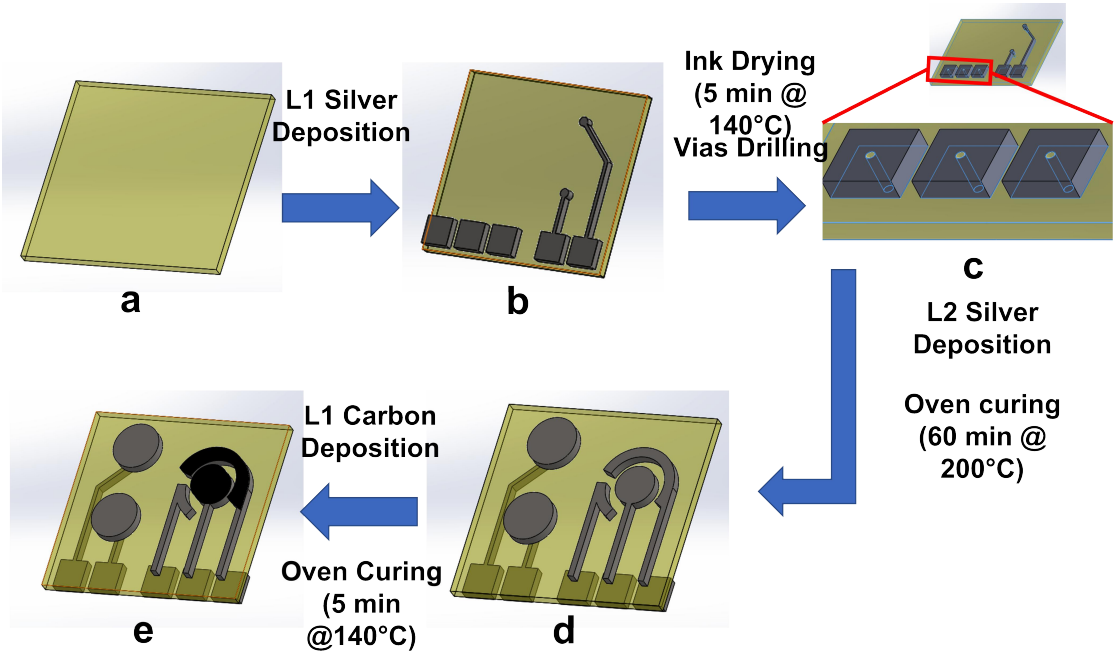

Figure 3.1: Overview of the different steps of the electrodes fabrication process

Table 3.1: Process parameters employed during fabrication

	Silver Ink	Carbon Ink
Sheat	500 SCCM	625 SCCM
Atomizer	1050 SCCM	1150 SCCM
Exaust	1080 SCCM	1000 SCCM
Plate temperature	75 °C	75 °C
Process speed	3.5 mm/s	3.0 mm/s

trochemical measurements acquired to investigate active area of printed sensors and to study the relation between output current and lactate concentration in both static and dynamic conditions.

3.3.1 Analysis of printed EMG dry electrodes

3.3.1.1 Impedance-based analysis

In order to evaluate the performances of the electrodes directly embedded on the devices by means of AJP, we compared their electrode-to-skin impedance with the one of two types of commercially available surface electrodes: wet Ag/AgCl electrodes (Kendall), and dry electrodes (DRV175). For each electrode/subject

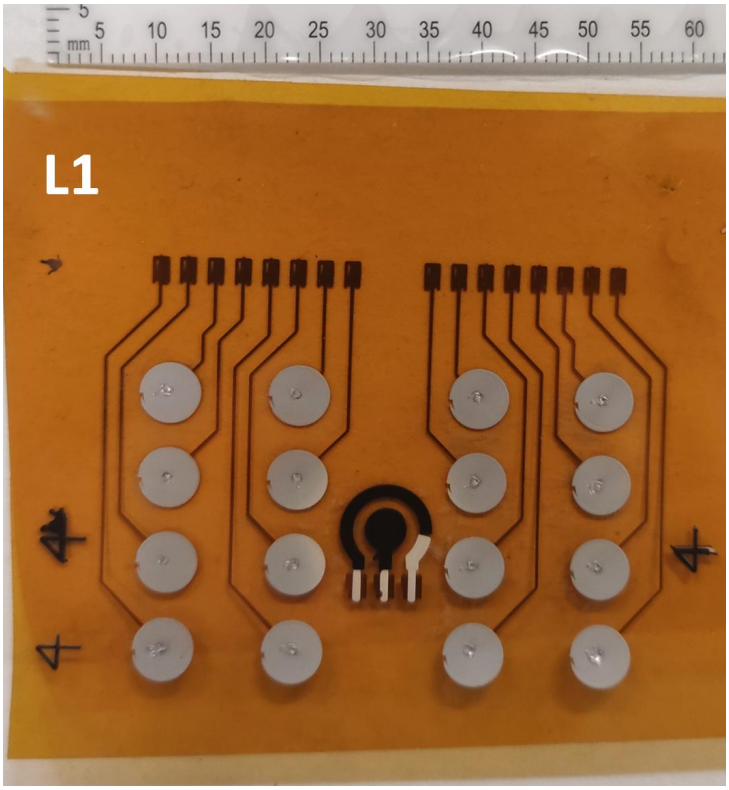

Figure 3.2: Final device that allows simultaneous measurements of lactate concentration in sweat as well as electromyography, thanks to eight EMG channels.

combination, three measurements were acquired at rest, placing a couple of electrodes on the gastrocnemius muscle of two healthy volunteers. Only for the dry electrodes, a set of measurements with water-humid skin were acquired to simulate sweating. All the measurements were acquired with a portable impedance analyzer (Palmsens3 EIS), configured to record impedance sweep in a range of frequencies from 10 to 1000 Hz, comprising the range of interest of EMG signal. All the measures were normalized with respect to the active area of the electrodes to provide better means of comparison. Both an intra- and an inter-subject analysis were performed. As highlighted from figure 3.3, the comparison among electrodes on the same subject showed a great similarity between our AJ printed electrodes and the commercial dry ones, with a difference around 20% for magnitude spectrum with sweat and a difference of around 46% without sweat. Regarding inter-subject variability, as highlighted from the average impedance for two subjects in each configuration shown in figure 3.4, comparable results could be obtained. The differences in terms of magnitude can be explained taking into consideration the variability in inter-subject device positioning, subject training and muscular anatomy. Moreover, the EMG electrode impedances were measured

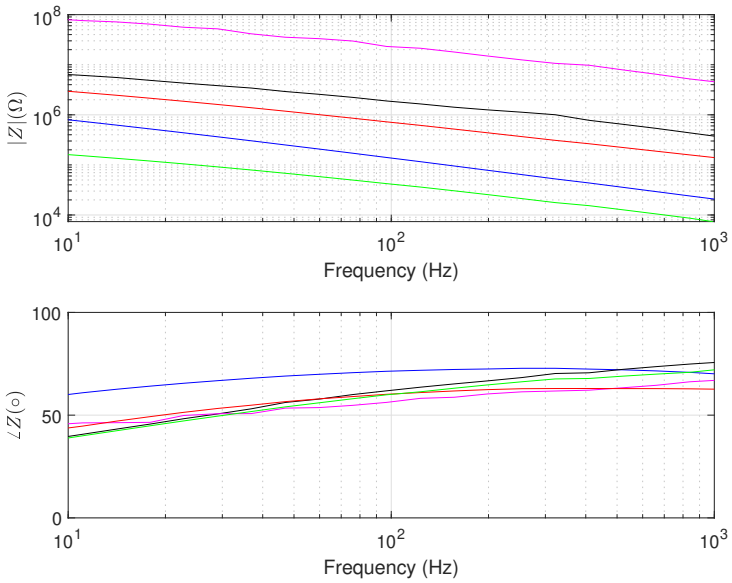

Figure 3.3: Comparison of the impedance of different electrodes on subject 1. Wet commercial electrodes in blue, commercial dry electrodes with/without sweat in green/black and AJ printed dry electrodes with/without sweat in red/magenta.

in a second session on the brachial biceps of a single subject during a 90 minutes period. Data acquired from each different EMG electrode were averaged, linearly fitted and their slopes compared of standard wet Ag/AgCl electrodes (Kendall), as reported in the literature [102]. This comparison is reported in figure 3.5 that shows that the two kinds of electrodes present a similar behavior in frequency, even though the average magnitude of the commercial electrodes is 20% of the one of the printed electrodes in all the frequency range tested. Analyzing then the variation over time of the contact impedances of the printed electrodes (figure 3.6) we can observe that impedance magnitude decreases quickly and tends to stabilize over time. In detail, the percentage average variation calculated between the two first successive measurements is 16.7% and it decreases to 3.3%, reaching a condition of stabilization after 60 minutes. This variation can be explained considering the formation of sweat at the electrode-skin interface that reduces the overall impedance. While the sweat layer is forming the impedances change and then stabilizes when the layer becomes uniform.

3.3.1.2 EMG acquisition and feature extraction

EMG electrodes were evaluated while acquiring a real contraction on one of the 8 channels. In particular, the possibility to follow the evolution of the main fea-

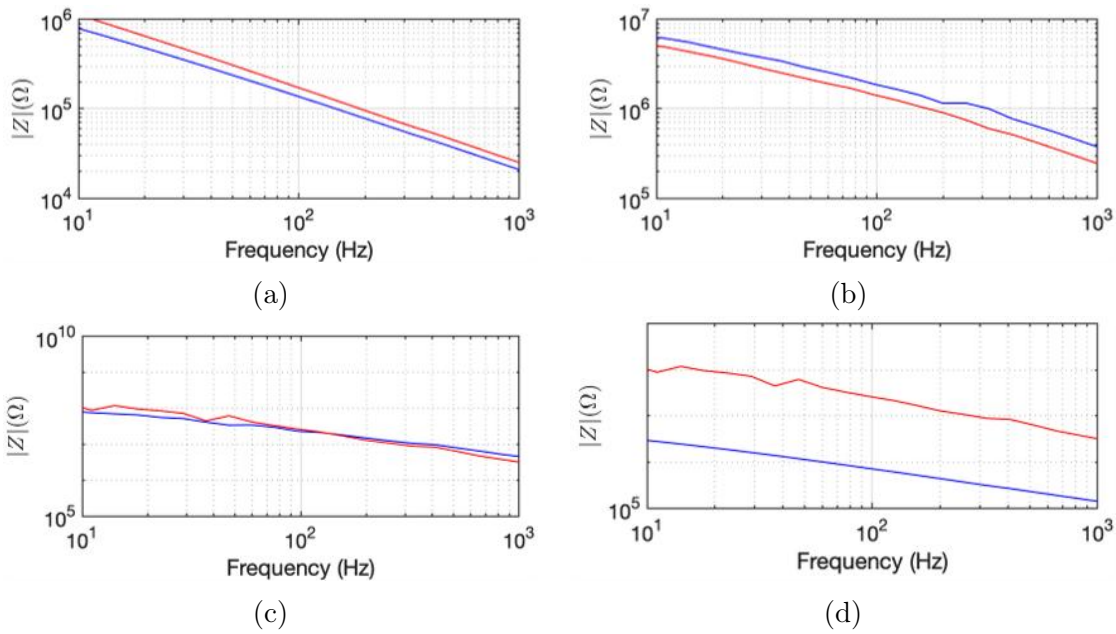

Figure 3.4: Comparison of the impedances of same electrodes between the two subjects (1 in red, 2 in blue). Wet commercial electrodes (a), commercial dry electrodes without sweat simulation (b) and AJ printed dry electrodes without/with sweat simulation (c)/(d).

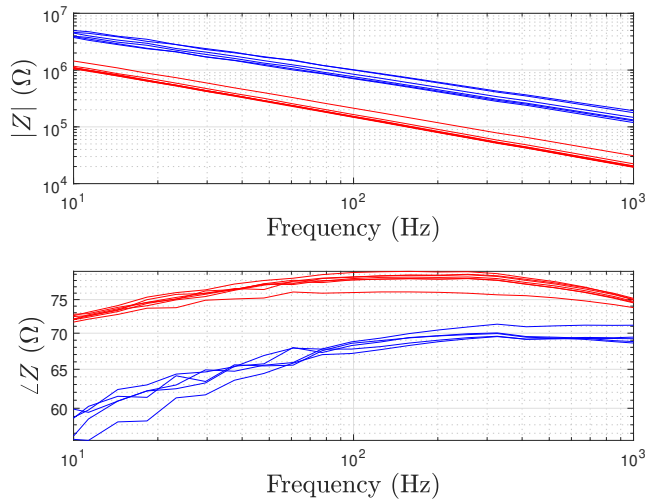

Figure 3.5: impedance comparison between our printed electrodes (blue) and the commercial ones (red).

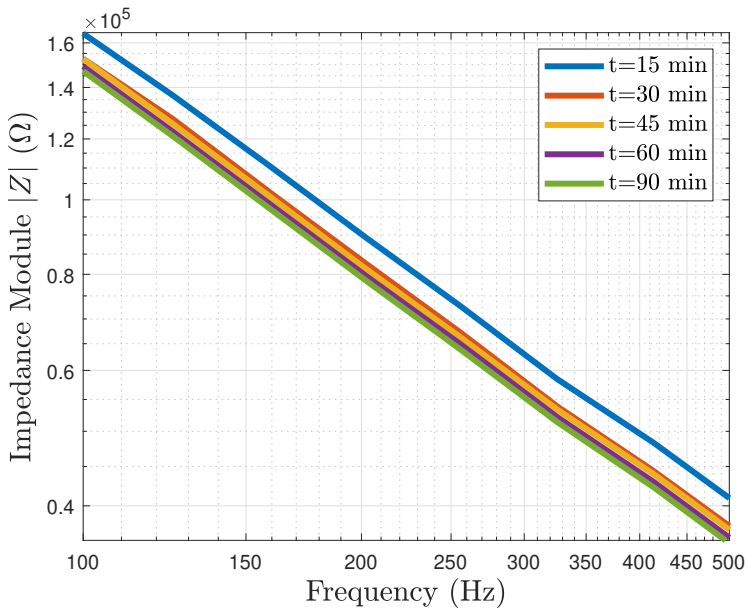

Figure 3.6: Detail of the impedance module of the printed electrodes over a 90 minutes period in the [100-500] Hz frequency range.

tures required to assess fatigue onset (mean and median frequency) during time measuring EMG during a single maximal contraction of the right gastrocnemius of a healthy volunteer standing on his toes. To simulate a fatigue condition, two recordings of 60 seconds were performed, the first one with the subject starting from a recovery condition and the second after running for 20 minutes. A decrease of both voltage amplitudes in the time domain (RMS value reduced of the 40%) and of the frequency peak of the frequency spectrum (peak shifted of almost -40 Hz) could be observed in the contraction recorded after physical exercise with respect to the contraction after rest. The analysis of frequency spectrum shows comparable frequency content, with most of the energy (75±3)% comprised within 20 and 250 Hz, in agreement with what was reported from the literature [103]. Regarding mean and median frequency, different trends could be appreciated for the two different repetitions, before and after intense physical exercise. While the first repetition showed a quite constant value of mean and median frequency during the contraction time, the second repetition showed decreasing trends. In both cases, the ranges of mean (170-190 Hz) and median (140-170 Hz) frequencies computed appeared in agreement with what the literature reports as the range in which the maximum EMG energy is located [104]. This result appears as a promising starting point to confirm the possibility to adopt this patch for monitoring fatigue during physical exercises. Moreover, the ability of the patch to acquire different channels was evaluated in another experiment whose aim was to derive multiple

information about the signal direction and spatial muscle activation with minimal invasiveness. Briefly, a subject was required to stand up from a chair and then sit again. The system was placed again on the gastrocnemius muscle. Then in post-processing, it was possible to extract color maps that are visually showing the activation of the different muscles during the task (Figure 3.7).

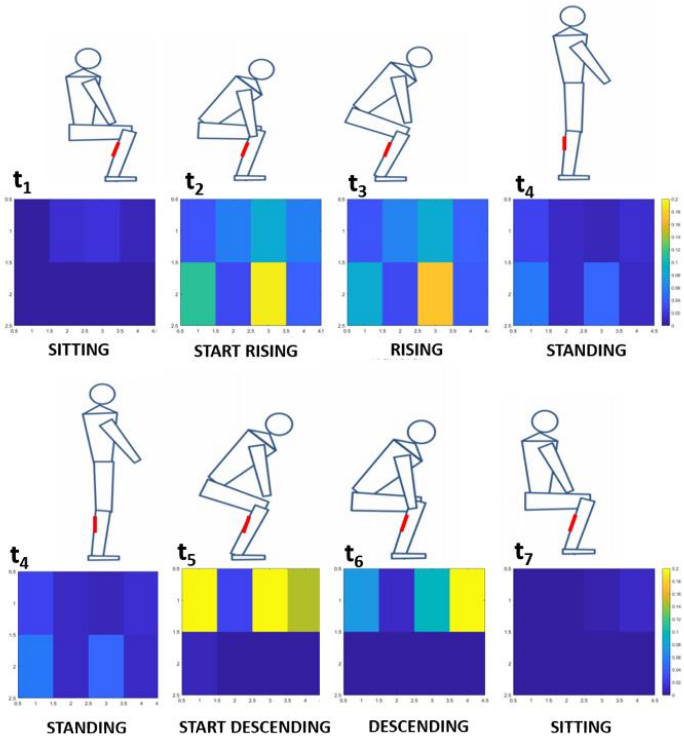

Figure 3.7: Spatial features extracted during task showing in each pixel the activation of a channel during the different phases of the exercise.

The correlation among the different channels confirmed that the highest value was obtained with an average delay of (0.03 ± 0.01) s among channels 1, 8 and 6 referring to the highest part of the muscle and among channels 5, 4 and 7 referring to the lowest part in each of the three subjects, suggesting the activation of the lowest part during rising and of the upper during descending (Figure 3.8). Interestingly, the highest correlation values (> 0.95) could be observed at delays in agreement with the distances between the peaks of RMS recorded on the different channels. In presence of a delay 0 and 0.2 s, maximum values of correlation would be observed respectively between nearby channels (e.g. among upper 1,6,8 and lower 2,4,5,7). At higher delays 0.8 and 1 s, maximum levels of correlation could be observed even between upper and lower channels. This can be comparable with the interval between rising and descending tasks, suggesting that the matrix

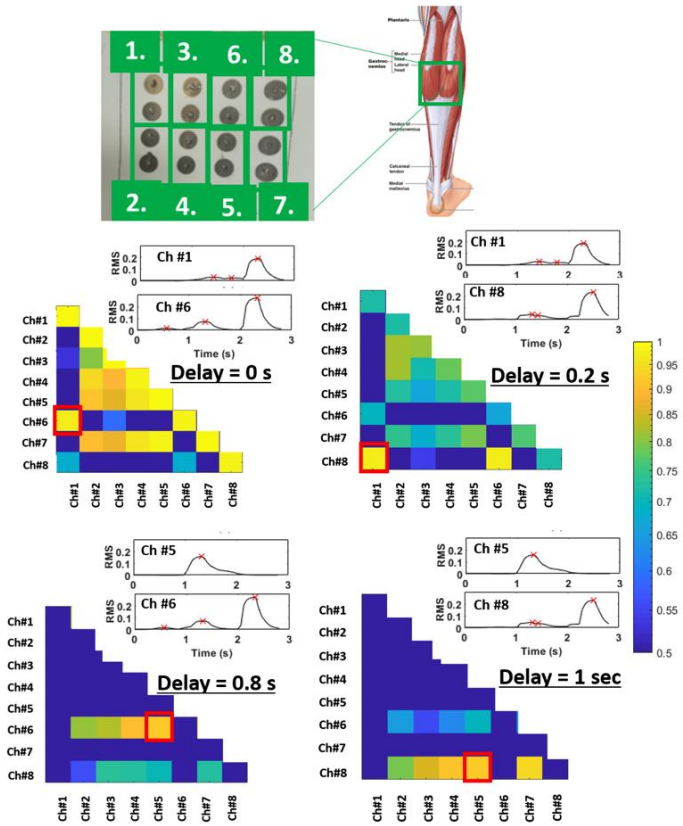

Figure 3.8: Maximum correlation values among the 8 channels during sit-to-stand and stand-to-sit tasks.

is successfully able to detect the different timings of activation of muscle with a higher resolution than classical single-channel EMG.

3.3.2 Analysis of printed lactate sensor

3.3.2.1 Electrochemical analysis

The first test involved the evaluation of the electroactive surface area (A_{real}) from Randles-Sevcik equation for a reversible reaction, as described in [103], by performing Cyclic Voltammetry (CV) at 0.1 V/s scan rate (ν) in a phosphate buffer saline (PBS) (50 mM, pH 7.0) containing a 5 mM concentration (C) of ferro/ferri-cyanide ($[Fe(CN)_6]^{3-/4-}$). Indeed, the electrochemical couple Fe^{2+}/Fe^{3+} redox process has a very well-known diffusion coefficient ($D = 6.20 \cdot 10^{-6} cm^2$). Furthermore, the effect of scan rate on oxidation and reduction currents and potentials was tested performing multiple CVs in the presence of 5 mM $[Fe(CN)_6]^{3-/4-}$ at different scan

rates (50, 100, 200, and 500 mV/s) in the potential range -0.6 to 0.6 V using the abovementioned potentiostat configured to perform CV. All measurements were performed in triplicate. The average active area calculated from the Randles-Sevcik equation was $(22.25 \pm 1.85)\ cm^2$, with a relative standard deviation (RSD) of 8%, confirmed a high reproducibility of the active area obtained with AJP, as demonstrated in previous works [102], where this technique was shown to ensure a lower variability when compared to SP, reducing RSD from 30 to 10%. The scan rate test (figure 3.9) allowed to confirm the linearity of both oxidation and reduction peak currents with respect to the square root of scan rate, indicating a diffusion-controlled redox reaction. Furthermore the ratio between the anodic and cathodic peak current near to unity for each scan rate and the independency from the scan rate of cathodic and anodic potential, suggesting a reversible behavior of the overall known reversible redox systems such as the ferri/ferrocyanide ones [105].

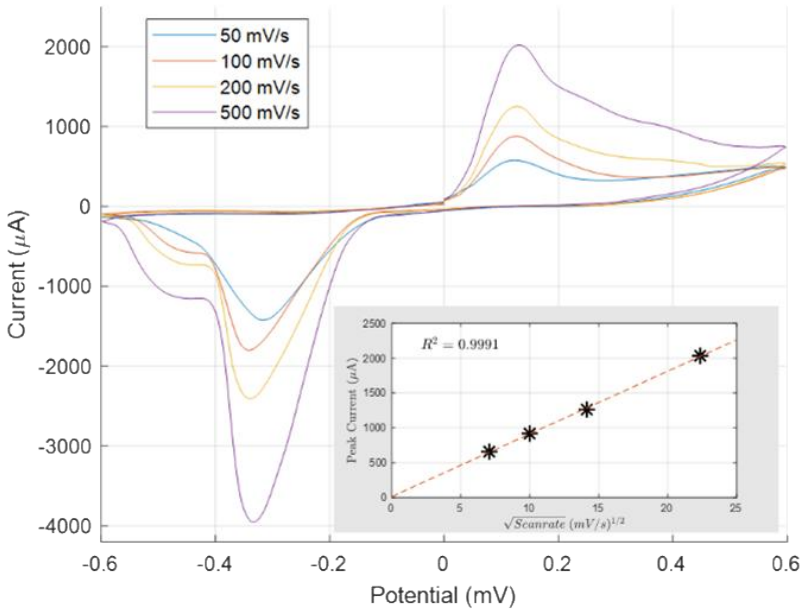

Figure 3.9: Electrochemical analysis at varying scan rate: in the zoom relation between scan rate square root and current of the peaks, confirming reversibility of ferrocyanide redox reaction.

3.3.2.2 Lactate static sensing

The second test performed on the lactate sensors was a static analysis. This test allows evaluating some important parameters of this printed chemical sensors

for an enzymatic lactate detection, i.e.: limit of detection (LOD), linearity and sensitivity. For each test, the platforms have been previously functionalized with 5 μl of 5 mM $[Fe(CN)_6]^{3-/4-}$ as mediator [54] and left drying at room temperature for 2 hours, protected from light. Dry L-lactate Oxidase (LOx) (Sigma Aldrich) was subsequently dissolved in PBS at a concentration of 100 U/ml and 5 μl of the solution was cast onto the WE and left drying for 2 hours. Standard solutions of sodium-L-Lactate (Sigma Aldrich) have been prepared in PBS with the following concentrations: 0 mM, 10 mM, 20 mM, 50 mM, 100 mM, 250 mM. 500 mM. For each concentration, 100 µl of the solution was placed onto the three electrodes layout using a micropipette, starting the chemical process described by equations 3.1 and 3.2 [106]. In detail, LOx catalyzes the oxidation of L-lactate to pyruvate, producing hydrogen peroxide (H_2O_2) that is then oxidized to produce a current proportional to the L-lactate concentration. A ferrocene mediator is employed to shuttle the electrons between the enzyme and electrode.

$$L - lactate + O_2 \rightarrow Pyruvate + H_2O_2 \tag{3.1}$$

$$H_2O_2 \rightarrow O_2 + 2H^+ + 2e^- \tag{3.2}$$

Five seconds after loading the sample, a potential of +400 mV vs. Ag/AgCl was applied and chronoamperometric measurements were recorded for 70 s with the abovementioned potentiostat. The average current value of three samples from each concentration at 70 s was taken as output to compare the different concentrations. Chronoamperometries obtained with different lactate concentrations (figure 3.10) suggested the possibility to correlate the increase in the steady-state current at 70 s with the increase of analytes concentration in all the range tested (from 5 to 250 mM).

The preliminary current-concentration plot obtained from the analysis of the chronoamperometric measurements (figure 3.11) suggest a higher linearity (R^2=0.9995) of the printed sensor in the range 0-20 mM. In this range a sensitivity of 0.39 $\mu A/mM$ was calculated, higher than the one observed in the full range tested 0-250 mM. The curve appears however to be linear also in the range 20-250 mM, with a R^2=0.9975 and a sensitivity of 0.15 $\mu A/mM$. This suggests a higher sensibility of the overall system for lower concentrations and saturation for higher lactate concentrations and appears in agreement with other work in the literature dealing with enzymatic detection on printed flexible electrodes [107]. Furthermore, the range of concentration measurable appear to be perfectly in agreement with the range expected from lactate concentration in sweat, typically from 10 to 100 mM depending on the level of exercise [108]. Usually lower than 20 mM at rest and higher than 70 mM during or after exercise [109].

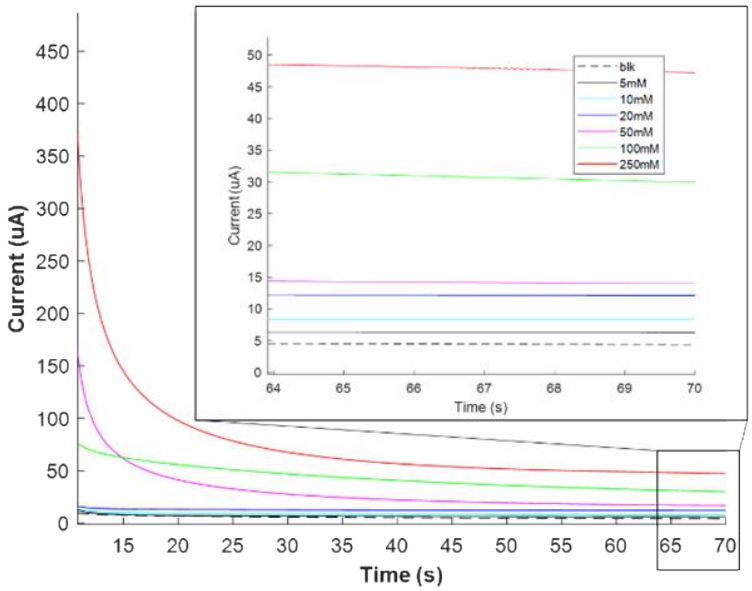

Figure 3.10: Chronoamperometries at different levels of lactate concentration. In the inset, it is highlighted the steady-state condition reach for all the concentration at 70 s, taken as reference.

3.3.2.3 Lactate continuous sensing

Aiming to a continuous and dynamic monitoring required in vivo sensing, after the measurements performed in static conditions a continuous monitoring of lactate variation in dynamic conditions was performed integrating the Kapton based patch with a paper-based microfluidic to facilitate from one side the immobilization of enzyme and mediator and from the other a proper flux of sample onto the testing point, as detailed in the setup design section (3.2.1). A preliminary analysis on the ability of the sensor to detect continuous changes in the concentration of lactate was assessed by first emulating the resting condition wetting the sample pad of PBS. In those conditions, the chronoamperometry was started applying a constant +0.4 V potential to the sensor and recording the current produced. After that, at discrete well-known time points (0 s, 125 s, 250 s, 400 s, 550 s) 50 μl of sodium-l-lactate PBS solution with different random concentrations were dropped onto the sample pad, emulating controlled increases of lactate concentration in the flux flowing onto the electrodes (figure 3.12). The measurement was performed in triplicate using the same set-up previously described for the other tests. The post-processing analysis of chronoamperometries was performed fitting each transitory after every time point with Cottrell equation and then calculating the difference between each deposition of lactate.

Results obtained appeared a preliminary promising starting point to enable a

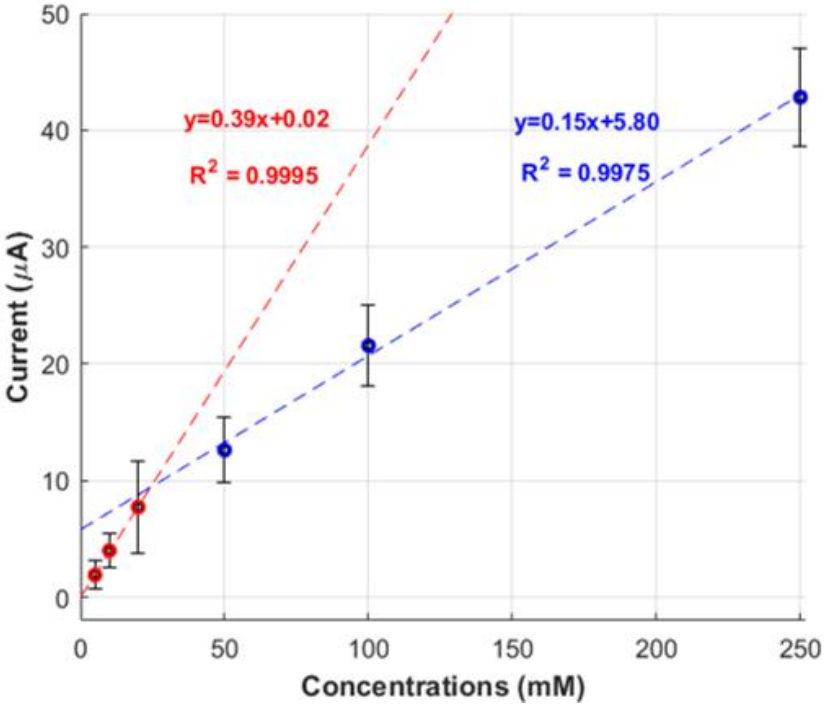

Figure 3.11: Current-Concentration plot of the whole range tested (0-250 mM), with linear fitting in the two ranges 0-20 mM and 20-250 mM.

continuous measure of lactate variation in sweat in a wearable device. The linearity (R^2=0.9816), the sensitivity (0.32 $\mu A/mM$) and the LOD obtained (4.1 $\pm$ 0.6) mM appear in agreement with what obtained in static condition but also from similar biosensors reported from the literature [108]. However, the lower sensitivity and absolute values of currents with respect to the static preliminary results, suggest that the main improvement need to be addressed to optimize the immobilization of the enzyme and of the mediator, in order to maximize electrons exchange, sensor stability and measurement repeatability even in presence of a flux of solution onto the sample pad.

3.4 Conclusions

This chapter shows a first prototype of an innovative fully printed flexible multi-sensing patch for unobtrusive and personalized fatigue measure during rehabilitative or physiotherapy sessions. By means of the emerging technique of AJP, a flexible patch easily integrable with any wearable device was developed, integrating on the same device: an 8 channel matrix for EMG recording, a three-electrode electrochemical sensor, printed connection for an easier interface with conditioning

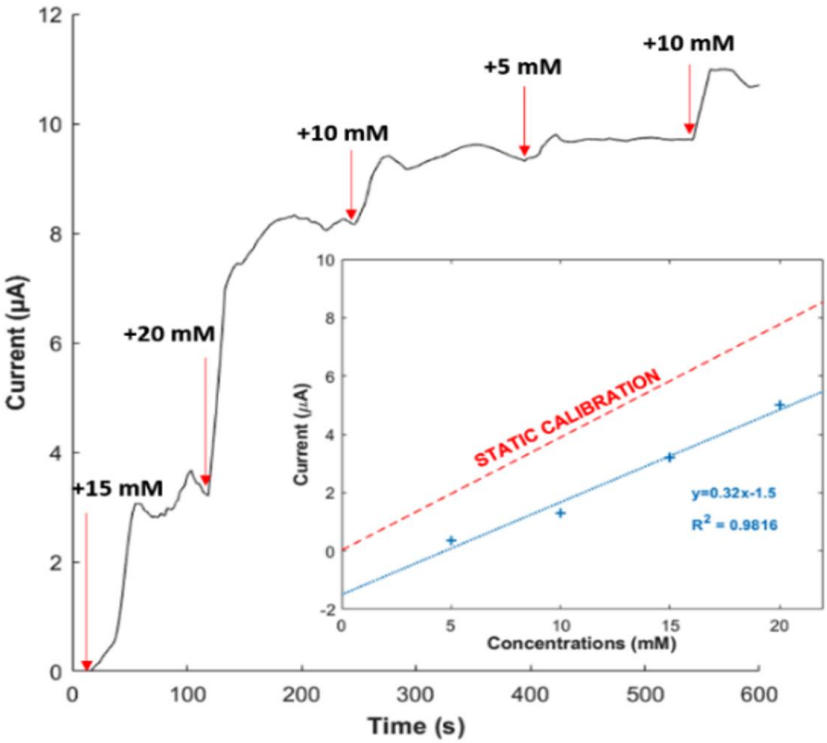

Figure 3.12: Current-Concentration plot of the whole range tested (0-250 mM), with linear fitting in the two ranges 0-20 mM and 20-250 mM.

electronics. Results of the measurements performed as preliminary analysis of both the sensors printed on the patch provided a promising starting point to pursue in the study a device able to follow changes in EMG features and sweat lactate variations during fatigue processes. The ranges recorded for mean and median EMG frequency and the decrease monitored after an intense effort suggest the ability of the device to monitor electrical muscular activity not in a single location, but over a large area. Regarding lactate sensing, preliminary results are a promising starting point suggesting the possibility to study the use of the current measured from the printed electrochemical sensor to follow lactate changes continuously within the physiologically range of interest for fatigue monitoring (10-100 mM). Further investigations are however needed to optimize the sensor design, to reduce the variability and improve the metrological characteristics of the sensors.

Future developments will need to address the improvement of the setup for continuous lactate monitoring, maximizing the stability of enzyme and mediator and the efficiency of electrons exchanges. In order to address the last issue, the structuration of the electrode surface is proposed in the literature to improve sensitivity and limit of detection of the overall devices. Starting from this consideration in the next chapters 4 and 5 two different fully printed nanostructuration approaches

are proposed.

Chapter 4

Microstructures

4.1 Introduction

As hinted before, in order to obtain continuous monitoring of the analytes, great attention is required in increasing sensor's repeatability, reusability and sensitivity as well as long-term stability [99]. Sensitivity is an important parameter in each application that requires measuring small variations of the analytes of interest. Specific functionalization techniques are usually employed to enhance sensitivity and selectivity [110]. In addition to bio and nano functionalization, one of the most relevant aspects of the surface of the electrodes that can influence both sensitivity and selectivity of the analysis is the micro-structuration [111]. Thus, the micrometric 3D structure of electrode surface can have a strong impact on analyte-electrode interaction, in terms of sample microfluidic and diffusion, and in terms of total surface area available for the reaction [112]. The micro-structuration of the surface of the working electrode usually aims at producing array patterns or increase the electrode porosity [113]. The latter is usually obtained using electrochemical processes [114] and aims to adsorb analytes while the former is often based on well-defined geometries like pillars. Pillar-based structures are well explored in the literature where different parameters like pillars width, distance, layout and shape are taken into consideration [115]–[117]. Those affect two main parameters: the before mentioned surface area and the diffusion layer of the analytes. The latter is because 3D features have a non-planar diffusion layer and that can interact with the produced current if the diffusion layers of different 3D features overlap or not [116].

The results presented in this chapter were published in [118].

4.1.1 Aim

Aim of this section of the work is to investgate the possibility to print 3D microstructures in order to improve the sensibility of electrochemical sensors.

4.2 Materials and Methods

4.2.1 Electrode Design and Fabrication

As exposed before, electrochemical sensors relate the flow of electrons to the concentration of electroactive species of interest (analytes) that undergo oxidation or reduction reactions. Those reactions take place if they are thermodynamically favorable (e.g. lowest unoccupied molecular orbital of the molecule has lower energy than the electrons in the electrode). Electrochemistry uses electrical potentials to change the energy level and thus ease redox reactions. This effect can be described through the Butler-Volmer equations that, however, do not fully consider how the concentrations of the analytes change close to the electrodes. This last issue can be addressed using Fick's laws of diffusion that allows describing the gradient of concentrations through time- and space-dependent differential models. As already exposed in the previous chapters, several techniques are reported to study these processes and for them are provided simplified relations to describe the current resulting from the experiments and their dependance on chemical and geometric parameters. One of the most important is the WE area, that can be controlled during the design process and it is directly proportional to the output current. Considering these evidences from the literature, the proposed 3D electrodes were designed to provide a $15mm^2$ WE base area and to fit in a 10×30 mm alumina substrate, compatible with commercial connector for screen-printed electrodes. A two-material architecture was selected to provide good electrode conductibility, stable RE and inert CE and WE. According to those choices, silver chloride (AgCl ink, XA-3773, Fujikura Kasei Co. Ltd., Shibakouen Minato-ku, Tokyo, Japan) was employed for conductive tracks, pads, and RE, and carbon (C ink, EXP 2652-28, Creative Materials Inc., Ayer, MA, USA) ink for WE and CE coating and further micro-structuration. A 3D render of the electrode structure is provided in Figure 4.1.

The sensors were produced using an Aerosol Jet Printer (AJ300, Optomec, Albuquer-que, NM, USA) in a five-step printing process shown in Figure 4.2. The substrates are initially cleaned in ethanol to remove possible contaminants and increase the adhesion be-tween ink and substrate. Then AgCl ink is deposed and cured at 120 °C for 20 minutes. Next, WE and CE are coated with carbon ink and then cured at 175 °C for 5 minutes. Those first steps were printed using a 750 μm head to coat the surface and obtain regular depositions, while the following fine

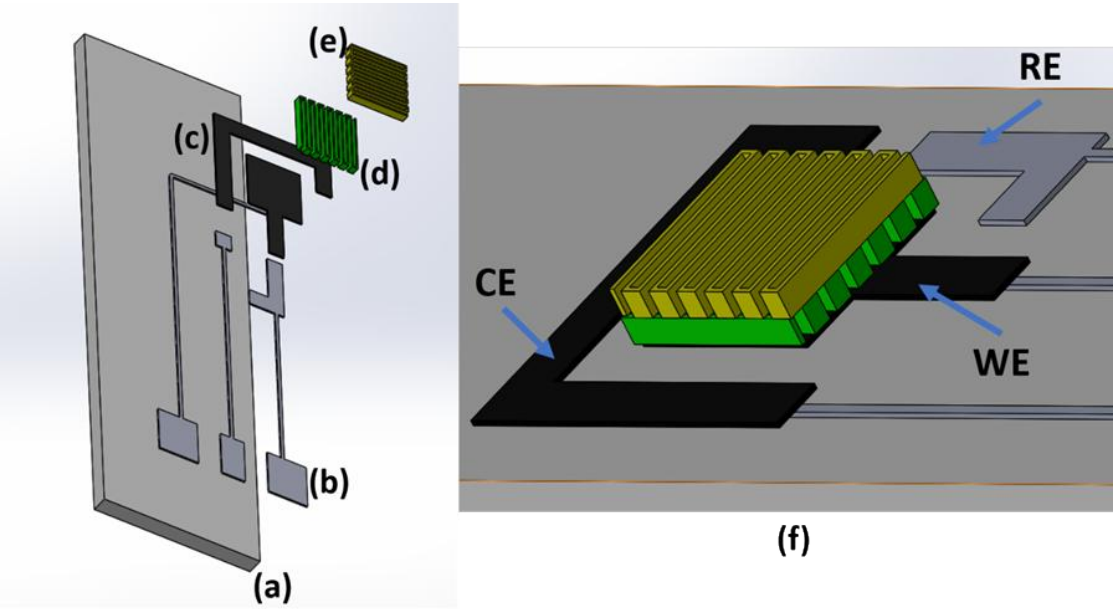

Figure 4.1: Render design of each layer of the sensor. Alumina substrate (a), AgCl conductive tracks (b), carbon coating (c), lines (d) and grid (e) micro-structuration. In (f) the stacked layers are depicted in detail. Unrealistic colors were chosen to enhance the visibility of each layer.

functionalization lines were printed using a 200 μm head to achieve a line width around 100 μm. The functionalization was printed in two successive steps divided and followed by the ink curing. After the first micro-structuration step, the second micro-structuration layer was printed. To provide a correct alignment between the different layers, a set of three four-shaped fiducials was inserted (Figure 4.2). Those were used to calculate the different positioning of the substrates during the production step and thus correct the printing path. Five sensors were produced after an accurate selection of the process parameters (reported in Table 4.1) like substrate temperatures and process speeds that promote the inks deposition. In figure 4.3 the output of each production step is depicted.

4.2.2 Physical and Electrochemical Evaluations

Electrical, morphological and electrochemical characteristics of the produced electrodes were evaluated after printing. The electrode resistances were measured using a 4-wire technique using a digital bench-top multimeter Hewlett–Packard 34401a (HP, Palo Alto, CA, USA) to evaluate the process variabilities. Geometrical features were evaluated using an Alpha-Step IQ Surface Profilometer (KLA-Tencor, Milpitas, CA, USA). Those first measurements aimed to evaluate the

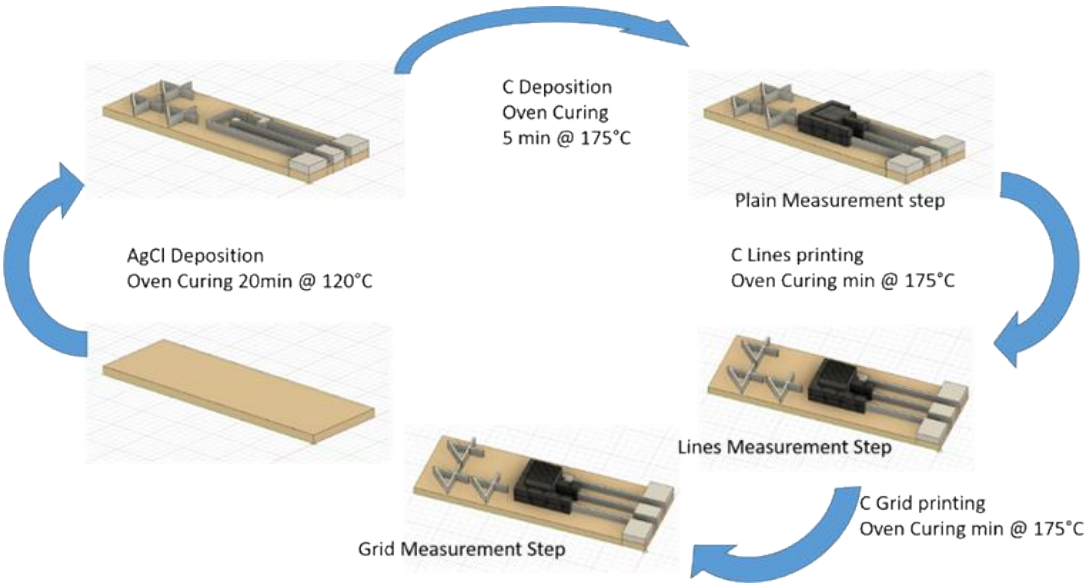

Figure 4.2: Micro-structured electrode production process

production process and identify drift and differences between electrodes. At first, we evaluated the profile of micro-structured lines produced on bare alumina. After performing electrode micro-structuration on 5 electrodes, their profiles were acquired and statistical analysis was performed. Each of the five profiles is divided into 13 signals that depict each a single micro-structured peak. Those signals were properly aligned and analyzed to obtain both the peak thickness and width. The former was evaluated as the mean of points that are at least 80% of the maximum acquired value. The average width was calculated as the distance between the points whose thickness was 10% of the maximum value. A similar evaluation was later performed on the produced electrodes on all two possible micro-structurations. Electrochemical evaluations were performed using a portable potentiostat Palmsens3 EIS (Palmsens, Compact Electrochemical Interfaces, Houten, Utrecht, The Netherlands). All the electrochemical experiments were performed in a Phosphate Buffer Saline (PBS) solution (50 mM, pH 7.0) as a supporting electrolyte and using ferro/ferri-cyanide ($[Fe(CN)_6]^{3-/4-}$) as analyte. The latter is considered a classical redox probe due to its well-known redox parameters [119], low cost and ease of detection that makes it a standard analyte for electrode characterization. Different preliminary electrochemical experiments were performed on the materials to define the best potential window from zero to one volt [0,1] V that allows the analyte detection without electrolyte interference. According to them, the measurement protocol was defined. Each session was started applying a constant 1 V bias to WE in PBS for 120 s, thus electrochemically cleaning the surface by stripping any deposited salt. Then 8 CVs (scan

Table 4.1: Printing parameters used during the production process.

	Conductive tracks, RE	CE & RE coating	Microstructures
Ink	AgCl	C	C
Sheat flow	250 SCCM	400 SCCM	40 SCCM
Atm flow	1100 SCCM	1150 SCCM	805 SCCM
Exhaust flow	1030 SCCM	1030 SCCM	790 SCCM
Substrate temp.	50°C	75°C	70°C
Process speed	3 mm/s	3 mm/s	2 mm/s
Number of Depositions	1	6	20

rate 0.1 V/s, voltage range [0 ;1] V) are performed in PBS solution to stabilize the electrodes and acquire blank voltammograms. Those first two steps were performed as a pretreatment technique to enhance the electrochemical activity of the electrodes and remove contaminants [120]. In order to improve the sensitivity and reduce the effects of the charging current, differential pulse voltammetry (DPV, pulse amplitude 0.2 V, pulse time 0.01 s, scan rate 0.2 V/s) was used to evaluate five different solutions with increasing ferro/ferri-cyanide concentrations (0 mM, 2 mM, 4 mM, 6 mM and 8 mM). At the end of those measurements, a DPV and four CVs in PBS are performed to collect information on adsorption. The experiment was concluded with a stripping equal to the first one to clean the sensor. On each electrode, all measurements were performed three times. The first on sensors with bare carbon WE and CE, the second after printing parallel lines on top of bare electrodes and the last one after the complete grid deposition. This procedure allows neglecting the inter-sensor variation and focuses on the intra-sensor variation due to the different functionalization. All the acquired measures were later elaborated using MATLAB R2019b to perform statistical analysis, data fitting and extract useful information on the overall behavior of the electrodes.

4.3 Results and Discussion

4.3.1 Physical Evaluations

The physical evaluations allowed characterizing the production process and evaluate their effects on the electrochemical performances. During the first two deposition steps, the resistance of each electrode was measured. The silver-silver chloride

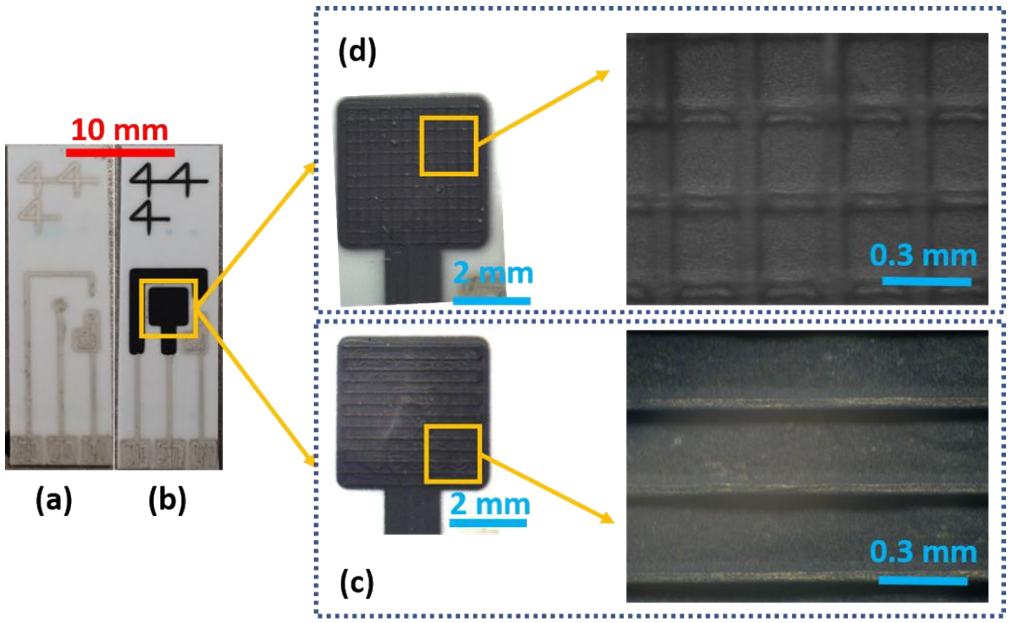

Figure 4.3: Step by step produced electrodes. (a) Silver Chloride conductive tracks and RE, (b) WE and CE carbon coating, (c) line micro-structuration, (d) grid micro-structuration.

tracks had different values according to their length. The average resistances are (15.44 ± 4.11) Ω for CE, (8.63 ± 2.50) Ω for WE and (6.97 ± 2.35) Ω for RE. The set of profile evaluations acquired after each deposition showed a low variability in the production process. In detail, non-micro-structured WE resulted (5.27 ± 0.76) μm thick on average with a mean width of (4.59 ± 0.70) mm. This ensures good coverage of the silver layer and guarantees a correct behavior of the electrodes preventing metal oxidation. In Figure 4.4, the average profile for the test line printed on the bare alumina is depicted. They present an average thickness of (58.20 ± 1.85) μm and an average width of (132.78 ± 5.67) μm. After this evaluation step, we printed the microstructure directly on WE surface, whose profile is shown in Figure 4.5. Analyzing the profile of those peaks we observed a similar average peak width of (130.09 ± 21.22) μm and a smaller thickness of (48.87 ± 13.86) μm. The comparison between subsequent deposition processes showed an increased relative standard deviation that suggests variability and drift in the deposition process due to the serial printing (the electrodes were printed one after another). Those differences can be also observed by analyzing the mean profile shape obtained on a single electrode. In Figure 4.6 it is possible to observe different peak profiles that are due to fluctuations in the process parameters. Similar phenomena were observed also on the grid microstructures. In this last situation, we obtained a (19.57 ± 8.71) μm average peak thickness and a (131.02 ± 19.37) μm average peak width.

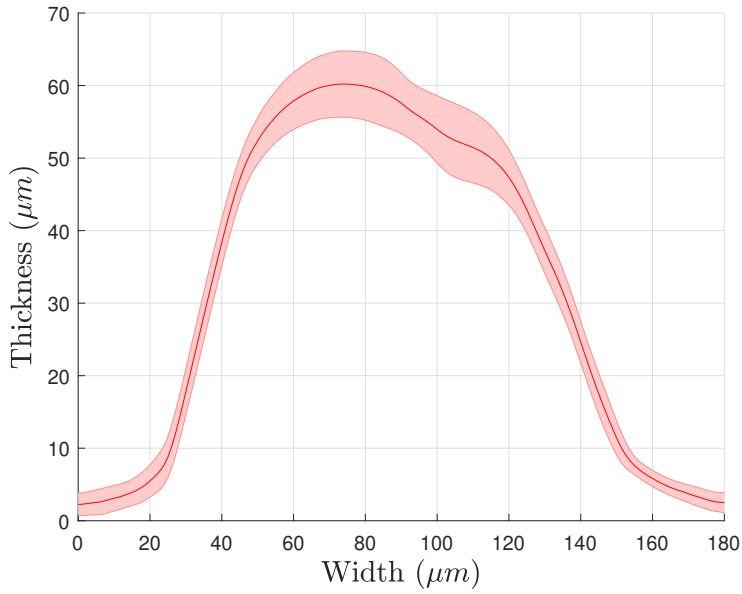

Figure 4.4: Micro-structuration profile obtained for test micro-structuration on bare alumina. The solid line depicts the average thickness of the peak while the shaded area represents the standard deviation. That statisti-cal information was obtained from 60 sample peaks

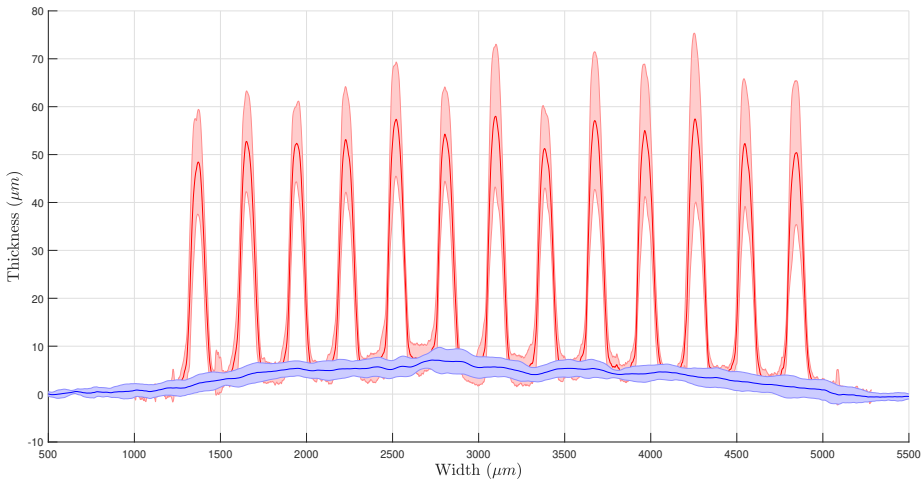

Figure 4.5: Average profiles of the WE of the produced electrodes. In blue are presented the bare WE, while the mi-crostructures are represented in red. As before, solid lines represent the average thickness and shaded areas represent the standard deviation.

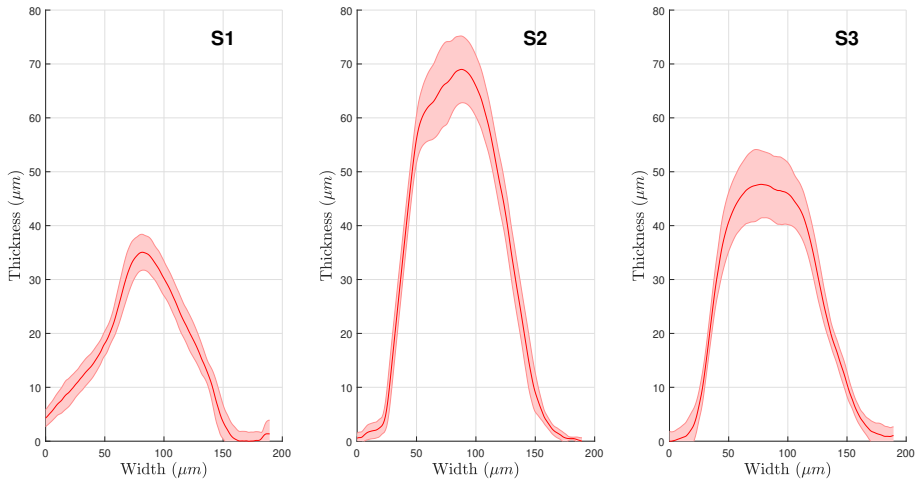

Figure 4.6: Average profiles obtained on different electrodes after the micro-structuration.

4.3.2 Preliminary electrochemical Tests

Preliminary experiments were performed to evaluate the feasibility of our approach and to determine important electrode's characteristics. At first different cyclic voltammetry (CV) experiments were performed both in pure PBS as blank solution and in ferro/ferricyanide solution. As reported in Figure 4.7, CV produced by the ferro/ferricyanide solution present two well-distinct peaks at 0.45V and -0.1V. As regards the CV produced by the blank solution, they present two spurious peaks at around 0.1V and -0.2V. Different potential windows were tested to minimize the impact of the undesired peaks. In the end, a [0,1] V potential window was chosen because it suppresses all the unwanted peaks and allows identifying the oxidative peak of the analyte of interest. In Figure 4.8, eight CVs obtained in blank solution for each sensor's micro-structuration are reported. CVs present similar peak currents and shapes. Moreover, a quick stabilization after only few cycles can be appreciated.

4.3.3 Electrochemical Evaluations

All the five sensors were tested using the aforementioned protocol that starts comparing the reaction of the three possible micro-structurations in a PBS blank solution. All the electrodes with all the microstructurations produce with DPVs similar blank electrochemical behavior, with a plain region in the [0.1 ;0.7] V potential window. This is convenient in our application where we expect from previous assessments a peak due to the ferro/ferricyanide reaction around 0.5 V.

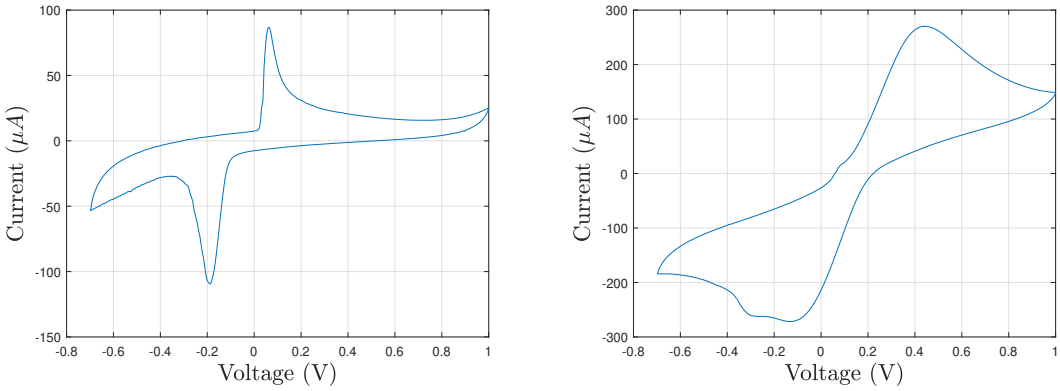

(a) (b)

Figure 4.7: Voltammograms obtained after two experiments performed in pure PBS (a) and in 8 mM ferro/ferricyanide solution (b) with a scan rate of 200 $mV \cdot s^{-1}$.

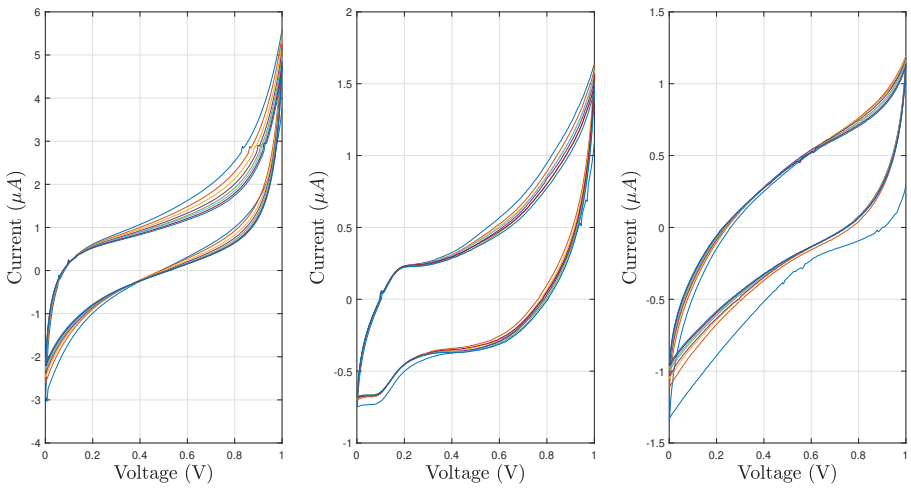

Figure 4.8: Voltammograms obtained by experiments performed in pure PBS for bare (left), line micro-structured (center) and grid micro-structured (right) sensors.

In Figure 4.9, the data collected from DPV performed on each configuration (bare, lines and grid micro-structuration) on a single sensor are reported. There, it is possible to observe an overall improvement of the peak current for each concentration. That implies ease of detection of the analyte using micro-structured devices rather than non-micro-structured ones. To further inquire about the sensitivity of our devices, the peak width was extracted through the PSTrace 5.8 software that provides both the peak current and position. The latter, expressed as peak voltage, is stable for all three configurations resulting slightly higher on average for plane electrodes at $(504.65 \pm 16.75)\ mV$, rather than line-microstructured $(479.75 \pm 37.94)\ mV$ and grid-microstructured $(468.94 \pm 22.92)\ mV$ electrodes. As regards the peak currents, each sensor was compared separately. In Figure 4.10, the peak currents are related to the analyte concentration to obtain three calibration curves for each sensor. Those curves resulted linear as expected from the theoretical background [81], [82].

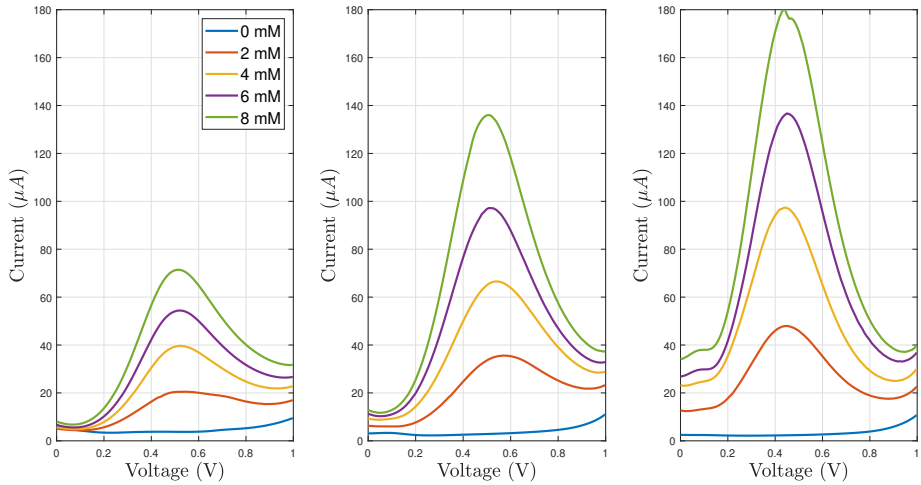

Figure 4.9: DPVs obtained on sensor S2 for the bare electrodes (left), lines (center) and grid (right) micro-structured ones.

Considering the sensitivity as the slope of the fitting line, it was shown that grid microstructures deposition improved the sensitivity with respect to the bare devices on average of 2.3 times, while the line microstructures produced an improvement of 1.5 on average. It was also shown that those micro-structurations do not interfere with the linearity of the device (the linear fit produced an $R^2 > 0.98$). The variability among the different sensors is due to the multiple variables that influence the electrochemical process. For example, the differences of the obtained micro-structured profiles play a major role in defining the different changes in the sensitivity of the sensors. In detail, it resulted that the line micro-structuration

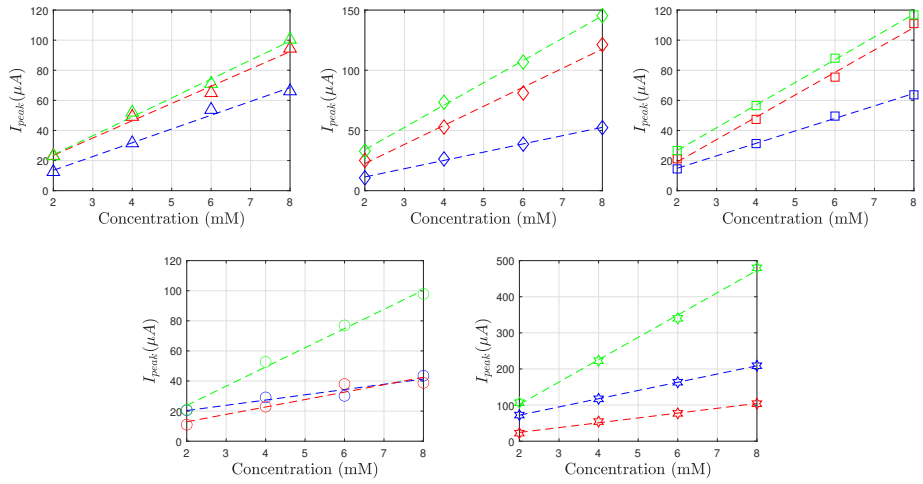

Figure 4.10: Sensors calibration points for bare (blue), line-micro-structured (red) and grid- micro-structured (green) electrodes. Dashed lines represent the best fit lines for each configuration.

for sensor S1 produced a 25%improvement of the sensitivity with an average peak thickness around 35 μm and an estimated added area of 8%, while sensor S2 experienced a 130% variation thanks to peaks up to 70 μm that produced an estimated added area of 33%. Those data present (figure 4.11) a linear dependence between the percentual increase of the slope and the one of area, as already foreseen by Cottrell 2.12 and Randles-Sevcik 2.13 equations.

4.4 Conclusions

In this chapter, a promising methodology to improve the sensitivity of electrochemical sensors exploring a third-dimension micro-structuration in fully printed devices realized by Aerosol Jet Printing was analyzed. Here a linear structure up to 70 μm thick with an average line width around 130 μm was obtained. The micro-structures permit to increase the surface up to 130% without changing the substrate occupancy. Our tests revealed that the micro-structuration process was able to increase the sensitivity of the electrodes on average of 2.3 times respect to bare electrodes. The proposed micro-structuration can be adopted in applications that require high sensitivity. Moreover, those geometrical features are comparable with the ones obtained in other works (as [112], [115], [116]) with lithographic processes instead of the hereby proposed fully additive, digital and maskless production process thus allowing greater flexibility and opening to new possible geometries. Future work will mainly address the improvement of the high process

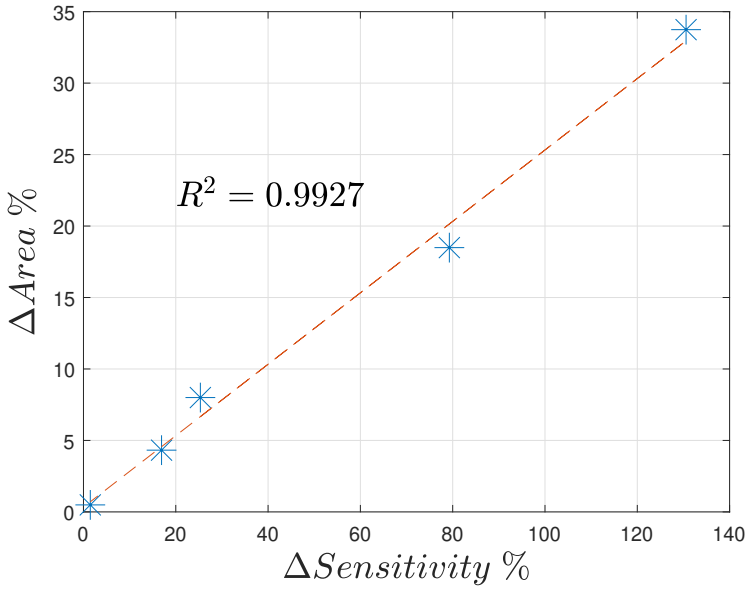

Figure 4.11: The obtained relationship between the micro-structuration-added electrode area and the increase in sensitivity. The blue asterisks represent the data points and the dashed red line is the best fit line that presents $R^2 = 0.9927$. The data for the added area were extracted from the profiles presented in Figure 4.6

.

variability obtained in this preliminary work by optimizing each production step for instance parallelizing the deposition and reducing the production time. Moreover, further work will experimentally inquire the limits of this approach in terms of maximum added area considering both the micro-structure spacing and their thickness. In particular, the latter is expected to present limitations due to the repeated deposition process that could modify the thickness-width ratio and the shape of the micro-structures limiting thus the effective improvement of sensitivity.

Chapter 5

Nanostructures

5.1 Introduction

In the previous chapter electrochemical transducers and electrochemical biosensors were introduced and their importance and their advatages were hinted. These are of particular interest because they allow real-time and/or continuous monitoring of the concentration of an analyte in a solution, with quicker response times, easier methodologies and fabrication than the standard detection methods. Moreover, they are easy to use, produce and miniaturize. That improves their portability that eases on-site monitoring and reduces the costs for the overall analytical process [61], [99], [121]–[123]. Despite these great advantages, electrochemical transducers are affected by many metrological issues such as limited stability, selectivity, repeatability and sensitivity [99], [122]. Most works in the literature aimed at addressing these issues by functionalizing the sensors with specific sensing layers and thus improving selectivity and sensitivity. As seen in the introduction, the possible functionalization layers include biomolecules but also other materials such as ion-selective membranes, imprinted polymers, nanostructures, microstructures [31], [124], [125]. Despite biomolecules offer unique advantages in terms of analyte recognition, they also introduce shelf life and storage issues that can limit their applicability out of laboratory conditions [126]. Thus, surface structuration of the electrodes exploiting more stable non-biological materials is explored. In the literature, nano-structuration is explored and seems to be a promising methodology to improve the system sensitivity [99], [118], amplify the sensors' signals [127] and to introduce enzyme-mimetic effects [128]–[130]. Those techniques, as well as the ones described in the previous chapter, aim to increase the electrode-electrolyte interface area and modify the mass transport processes in the proximity of the active electrodes [53], [118]. Usually, the nanomaterials used for electrochemical biosensors are divided into two groups: carbon-based and non-carbon-based. [53] The

latter presents a plethora of possible materials including for example noble metals (as silver, gold and platinum), silica nanoparticles and organic materials [131]–[133]. However, for their performances, commercial availability as well as their low toxicity, carbon-based nanomaterials are the most used in biosensing [134]. Thus, they represent an optimal trade-off among electrical properties, cost and biological compatibility [135]. Of course, one of the most crucial aspects to fully exploit these properties to improve metrological issues of electrochemical biosensors is the possibility to precisely control the deposition of these functionalization materials. Thus, uncontrolled and often adopted deposition protocols lacking reproducibility and geometry control (e.g., manual drop-casting), might influence the variability of the final results. In order to produce the devices was then selected again the Aerosol Jet Printing technology.

5.1.1 Aim

In this chapter, the production process of a simple fully-printed nanostructured electrochemical cell is proposed. AJP was used to fabricate the whole device starting from the bare cell deposition and then using two different commercial carbon nanostructures to functionalize the working electrodes. The aim was to provide a more general investigation of sensors as possible, as a starting point for translating sensor use in any areas previously mentioned (e.g. cellular processes, food control, clinical practice and environmental control). The printed sensors were tested, and the two different nanostructures were compared to evaluate their electrochemical behavior and how they can improve the characteristics of the sensors.

The presented results were published in [136]

5.2 Material and Methods

5.2.1 Design and Production Process

A three electrodes layout, including working, reference and counter electrodes, was selected as the most commonly used electrochemical sensor to guarantee optimal control of the potential of the cell. This kind of device relates the output current to the concentration of analytes that undergo redox reactions close to the active electrodes. Starting from previous work [66], [118], we designed simple cells with parallel rectangular electrodes. The sensor was fabricated by means of three different inks, deposed during three successive printing sessions. Silver-silver chloride ink (AgCl ink, XA-3773, Fujikura Kasei Co. Ltd., Shibakouen Minato-ku, Tokyo, Japan) was employed to fabricate conductive tracks, pads and the reference electrode (RE), to ensure high conductivity as well as RE stability; carbon ink (C ink,

EXP 2652-28, Creative Materials Inc., Ayer, MA, USA) was selected for WE and CE to provide a stable electrochemical substrate as well as a suitable substrate for the further functionalization; finally, two different kinds of nanostructures were selected for the surface functionalization: carbon nanotubes (CNT) or graphene. An explicative render design is shown in figure 5.1a. The CNT functionalization was otherwise performed using the commercial Nink 1000 (NANOLAB, Waltham, MA, USA) Multi-Walled Carbon Nanotubes ink. This is an aqueous suspension of multi-walled carbon nanotubes with a declared length between 1 μm and 5 μm and a diameter of 15 nm. The graphene coating was obtained exploiting a custom ink, developed to insure both printability and adhesion on the substrates. The ink was prepared by loading 15% of graphene powder and adding 3% of Polyvinylpyrrolidone (PVP) as binder and adhesive. To improve the printability and lower the ink viscosity, 38.5% of DI water and the same amount of Ethyl Glycol were added. Furthermore, to avoid the agglomeration of the solid particles, 5% dispersant was added. Different curing parameters were evaluated to provide an optimal curing process that requires a 20-minute thermal treatment at 200 °C. This ensures a good ink-substrate adhesion even in wet environments. The graphene powder was acquired by DIRECTA PLUS S.p.A. (Lomazzo, Italy) that produces it through a patented process. The obtained power has a mass-median-diameter (D50) of (4 $\pm$ 2) μm. An Aerosol Jet Printer (AJ300, Optomec, Albuquerque, NM, USA) with a 750 μm head was employed to fabricate the bare devices. This technique was selected as the production process because it allows deposing all the needed materials in a digitally controlled manner that ensures fast prototyping and production. A parallelized production protocol was implemented to reduce inter-sensor variability. In detail, for each lot, ten devices were printed in two rows within the same printing session. 30 bare electrodes were produced divided into three lots named A, B and C. Flexible polyimide foil of 75 μm (Kapton, DuPont de Nemours, Luxembourg, Grand Duchy of Luxembourg) were selected as substrate, due to its excellent mechanical properties as well as good compatibility with inks and printing process. For each lot, the substrate was at first cleaned in ethanol to remove possible contaminants and increase the adhesion between ink and substrate. After that, AgCl ink was deposed and cured at 125 °C for 30 minutes. Next, WE and CE were coated with carbon ink and then cured at 175 °C for 15 minutes. Finally, WE was AJP-functionalized using a 300 μm head and CNT (sensors 1-5) and graphene (sensors 6-10) inks. Those carbon-based nanostructures were chosen to improve the sensitivity of the sensors. According to the literature, such nanostructures are able to increase the surface-to-volume ratio even without changing the chemical composition of the surface [99], [137], [138]. Moreover, the selected digital production process aims to improve the repeatability of the printed sensors avoiding operator-dependent drop-casting functionalization methods [139], [140]. Both the

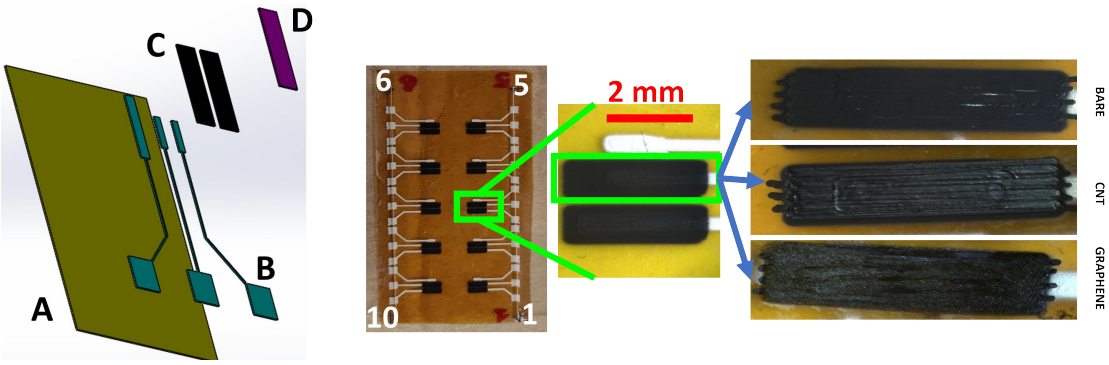

(a) (b)

Figure 5.1: Render design of the sensors (a) and the printed devices at different scales (b)

nanostructured inks were thermally cured for 20 minutes before testing. Lot A and B were used to perform preliminary adhesion and electrochemical tests, while lot C was used to evaluate sensor performance for peroxide detection. The final sensors fabricated are shown in figure 5.1b while the selected process parameters are reported in table 5.1.

Table 5.1: Process parameters employed during the fabrication of the devices

	AgCl Ink	C ink	CNT ink	Graphene Ink
Sheat flow (SCCM)	250	910	50	80
Atomizer flow (SCCM)	1100	1300	670	630
Exhaust flow (SCCM)	1040	1000	580	550
Printing speed (mm/s)	2.5	2.5	2	2
Plate temperature (°C)	75	75	45	90
Curing time (min)	30	15	20	20
Curing temperature (°C)	125	175	60	200
# of depositions	1	6	3	9
Head size (μm)	750	750	300	300

5.2.2 Preliminary Process Evaluation

After the production process, different tests were carried out to evaluate its goodness. At first, different geometrical evaluations were performed using an optical microscope NB50T (Orma Scientific, Sesto San Giovanni, Milan, Italy) with a trinocular zoom 0.8x–5x–LED. Then the geometrical profiles of the active electrodes were evaluated using an Alpha-Step IQ Surface Profilometer (KLA-Tencor,

Milpitas, CA, USA) in four different positions. At last, a set of scratch tests were carried on to assure the correct adhesion of the printed materials on the substrate. Briefly, a set of lines were scratched on the surface of the sacrificial electrodes using a metal blade. Then, a Kapton tape is placed in contact with the devices and removed three times. A visual examination was then carried on to assess the adhesion between the substrate and the selected inks.

5.2.3 Preliminary Electrochemical Assays

After the first physical assays, different tests were carried on analyzing the electrochemical behavior of the devices. All the following tests were performed using a portable potentiostat Palmsens3 EIS (Palmsens, Compact Electrochemical Interfaces, Houten, Utrecht, The Netherlands). At first, a set of cyclic voltammetry (CV) experiments were carried on in a phosphate-buffered saline (PBS) to evaluate the suitable potential windows of the sensors with the different functionalization. The test was performed running different CVs with a fixed scan rate (ν=0.2 V/s). From previous works [118], a starting [-0.05 ; 1] V potential window was selected and then it was gradually increased until unwanted features, such as peaks unrelated to the electroactive analytes in the solution (spurious peaks) were recorded. The suitable potential window selected is the last where no spurious peaks were recorded. Then a set of CVs was carried on in a ferro/ferricyanide ($[Fe(CN)_6]^{3-/4-}$) solution in PBS to evaluate the voltammograms and to further inquire the microscopic surface area of the electrodes according to [66]. Briefly, different CVs were carried on in ferro/ferricyanide solutions at different concentrations (2 mM, 4 mM, 6 mM and 8 mM) at a fixed scanrate (ν=0.2 V/s). The shape of the voltammograms was evaluated and the peak position and amplitude were compared between the different surface functionalization. To evaluate the surface area, the CVs on 8 mM ferro/ferricyanide in PBS solution were considered. From Randles-Sevcik equation 2.13 (reported here in 5.1), the electroactive surface area was calculated using the well-known electrochemical parameters of the ferrous/-ferric redox couple, as its diffusion coefficient ($D = 6.20 \cdot 10^{-6}\ cm^2/s$), number of active electrons ($n = 1$), as well as the physical constants (Faraday's constant F and the universal gas constant R) and the measured values for the peak current I_p and absolute temperature (T).

$$I_p = \pm 0.446 \cdot nFAC^* \sqrt{\frac{nFD\nu}{RT}} \tag{5.1}$$

Furthermore, the stability of the electrodes was assessed. One electrode for each functionalization was exposed to a ferro/ferricyanide solution (6 mM in PBS) and a set of 4 CVs (inside the previously defined potential windows, scanrate ν=0.2 V/s) were performed every 2 minutes for 9 times. The peak current was evaluated

in time and compared with the ones obtained with a commercial Screen-Printed Carbon Electrode (DRP-C11L, Metrohm Dropsens, Asturias, Spain). Moreover, a set of electrodes were immersed in PBS and single chronoamperometry (applied voltage 1V) was performed. The experiment aimed to estimate the time needed to obtain a steady-state current. This time is unique for each electrochemical system since it is influenced by several different factors depending on the electrolyte solution (species and its hydrodynamics), the analytes (number of transferred electrons and the species diffusion coefficient) and the electrodes (shape, dimensions, materials, resistance, surface roughness, porosity, etc. . .) [80]. Hence, this parameter has been estimated to plan further analysis accordingly

5.2.4 Peroxide Detection

To perform these experiments, the electrodes were immersed in 20 mL of PBS stirred at 490 rpm through an ARGO LAB M2-D Pro magnetic stirrer (Giorgio Bormac S.r.l., Carpi, Italy). This experimental setup is exemplified in figure 5.2. The electrodes underwent first a pre-treatment step that is composed of a 300 s long chronoamperometry at 1V followed by 20 CVs at 0.2 V/s scanrate and using the potential windows defined in the previous experiment (see Preliminary Electrochemical Evaluations). Then, hydrogen peroxide detection was performed through chronoamperometry (CA). After waiting for 600 s to reach the steady-state current, hydrogen peroxide was injected in steps of 100 μM until the total amount of 500 μM was achieved. Each concentration step was maintained for 200 s. The applied potential was set above the oxidation peak obtained from the voltammogram analysis at 1V for each kind of electrode. The collected signals were elaborated through a MATLAB 2019b. The current values were evaluated by averaging the last 20 s of each concentration step. From the collected data, the noise was extracted as already proposed in [141]. Briefly, noise is extracted by subtracting the average steady-state current of the sensors from the measured steady-state current. The former was considered the signal level of the sensors. Those two values were compared to evaluate the signal-to-noise ratio (SNR) of the electrodes. Moreover, the noise signal was evaluated in the frequency domain calculating its power spectral density (PSD).

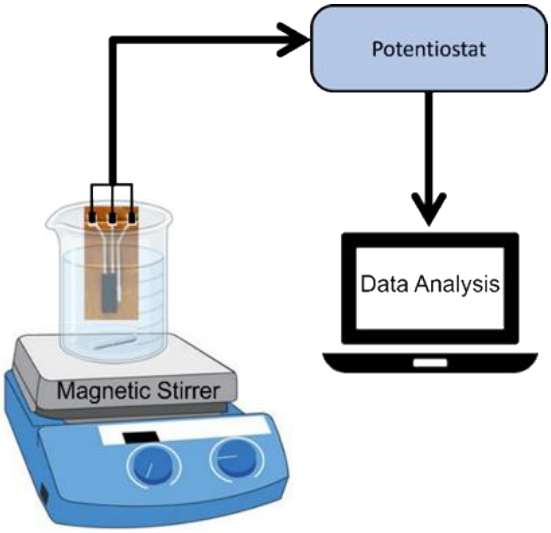

Figure 5.2: Experimental setup used to detect hydrogen peroxide. The sensor (orange) is placed inside a backer filled with PBS. This setup is placed on top of the stirrer. The Palmsens3 reads the information on the device and sends them on a laptop where the information is stored later analyzed

5.3 Experimental Results

5.3.1 Preliminary Process Evaluation

The preliminary evaluations on the electrodes using the optical microscope provided interesting information on the output of the production process. The correct coating of the WE and CE electrodes was assessed as well as the physical dimensions of the interconnecting lines that resulted (495 $\pm$ 30) μm wide including a reduced phenomenon of overspray. A set of images collected with the optical microscope can be seen in figure 5.1b where the three different WE used are shown. There, differences in color and texture are visible. In fact, the bare electrode resulted darker and opaque, the CNT-functionalized one is shinier and the graphene-functionalized presented a glitter-like appearance. Then, the mechanical profilometer was employed to assess the thickness of the produced electrodes in four different positions on all the lot C sensors. The profiles obtained in position p2 on a bare electrode can be seen in figure 5.3. The average profiles reflect the designed layer structure. The profiles taken in positions 2 and 3 that depict the center of the electrodes have similar shapes and they present an average thickness of 7.43 μm for CE. 11.33 μm for WE and 6.36 μm for RE. No appreciable difference between CNT and graphene functionalized electrodes is observed. In all the three kind of functionalization, the peaks measured on position p1 have

different thicknesses due to their different design. CE is the thickest due to the overlay of the silver/silver chloride and the carbon layers, WE only present the carbon layer, while the RE results invisible since no layer is present. Lastly, the scratch test was carried out on the sacrificial electrodes. No appreciable difference was observed after the test and thus the results (shown in figure 5.4) confirm the adhesion between each layer of the device and between the printed layers and the substrate.

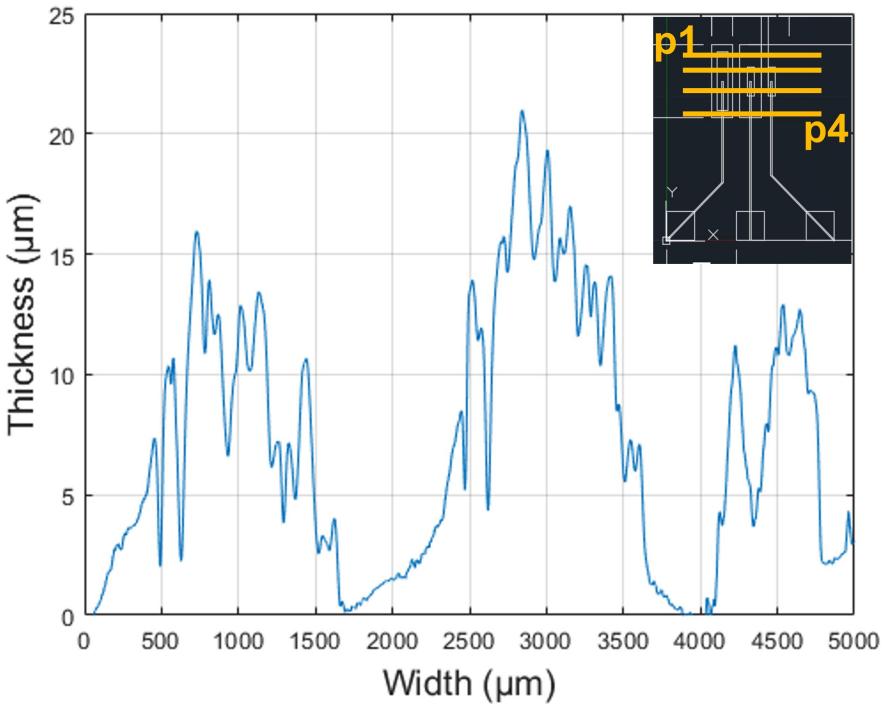

Figure 5.3: Profile of the electrodes (from left to right CE, WE and RE) achieved with the mechanical profilometer in position p2. In the inset, the four position in which the profiles were sampled are depicted.

5.3.2 Preliminary Electrochemical Assays

Results obtained from the first experiment performed allowed us to obtain the potential window for each kind of electrode we produced. The voltammograms obtained are shown in figure 5.5. All the electrodes present a spurious peak at around 0.1 V that appears to increase the lower bound of the window. According to this observation, for each kind of electrode, a potential window was selected to avoid those unwanted features. The potential windows, summarized in table 5.2, are adopted for all the following experiments.

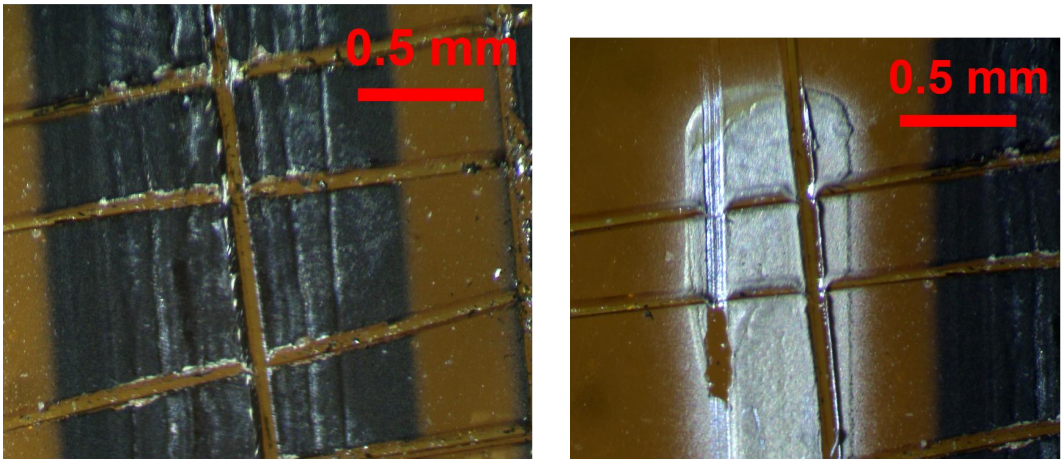

(a) (b)

Figure 5.4: Optical images of obtained on the sacrificial electrodes after the scratch test for a CE (a) and a RE (b)

Table 5.2: SELECTED POTENTIAL WINDOWS

Functional Ink	E_min (V)	E-max (V)
Bare Carbon	-0.05	1.3
CNT	-0.05	1.0
Graphene	-0.15	1.0

5.3.3 Cyclic Voltammetry

Cyclic voltammetry was carried on in ferro/ferricyanide solutions in various concentrations ranging from 2 to 8 mM. The obtained voltammograms are shown in figure 5.6. All the voltammograms present detectable oxidative peaks at well-defined potentials. CNT-functionalized electrodes show better performances presenting a fully reversible behavior, the lowest peak voltage at $(180 \pm 5)\ mV$ and the highest sensibility. Graphene presents an oxidative peak around $(455 \pm 20)\ mV$. The stable potential windows for those electrodes don't allow a complete formation of the reduction peak. Similar observations can be made for the voltammograms produced by the bare carbon electrodes where the peak voltage is located around $(974 \pm 17)\ mV$. The voltammograms were also used to obtain information about the active surface area of the electrodes. According to those calculations, graphene functionalized electrodes were able to improve the microscopic surface area 11.27 times more than the original bare electrodes, while CNT improved the microscopic area up to 105.56 folds.

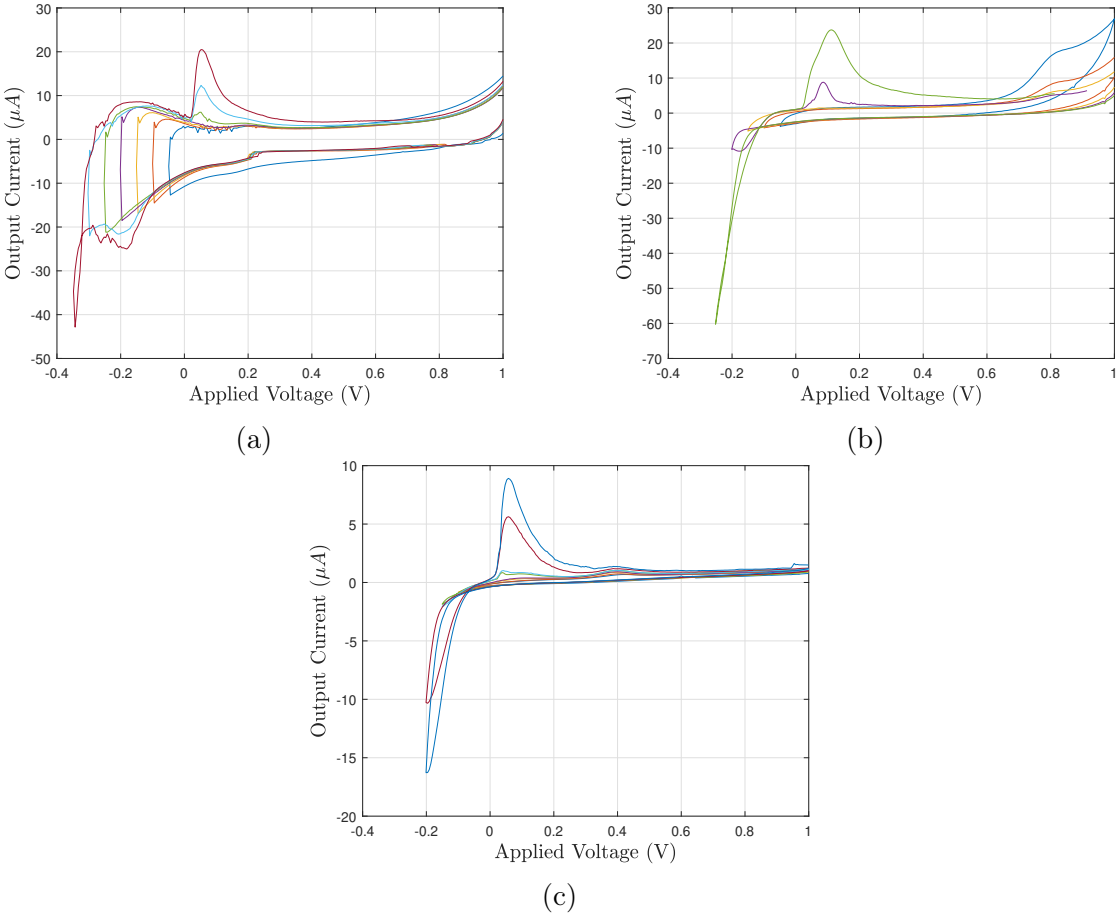

Figure 5.5: Potential windows definition test for bare carbon electrodes (a), CNT (b) and graphene (c) functionalized

5.3.4 Stability Tests

Electrode stability was assessed by evaluating the peak current over time (figure 5.7). All the examined electrodes present similar behavior, with an absolute value of the peak height increasing over time at each CV sweep. This trend is also present in commercial screen-printed electrodes (SPE). This data underlines how stability and consequently reusability might be the future challenge to be addressed to improve the overall behavior of these devices [65], [99] as far as cyclic voltammetry is selected as measurement technique. Then, the stability and settling time in chronoamperometric measurements was evaluated. Both the nano-functionalized electrodes produced a similar steady-state current. We considered the current at its steady-state when the signal derivative was lower than 0.01 μA/s. This situation occurs after approximately 400s for each kind of sensor.

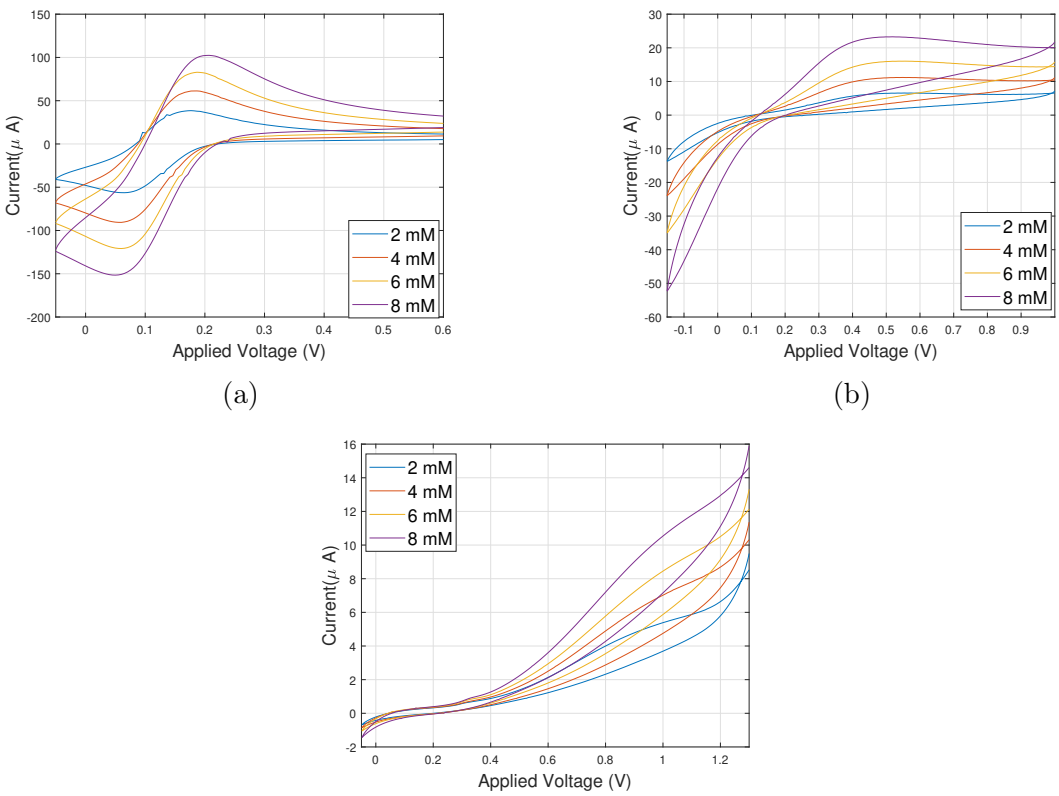

Figure 5.6: Voltammograms obtained with ferro/ferricyanide for CNT (a), graphene (b) and carbon bare (c) electrodes

5.3.5 Peroxide Detection

CA experiments were carried on for all the produced sensors in lot C. An example of the obtained output current is shown in figure 5.8a. All the calibration lines obtained from these experiments are reported in figure 5.8b. All the produced sensors produced a linear calibration line ($R^2 > 0.9$). The average sensitivity of CNT functionalized sensors resulted (20 ± 4) μA/mM with a relative standard deviation of 0.2, while graphene functionalized sensors produced an average sensitivity of (2.8 ± 0.9) μA/mM with a relative standard deviation of 0.33. Furthermore, the response time of the sensors was estimated stepping the pure PBS solution to a concentration of 100 μM. The response time was defined as the time needed to the output current signal to go from 10% to 90% of its steady-state. The behavior of all the printed sensors was evaluated and averaged. The two kinds of functionalization behave similarly and produce a fast response of (3 ± 1.5) s for CNT electrodes and of (2.5± 1.7) s for graphene ones. It is important to notice

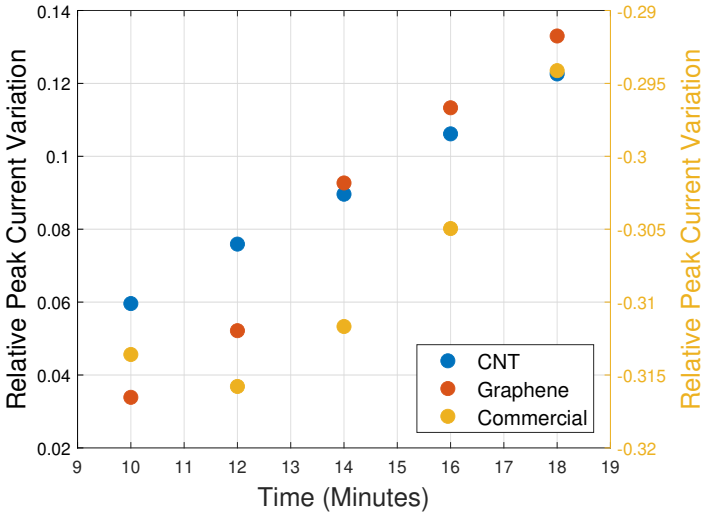

Figure 5.7: Normalized peak current of CVs (ν =0.2 V/s) recorded every 2 minutes in 6 mM ferro/ferricyanide solution for CNT functionalized electrodes (blue), graphene functionalized electrodes (red), and commercial SPE (yellow, secondary y axis).

that the main factor that impacts on the response time variability is the position in which the solution injected and thus is highly operator dependent. Even though the variability of the measurements is up to 70%, the response time of the device is comparable with other works in the literature [67], [142]. Moreover, different levels of noise were recorded on the signal from the different sensors. On average the signal-to-noise ratio for the sensors functionalized with CNT was 26.5 dB, while the one for the ones functionalized with graphene was almost double at 51.2 dB. A more accurate analysis of the noise produced by CNT sensors obtained as described in the Methods section was carried on and an example of its power spectral density (PSD) is shown in figure 5.9. All the sensors present a similar PSD with a constant spectrum at low frequency, with a flicker-like behavior above approximately 1 Hz. Different analyte concentrations slightly change the overall power of the noise shifting up the plot on the y-axis.

5.4 Discussion

Results obtained during sensors characterization offered the opportunity to discuss several interesting and promising aspects concerning both the electrochemical behavior of the specific materials employed (inks and nanomaterials) and the overall performances of the electrochemical sensors while quantifying hydrogen peroxide.

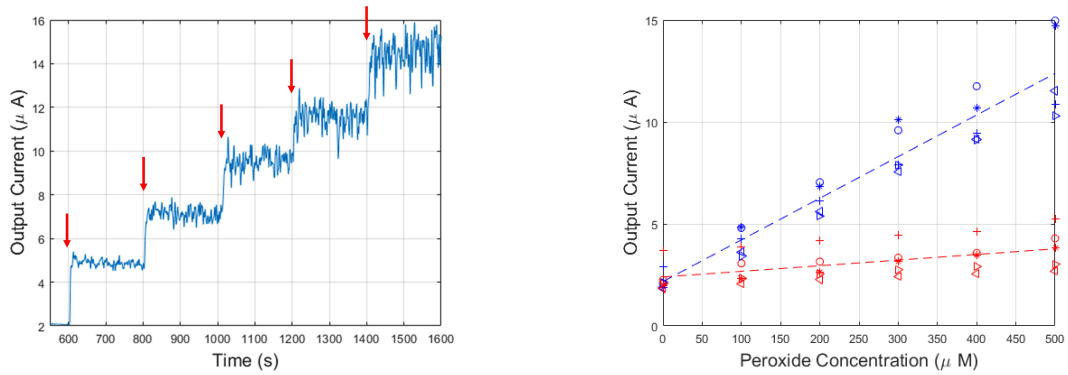

(a) (b)

Figure 5.8: Chronoamperometry responses for a graphene-functionalized sensor with injections of 100 μM of hydrogen peroxide at the time instants marked by red arrows (a). The calibration curves extracted for each sensor are reported in (b) where dashed lines represent the average fitting line for each electrode functionalized with CNT (blue) and graphene (red).

According to the results obtained during the preliminary electrochemical characterization, the spurious peak around 0.1 V observed in all the sensors represents an interesting effect to be discussed. This effect is probably due to the electroactivity of the silver/silver chloride layer underlying WE and CE in presence of the supporting electrolytic solution. In detail, due to the chemical properties of silver-silver chloride, when it is polarized at a negative potential, in presence of an ionic solution, it attracts electrons thus causing oxidation of the material. This results in the measurement of an oxidative peak of current originating by the interaction between the supporting electrolyte and the conductive electrode. Since this peak is completely independent of the concentration of the analyte in the solution, it represents a typical sign of instability and has to be avoided in the stability window, to make sure that all the peaks measured are only due to analyte presence. Similar effects are reported in the literature even when using silver/silver chlorides RE [82]. This issue might be reduced by modifying the production process and introducing a third layer composed of a different noble metal ink such as silver, gold or platinum that are stable in the potential window of interest. However, in the current application, the potential of interest required to detect hydrogen peroxide (1 V) falls within the potential windows ([-0.05 ; 1] V) in which the combination between solution and electrodes materials are stable and the system does not show any significant spurious current peaks. The absence of any peaks other than the one of ferro/ferricyanide in this window confirms that our results are reliable and robust. Moreover, it ensures the possibility to rely on the selected fabrication process which is faster and more cost-effective with respect to a traditional three-layer

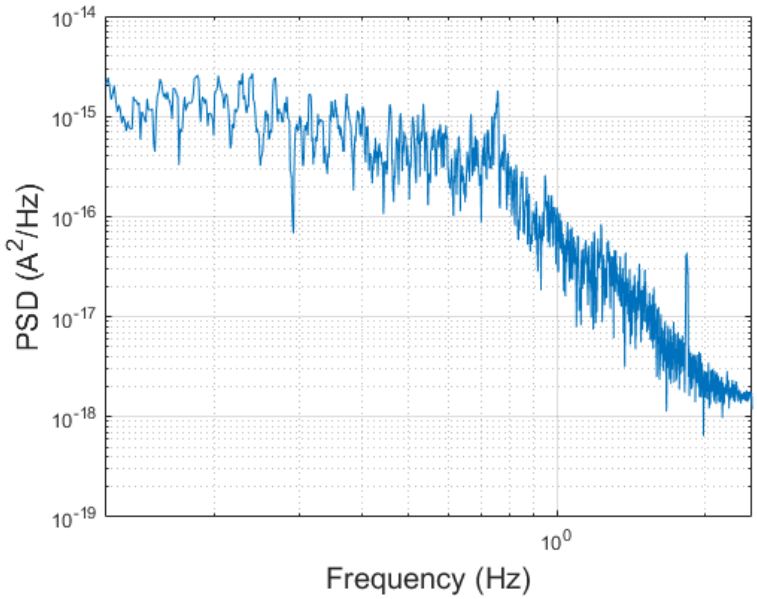

Figure 5.9: Power Spectral Density (PSD) of the noise produced by a CNT-functionalized sensor on a single concentration interval.

structure, with stacked silver, carbon and silver-chloride. Despite the presence of the spurious peak, thanks to the accurate definition of a stable window potential the CVs in ferro/ferricyanide revealed stable peaks voltages that are related to the surface functionalization, as well as the reference electrode material, the used electrolyte solution, ohmic drop and electrode resistance [82]. We report a decrease in the peak voltage for the CNT and graphene functionalization. Those effects are also reported in the literature and can be explained considering the different diffusion patterns involved and the change in the electrode-electrolyte interface resistance [132], [139], [143]. A major difference comparing presented results with the literature regards graphene-functionalized electrodes. For example in [144], small to no difference between bare and functionalized sensors as regards the peak position, while the ones presented here are highly reduced. The difference can be explained considering both the different production processes and the different materials employed. As an example, the cited work employs a glassy carbon electrode that is way more conductive than our printed ones and then graphene is electrodeposited on top of the electrode. This process introduces small to no differences in the electrode resistance. On the other hand, the hereby proposed devices, are composed of printed electrodes that present lower conductivity and then the use of a nanostructured functionalization widely reduces the electrode/electrolyte resistance. This produces a remarkable decrement in the standard potential of the reaction [80]. As regards the current produced by the sensors during peroxide

detection, different values were obtained according to their nano-functionalization. CNT helped increase the total output current up to 15 μA producing also better sensitivity, while graphene produced a maximum current of 5 μA in similar conditions. As already observed in [118], there is a linear correlation between the increased sensitivity of the devices and their surface area. Moreover, nanoparticles increased the surface area of the electrodes much more than the previously reported microstructures. Even though, those two approaches are valid and could be used together to further improve the sensitivity of electrochemical devices. The sensitivity of the sensor was improved increasing the surface-to-volume ratio of the electrode-solution interface thanks to the nanotubular geometry of CNTs, to the large sheets geometry of graphene layers randomly oriented during the deposition. Results obtained reveals that carbon nanotubes perform better than graphene in improving the sensitivity producing an average sensitivity of around $(27 \pm 5)\ \mu A/(mMcm^2)$ rather than $(3.5 \pm 1.3)\ \mu A/(mMcm^2)$ obtained with the latter. Those values are, on average, smaller than the ones obtained in the literature presented in table III, but that can be due to the on-site synthesis of those devices versus our ink deposition and/or the use of different nanostructures that further enhance the sensitivity of the reported devices. Similar observations can be made as regards the limit of detection (LOD) of the sensors. The intra-sensor LOD of our devices was determined according to [145] and reported as well in table 5.3. The LOD of the two kinds of functionalization presents small differences and is comparable with the ones already reported in the literature. The variations can be again due to different processes and interface resistance that can impact the overall signal to noise of the devices. The main differences in sensitivity and LOD between the sensors presented in this work and the best ones presented in the literature ([146], [147]) is due to different production processes, growth of the functionalization materials and different kind of nanostructures involved. For instance, in [146] a set of nanohybrids composed of carbon nanotubes and platinum nanoparticles were synthesized through a time-consuming approach that involves strong acids. Those nanoparticles were then dropcasted on a bulk platinum electrode. Otherwise in [147], direct growth of graphene nanostructures was achieved through an electrochemical process that required a highly controlled setup. Indeed, these techniques provide better metrological characteristics but with the approach proposed in this work is possible to highly reduce the use of dangerous chemicals and at the same time to reduce the time duration of the process production. Moreover, with the herby proposed approach, different patterns can be digitally designed and achieved allowing fast prototyping of innovative devices with characteristics that are a tradeoff between metrological and processing ones. As regards the noise recorded on the sensors, different features were observed. Analyzing the standard deviation of the signal at the different analyte concentrations, a linear

Table 5.3: Comparison of the values of the limit of detection (LOD, μM) and sensitivity ($\mu A/(mMcm^2)$) between different works in literature and our devices

	LOD	Sensitivity	Ref.
rGO-MWCNT	9.4	32.91	[149]
rGO	0.7	22.79	[142]
rGO	1.0	300.00	[147]
MWCNT-Pt	0.3	205.80	[146]
CNT	7.3	27.00	This work
Graphene	8.8	3.5	This work

correlation between the two parameters was recorded, which was more evident on CNT-functionalized sensors. Analyzing their PSD (figure 5.9), we could observe the superposition of two different effects. At low frequencies thermal and shot noise dominate. Both those effects produce a white noise with a power that is directly proportional to the average current flowing on the electrochemical cell and this explains the increase of noise at higher concentrations. At higher frequencies, mass transport effects are relevant. Those processes are involved in providing analytes to the surface of the electrodes where the reaction occurs and thus can shape the power spectral density of the correlated noise.[148]

5.5 Conclusions

In this chapter, a comprehensive comparison between the electrochemical performances of CNT and graphene-modified electrodes was reported. Significant differences were highlighted both in the preliminary characterization tests and in the detection of hydrogen peroxide. Even though similar limits of detections were achieved (7.3 μM for CNT and 8.8 μM for graphene) and both were able to improve the electrode-electrolyte interface area up to 105 times, CNT produced on average a better sensitivity (20 $\mu A \cdot mM^{-1}$) than graphene (2.8 $\mu A \cdot mM^{-1}$), while both the functionalization layer presented response times comparable with the literature, even though presenting a high variability. The introduction of an automatized processes or microfluidic system could be implemented in the future to try reducing the underlined variability. According to the presented results, both the nanostructured inks taken into consideration appear suitable to improve the sensitivity and in general the metrological characteristics of printed electrochemical sensors. Overall, the proposed fabrication process, which includes all the fabrication steps starting from bare electrodes to their surface functionalization, appears particularly convenient, in terms of time and cost-effectiveness, to ease the integration of fully printed electrochemical sensors in devices for envi-

ronmental control, diagnostic monitoring and to assess quality in the industrial environment. Further inquiries can be addressed to evaluate the effects of both micro and nanostructures on the metrological characteristics of electrochemical devices as well as to deepen the understanding of the noise and uncertainty produced by electrochemical transducers.

Chapter 6

Temperature Influence Evaluation and Correction

6.1 Evaluation of the Uncertainty Sources on Electrochemical Sensors

In a frame where electrochemical sensors acquired great relevance thanks to their ease of use and reduced cost that allow their employment in a wide set of applications (e.g. food safety, environmental pollution control, and the detection of biomolecules and proteins [61], [99], [121]–[123], [150], [151]), printed electronics and AJP in particular are reported in the literature as a viable technology to produce electrochemical sensors [54], [66], [118], [151]. Even though they present many advantages, those kinds of sensors are affected by many metrological issues, mostly regarding sensitivity, selectivity, repeatability, limit of detection (LOD) and signal to noise ratio (SNR) [99], [122]. Many efforts are devoted in the scientific community to address these issues. Among the solutions proposed in the literature, both organic (e.g. enzymes, antibodies, etc...) and inorganic functionalization are explored and seem to be providing relevant improvements. The latter class of functionalization includes nanomaterials that are promising both to increase the surface area of the electrodes and for their enzyme mimetic effect [128], [129]. These techniques are often used to address sensitivity and selectivity issues, but to further improve the quality of the measurements uncertainty control is fundamental. Uncertainty is related to the used instrumentation as well as the intrinsic noise produced by the sensor. The latter is important to allow the detection of low concentrations of analytes, design improved next-generation devices and develop better models for electrochemical sensors [141]. Excluding electromagnetic narrowband interferences, one of the main components that contributes to uncertainty in electronic systems and sensors is due to thermal effects. Moreover, temperature

effects are shown to influence the overall behavior of electrochemical sensors [152]. In light of this, the signal produced by AJP-printed electrochemical sensors during chronoamperometry (CA) experiments is analyzed to identify their different noise and uncertainty sources. The hereby presented results were published in [153].

6.1.1 Materials and Methods

6.1.1.1 Sensor Production Process

Starting from the work exposed in the previous chapters as well as in [66], [118], we designed simple three-electrode cells composed of working, reference and counter electrodes. We propose a three-layer device produced using silver-silver chloride ink chloride (AgCl ink, XA-3773, Fujikura Kasei Co. Ltd., Shibakouen Minato-ku, Tokyo, Japan) for interconnections, pads and the reference electrode (RE); A carbon layer (C ink, EXP 2652-28, Creative Materials Inc., Ayer, MA, USA) was deposed on top of the working and counter electrodes (WE and CE respectively) to provide a stable electrochemical substrate as well as a suitable substrate for the further functionalization performed with carbon nanotubes (Multi-Walled Carbon Nanotubes ink, Nink 1000, NANOLAB, Waltham, MA, USA). A Kapton substrate was selected as flexible substrate due to its excellent flexibility, thermal stability and chemical durability. The production process was performed optimized to try to reduce inter-sensor variability. The devices were printed in two rows parallelizing the production of the devices. An Aerosol Jet Printer (AJ300, Optomec, Albuquerque, NM, USA) with a 750 μm head was employed to fabricate the bare devices. The Kapton substrate for each lot is at first cleaned in ethanol to remove possible contaminants and increase the adhesion between ink and substrate. Then AgCl ink is deposed and cured at 125 °C for 30 minutes. Next, WE and CE are coated with carbon ink and then cured at 175 °C for 15 minutes. Then, the electrodes were AJP-functionalized using a 300 μm head and CNT ink. The nanostructured ink was thermally cured for 20 minutes before testing. The produced electrodes are shown in figure 6.1.

6.1.1.2 Preliminary Evaluations

Different tests were carried on analyzing the electrochemical behavior of the devices. All the tests were performed using a portable potentiostat Palmsens3 EIS (Palmsens, Compact Electrochemical Interfaces, Houten, Utrecht, The Netherlands). Those tests defined a stable potential window of [-0.15; 1]V in Phosphate Buffered Saline (PBS). Then, different chronoamperometry (CVs) were performed in ferro/ferricyanide ($[Fe(CN)_6]^{3-/4-}$) in PBS solutions at different concentrations (2 mM, 4 mM, 6 mM and 8 mM) at a fixed scan rate (ν=0.2 V/s). The shape

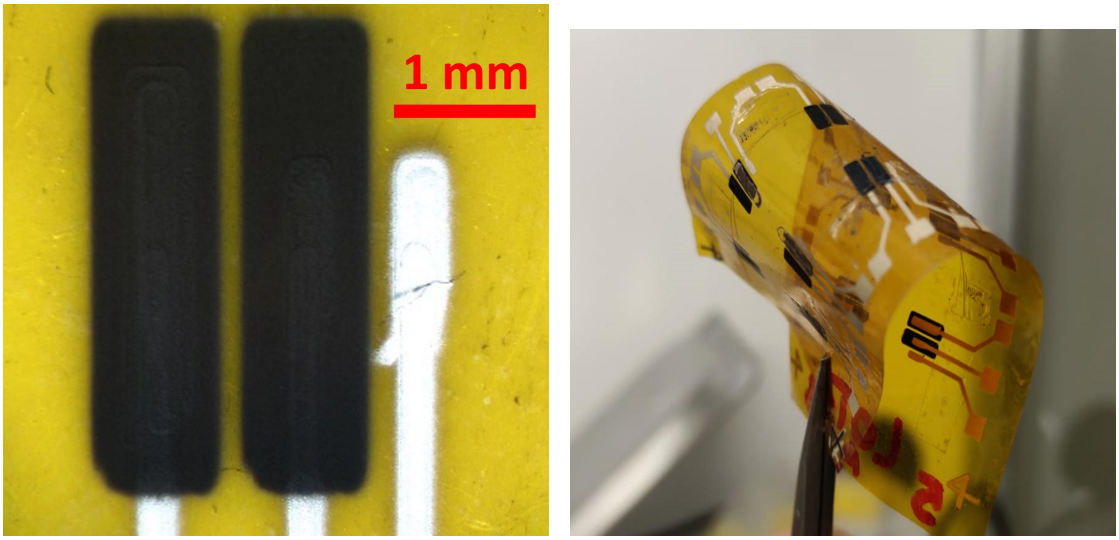

(a) (b)

Figure 6.1: Sensors produced with a focus on their active area (a) and their flexibility (b).

of the voltammograms was evaluated and the peak position and amplitude were compared.

6.1.1.3 Electrochemical Cell Impedance

The electrochemical cell impedance was also evaluated to obtain information on the equivalent model of the cell. In the literature, many are the proposed models like the one shown in the previous chapters, but often the most used is the Randles circuit shown in figure 6.2. C_{dl} represents the double-layer capacitance and R_s is the bulk solution resistance. R_{ct} (charge transfer resistance) and Z_W (Warburg impedance) represent the whole charge transfer process. [148] Those models are often referred as useful to understand the noise components of the sensors [154]. In order to obtain its impedance, the cell was polarized at 1V DC and 0.1V sinusoidal small signals at different frequencies were superimposed to obtain the impedance spectrum of the cell. The measurements were performed from 10 mHz to 50 kHz. The experiments were carried on changing two different parameters: at first the analyte concentration and then the stirring frequency. We chose ferro/ferricyanide as analyte and we changed different concentrations (0 mM, 1 mM, 2 mM and 3 mM).

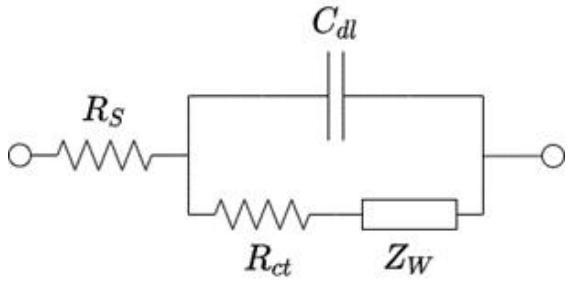

Figure 6.2: Randles circuit model for an electrode/electrolyte interface.

6.1.1.4 Measurement Setup for Noise Collection

To extract the noise levels, the electrodes were immersed in 20 mL of Phosphate Buffered Saline (PBS) solution that is stirred at different frequencies through an ARGO LAB M2-D Pro magnetic stirrer (Giorgio Bormac S.r.l., Carpi, Italy). Noise levels were evaluated at different hydrogen peroxide concentrations ranging from 100 μM to 500 μM through a single chronoamperometry (CA) where each 200 s the concentration is stepped. The applied potential was set above the oxidation peak for the analyte at 1 V. During this experiment the stirrer was set to 490 rpm. The experiment was carried on with the abovementioned Palmsens3 EIS at a sampling frequency of 5 Hz. The collected signals were elaborated through MATLAB 2019b. In particular, the output signal is expected to be a constant current. From this consideration, the average current is subtracted from the measured signal and the resulting one is considered as the output referred noise of our experiment. This is composed by both the noise introduced by the sensor and by the noise introduced by the interconnections, the electronic front-end and the digitalization. All the noise components that are related with the measurement setup were evaluated replacing the sensor with a 220 kΩ resistor. A resistor produces a white noise with a power spectral density (PSD) as reported in equation 6.1, where k represents the Boltzmann constant, R the gas constant and T the absolute temperature.

$$S_{ni} = \frac{4kT}{R} \tag{6.1}$$

The noise recorded in this condition produced a PSD constant over our frequencies of interest, with a mean power of approximately $2 \cdot 10^{-21} \frac{A^2}{Hz}$ and can be used as a background noise level.

6.1.1.5 Temperature Influence

A test was carried on assessing the thermal noise contribution on the signal. A sensor was immersed in 20 mL stirred PBS solution and a CA was recorded. After

300 s at 20 °C, the solution was heated up to 48 °C using the above mentioned stirrer. The solution temperature was monitored during the whole process. The recorded signal's noise was evaluated in the two situations. In a similar setup, a second electrode underwent a CA while the stirrer temperature was stepped from 25 °C to 50 °C to evaluate how the temperature influences the output current of the printed electrochemical sensors. To monitor the temperature a commercial Pt100 sensor was immersed in the solution. A custom virtual instrument on LabVIEW was designed to sample each second the resistance of the sensor through a Hewlett–Packard 34401a (HP, Palo Alto, CA, USA) using a 4-wire technique.

6.1.2 Results and Discussion

6.1.2.1 Preliminary Evaluations

The preliminary evaluations produce a set of well-defined voltammograms. An example can be seen in figure 6.3. The sensors presented a fully reversible behavior with a peak separation around 150 mV. The relationship between the peak current and the applied ferro/ferricyanide concentration presented an optimal linearity ($R^2 > 0.999$) showing a sensitivity of 12.94 μA/mM.

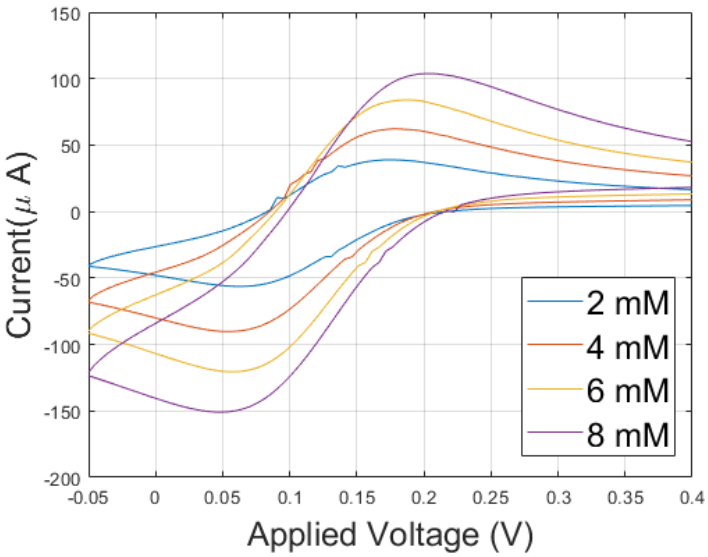

Figure 6.3: Voltammograms of the produced sensors performed with 0.2 V/s scan rate in a ferro/ferricyanide in PBS solution at concentration ranging from 2 mM (blue) to 8 mM (purple).

6.1.2.2 Electrochemical Cell Impedance

The evaluation of the sensor impedance provided different results. Great differences were observed in the impedance between measures in pure PBS and with ferro/ferricyanide (figure 6.4a). The main differences are due to the presence of faradic processes when the analyte is in the solution. Those processes mostly influence the charge transfer resistance and the Warburg impedance. Further measures were extracted at different ferro/ferricyanide concentrations (figure 6.4b). From these we could estimate thorough the impedance fitting tool embedded in PSTrace 5.8 a solution resistance of $R_S \approx 37\ \Omega$ and observe similar corner frequencies.

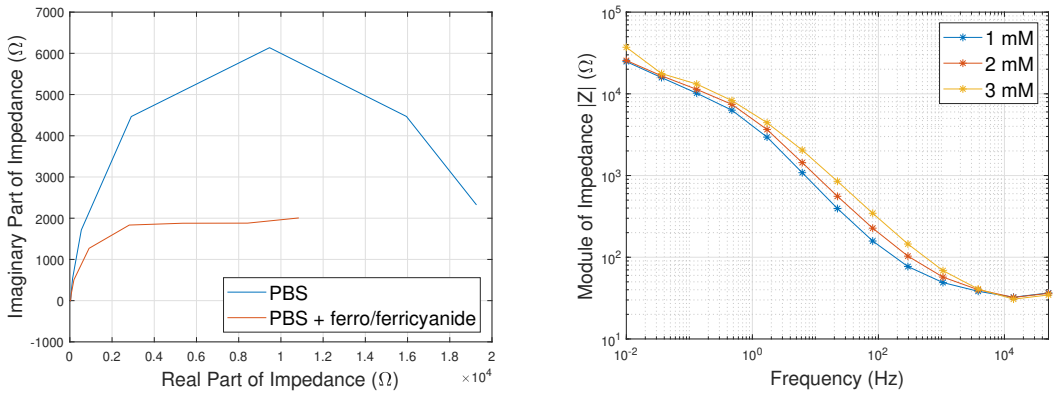

(a) (b)

Figure 6.4: Impedance of the electrodes. In (a) the real and imaginary part of the impedance are shown comparing the results obtained in PBS and with 1 mM ferro/ferricyanide. In (b) the impedance module at different ferro/ferricyanide concentration

6.1.2.3 Noise Analysis

Different levels of noise were recorded at a sampling frequency of 5 Hz on the signal at different concentrations of the analyte. We evaluated the standard deviation of the output current for each concentration step and a linear correlation ($R^2 > 0.997$) between those and the analyte concentration was obtained (figure 6.5). Moreover, accurate spectral analysis on the noise produced by the sensors was carried on and its power spectral density (PSD) is shown in figure 6.6. Relevant differences with the previously obtained background noise are observed. The PSD is not constant in frequency, but presents a corner around 0.9 Hz, while the plateau at low frequency is several orders of magnitude higher than background noise. According to [148], this peculiar shape can be seen a superposition of effects related to the transduction

principle of the sensors. At high frequencies, for example, mass transport effects are relevant. The current generation relies on the oxidation of species near the electrode surface and the reactants for those reactions are dispersed in the bulk solution and are moved to the electrode surface mainly by diffusion. This process requires time and thus shapes the Power Spectral Density (PSD) of the noise resembling a flicker noise. This section of the spectrum is empirically analyzed in [141] where equation 6.2 is fitted under different operating conditions.

$$N_{flicker} = S(f) = A \cdot \frac{I_{avg}^2}{f^\alpha} \tag{6.2}$$

The achieved measurements agree with the one reported in [141], showing how the α parameters tends to increase with the analyte concentration. On the other hand, at low frequency thermal and shot noise dominate. The former is related to energy dissipation both inside the electrolyte solution and on the electrode-electrolyte interface, while the latter is due to the presence of a potential barrier at the interface. Both those effects produce a white noise with a power that is directly proportional to the average current flowing on the electrochemical cell.

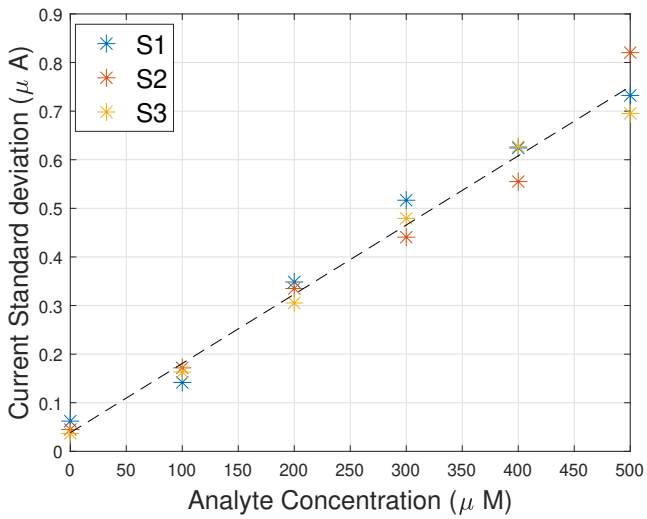

Figure 6.5: Standard deviation of the current output recorded at analyte concentrations ranging from 0 μM to 500 μM. Each color represents a sensor, while the dashed black line is the average best fitting line.

6.1.2.4 Temperature Influence

As exposed before, temperature is one of the main variables that influences the noise and thus the uncertainty in the produced sensors. At first, the noise compo-

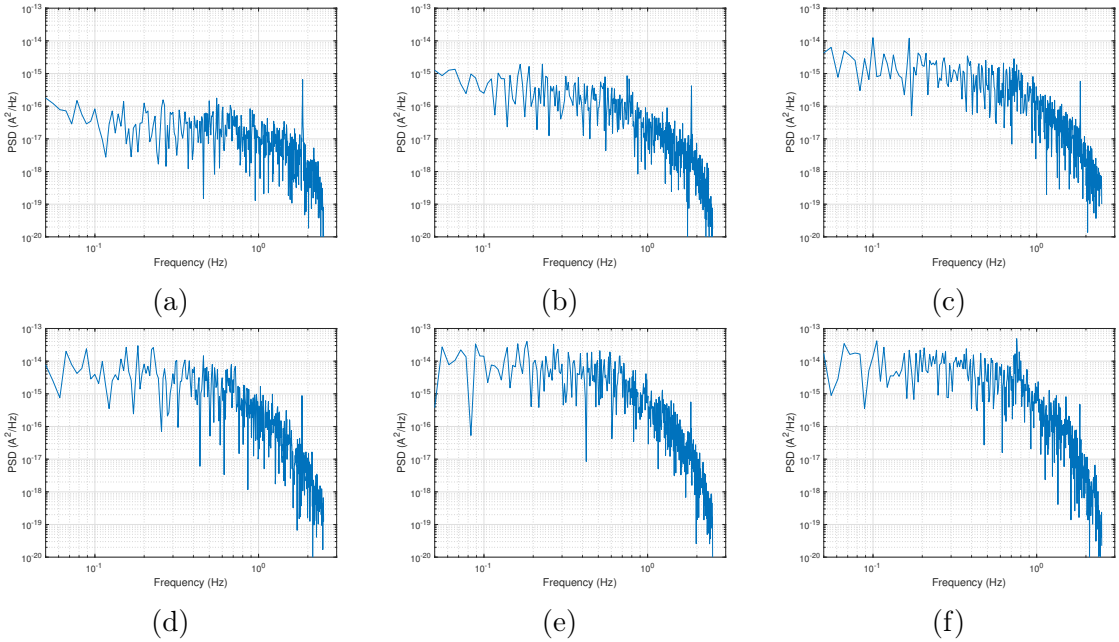

Figure 6.6: Power spectral density of the noise collected on chronoamperometry (CA) experiment at analyte concentrations 0 μM (a), 100 μM (b), 200 μM (c), 300 μM (d), 400 μM (e) and 500 μM (f).

nent was evaluated. Our measurements show (figure 6.7) how changing the solution temperature leads to an increasing level of noise on the signal. For instance, from 25 °C to 40 °C the noise level increases by 79%. During this experiment, a consistent variation of the average output current of the sensor was observed. This can be a main issue to address to provide reliable measures with these sensors. In order to characterize the process, a new experiment was performed and the output current was recorded while changing the solution temperature between 20 °C and 48 °C. The output current of the sensor was then related to solution temperature as shown in figure 6.8. This behavior can be explained from the Cottrell equation 6.3 which express the output current (i_o) as a function of the analyte concentration (C^*) and the surface area of the electrode (A).

$$i_o = \frac{nFAC^*\sqrt{D}}{\sqrt{\pi t}} \tag{6.3}$$

The diffusion coefficient D is temperature-dependent and can be expressed as Arrhenius exponential function [155] as in equation 6.4.

$$D = D_0 \exp\left(-\frac{E_D}{RT}\right) \tag{6.4}$$

From equations 6.3 and 6.4, the simplified model presented in equation 6.5 was extracted.

$$i_o = \sqrt{a \cdot \exp -\frac{b}{T}} \tag{6.5}$$

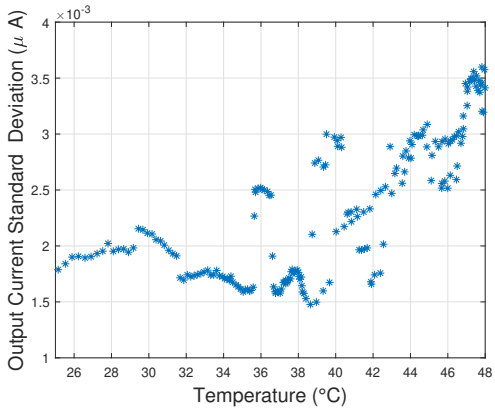

Figure 6.7: Standard deviation of the output current signal calculated for different temperatures.

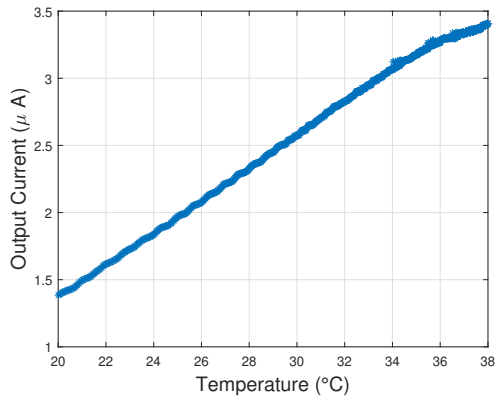

Figure 6.8: Output current of the sensor related to the temperature of the solution in which it is immersed.

6.1.3 Conclusions

In this section the uncertainty components and influence variables of a set of printed electrochemical sensors were considered. First assays show that electrochemical noise is directly proportional with analyte concentrations. The main components that shape the PSD of the sensor noise are explored and those are related to the electrochemical processes underlying the transduction principle of the device. At high frequency, the noise spectrum is limited by mass transport processes that introduce a flicker-like behavior, while at low frequency shot and thermal noise are mostly relevant. The effects of the temperature are then better investigated and they are shown to be dominant not only as a noise source but also as main influence parameters that can change the average output current of the sensor. This behavior was explained using the standard electrochemical theory from which a simplified fitting model was extracted and validated obtaining a coefficient of determination over 0.995. This last result is promising and can be used to compensate for the effects of temperature leading to an improvement of the reliability of the sensors in experiments that are performed out of laboratory conditions.

6.2 Correction of Temperature-related Uncertainty on Electrochemical E-skin Sensors

Starting from the considerations made in the previous section, it is possible to compensate the effects of temperature. To do so, a set of integrated temperature sensors should be designed accordingly.

Main aspects to be considered are obviously related to the target application, the target production process, as well as the measurement techniques that will be employed.

The target application being e-skins requires to reduce the dimensions of the design and to provide great flexibility to conform properly to the human body. Then considering Aerosol Jet Printing as the target printing process to easily integrate these temperature sensors in the previously described electrochemical ones, a few considerations on the kinds of sensors should be taken into account. Positive and Negative temperature coefficient thermistors (PTC and NTC respectively) as well as integrated temperature sensors are rigid and usually employ non-printable materials. Thermocouples require to know the temperature at the reference junction and therefore this is not feasible in many wearable applications. On the other hand, resistive temperature detectors (RTD) use the thermoresistive effect of metals allowing simple geometry designs and a production process compatible with printed electronics. [156] Thus, among the different typologies of temperature sensors, RTDs are the most suitable for a fully printed, compact and flexible design.

In order to try to comply to those requirements, two different fields were pursued: topology and material science. The former uses the design of the device shape to try to reduce the effects of substrate deformation. The latter on the other hand, focuses on different metallic materials to try to understand which is the better to produce the devices.

The first part of the presented results were published in [157], while the second part of the results are currently under revision for the IEEE Sensors Journal.

6.2.1 Topology analysis

In this section is proposed a preliminary study on flexible AJP-printed temperature sensors and their topology. The proposed printed sensors will be characterized analyzing their geometry and the effects of substrate deformation.

6.2.1.1 Sample Design and Production

The design process of the sensor started analyzing different possible geometries. Among the possible, the ones in figure 6.9 where selected. A standard strain

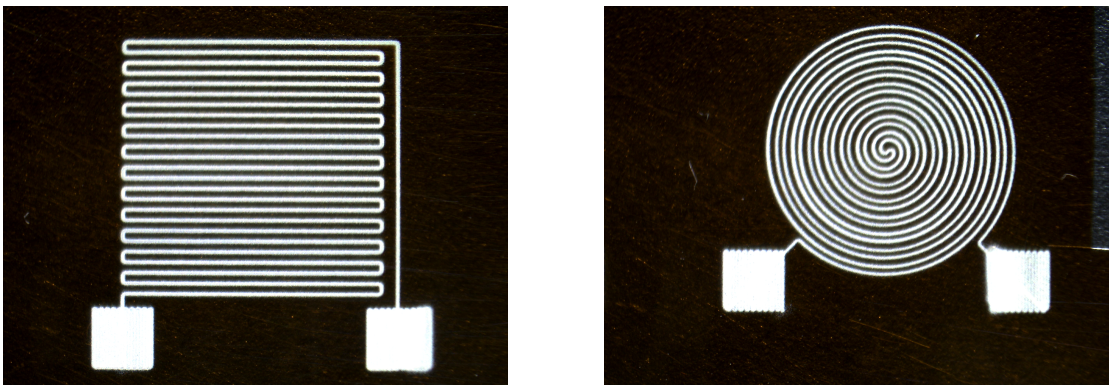

(a) (b)

Figure 6.9: Microscope images of the different geometries evaluated in this work. A standard strain gauge geometry (a) and the proposed double helix (b)

gauge-like geometry (figure 6.9a) was selected as state of art and designed following commercial strain gauges. On the other hand, a double helix geometry was further proposed to reduce the area of the sensor and uniform the dependance on strain in each direction. Both the geometries were designed with similar length and with target linewidth of 150 μm.

The devices were printed on a flexible polyimide foil (Kapton, DuPont de Nemours, Luxembourg, Grand Duchy of Luxembourg) using an Aerosol Jet Printer (AJ300, Optomec, Albuquerque, NM, USA). The substrate was selected considering the most common substrates used for eskins as well as the mechanical and electrical proprieties of the available materials [18]. Among the possible inks, a silver ink (Smart Aero, Genesink, Rousset, France) was selected and deposed after cleaning the substrate with ethanol to increase the ink-substrate adhesion. The selected process parameters were 1240 SCCM for the sheath flow, 850 SCCM for the atomizer flow and 800 SCCM for the exhaust flow with a process speed of 3 mm/s. The ink was thermally cured in an oven at 150 $°C$ for 60 minutes according to the producers' specifications to achieve proper electrical conductivity. After the process evaluation, the samples where then wired using a conductive epoxy (CW2400, Chemtronics, Kennesaw, USA). The overall production process is summarized in figure 6.10.

6.2.1.2 Process Evaluation

In order to evaluate the outcome of the production process two different evaluations were carried on. At first, the sensors were inspected using an optical microscope NB50T (Orma Scientific, Sesto San Giovanni, Milan, Italy) equipped with a trinocular zoom 0.8x–5x–LED and a camera. In this evaluation step the

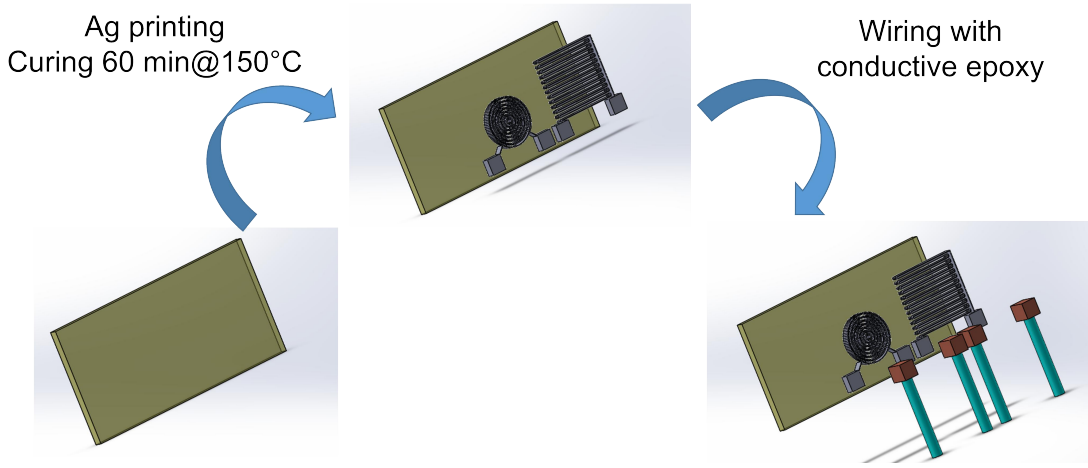

Figure 6.10: Render design of the three production process steps for the sensors

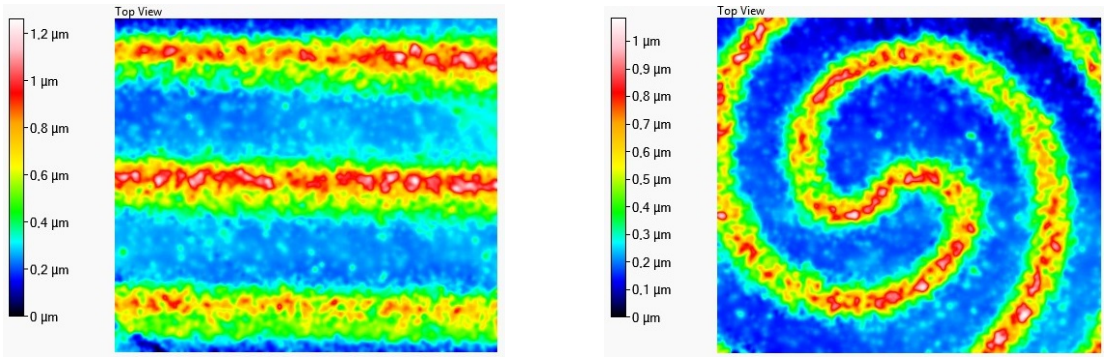

(a) (b)

Figure 6.11: Thickness of the printed lines obtained for the standard strain gauge geometry (a) and for the proposed double helix (b)

lines were analyzed and measured. The main aim was to measure the average line width and its variations in the production process. On the double helix geometry, the width was evaluated as (137 ± 19) μm, while it resulted (157 ± 16) μm for the strain gauge geometry. In the latter a smaller standard deviation was achieved due to the use of straight lines. In fact, straight lines are a simple trajectory that is easier to produce with linear stepper motors employed by the AJP.

Then a Filmetrics Profilm 3D optical profilometer (Filmetrics Inc., 10655 Roselle St., San Diego, CA, USA) was used to evaluate the thickness of the printed features. This analysis provided a set of clear images (figure 6.11) on the thickness of the printed traces revealing an uneven deposition of the functional material and an average thickness of 0.6 μm for the double helix and 0.4 μm for the classical strain gauge geometry.

6.2.1.3 Resistivity Evaluation

In order to calculate the average resistivity (ρ), a set of three straight, 2 cm-long lines were printed. The resistivity was then calculated using equation 6.6 where l is the length (known by design), R is the measured resistance and S is the average cross-section area of the conductor. This was evaluated through the optical profilometer, measuring the profile in three different positions for each sample.

$$\rho = R \cdot \frac{S}{l} \tag{6.6}$$

The resistance was evaluated using a digital bench-top multimeter Hewlett–Packard 34401a (HP, Palo Alto, CA, USA) and a 4-wire technique. According to the achieved results, the average line width for the straight lines used for the resistivity evaluation resulted (52.3 ± 4.5) μm. The average cross-section area was evaluated by integrating the data collected with the optical profilometer through a MATLAB program. An average of (150.3 ± 30.0) μm^2 was obtained. The measured line-resistance resulted on average (10.90 ± 4.85) Ω. The obtained average resistivity resulted (8.2 ± 4.0) Ω·cm that resulted compatible with the one presented in the ink datasheet.

6.2.1.4 Sensitivity to Substrate Bending

To evaluate the differences between the two geometries different features were evaluated. The behavior of the two geometries under deformation was evaluated. Briefly, the sensors were placed on a planar substrate, then they were bended onto a cylinder with radius 30 mm. The selected deformation axis was the one that maximized the sensibility of the devices. The variation in resistance is measured by a multimeter Hewlett–Packard 34401a with a 4-wire technique. One sample for each geometry was analyzed in bending.

The obtained resistance variation due to substrate deformation is shown (normalized) in figure 6.12. The two geometries presented a slightly different behavior when subjected to the same stimulus. The double helix geometry (in blue in the image) presented a fast-rising spike that settled then to a lover value and has equally fast rising and falling times. On the other hand, the strain gauge geometry (in red in the image) presented a slower rising and falling times similar to a first order system behavior. Both the geometries however presented a small variation of the resistance evaluated in the rest position.

6.2.1.5 Sensitivity to Temperature Variations

In order to evaluate the behavior of the sensors in relation with the temperature they were placed on top of an hotplate and covered with a beaker to avoid airflows.

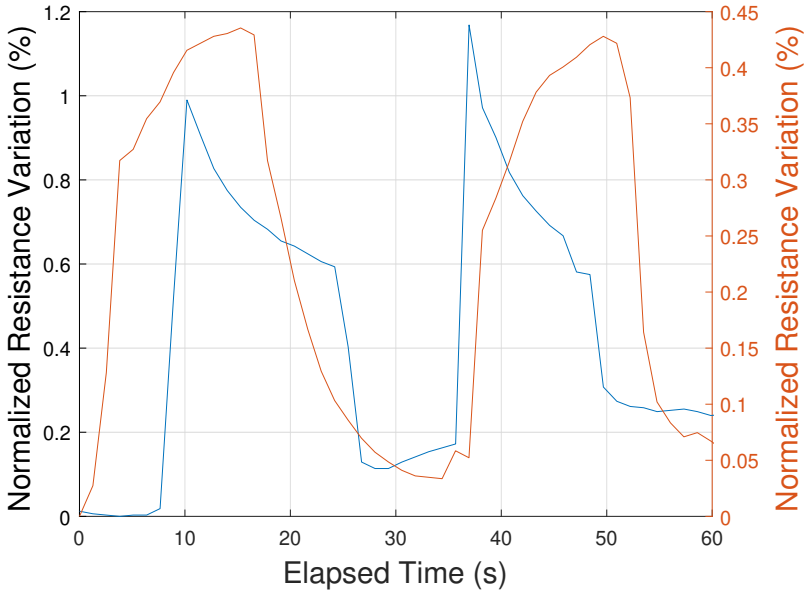

Figure 6.12: Stress-induced resistance variation in the sensors for double helix (blue) and strain gauge (red) geometries

A Pt100 was mounted nearby to provide a reliable measurement of the temperature applied to the sensors. All the measurements of resistance were performed using a 4-wire technique with a set of the aforementioned Hewlett–Packard 34401a multimeters connected with a computer through a GPIB interface and controlled by a LabVIEW interface that samples the signals at 1 Hz. A scheme of the experimental setup is shown in figure 6.13.

At first a set of increasing temperature setpoints ranging from room temperature up to 80 $°C$ were imposed each for 20 minutes. Then the hotplate was switched off and left to cool down back to room temperature. The collected data were then analyzed in MATLAB to obtain the temperature coefficient of resistance (TCR, α in the equation) and the resistance at 0 $°C$ (R_0) to be used in the simplified calibration relation shown in equation 6.7.

$$R = R_0 \cdot (1 + \alpha T) \tag{6.7}$$

The obtained results expressed as the relative variation of sensors' resistance to temperature are shown in figure 6.14. The printed devices present similar behavior perfectly comparable to the one of the Pt100 used as reference sensor. Moreover, the collected data were used to obtain a resistance-temperature characteristics for each sensor (figure 6.15). Both resulted linear, with reduced hysteresis. As regards the sensibility, the double helix geometry performed slightly better with a TCR of

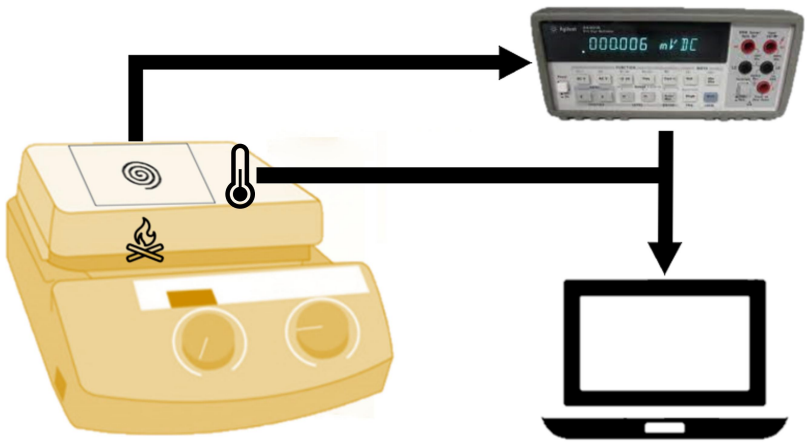

Figure 6.13: Schematic representation of the experimental setup for the evaluation of the sensitivity of temperature variations of the proposed sensors

$2.7 \pm 0.3 \cdot 10^{-3}$ $°C^{-1}$ than the strain gauge geometry (TCR=$2.3 \pm 0.1 \cdot 10^{-3}$ $°C^{-1}$).

6.2.1.6 Activity Closing Remarks

In the previous sections, two different geometries were preliminary analyzed in order to propose a fully AJP printed and flexible temperature sensor that can be used in the eskin application field. The sensors were designed and produced. Then the production process, the design idea and the materials were evaluated. The average resistivity of the conductive ink was evaluated to be 8.2 Ω·cm and compatible with the one presented in the material datasheet. Microscope analysis provided an average line width of 137 μm for the double helix geometry and 157 μm for the strain gauge one. A preliminary evaluation of the resistance variation under deformation was performed and revealed that the two geometries perform in different way, but the double helix presented lower variations. Considering on the other hand the effects of temperature, the two geometries performed similarly and resulted linear, with reduced hysteresis and similar sensibility. Even though, those results are promising, different future research topics are still open, such as exploring different materials and new geometries, as well as designing a whole system whose metrological characteristics can meet application requirements, such as a temperature resolution of 0.1 $°C$.

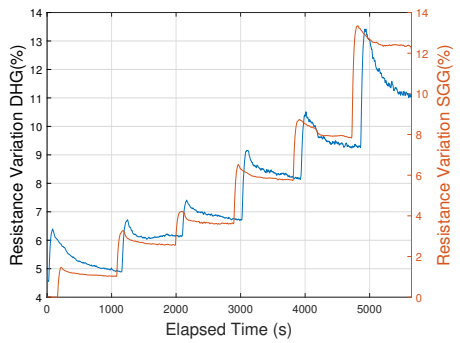

Figure 6.14: Temperature dependance of the sensors shown in time. The resistance variation for the double helix geometry is reported in blue, while the one of the strain gauge geometry is reported in red

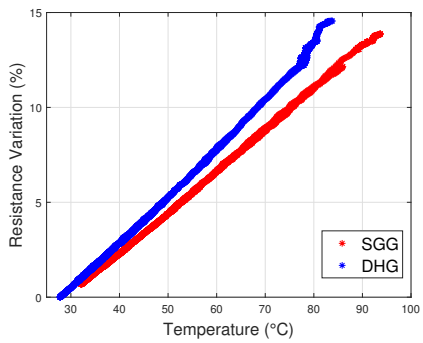

Figure 6.15: Resistance-Temperature plot for the strain gauge geometry (in red) and the double helix geometry (in blue)

6.2.2 Material Evaluation

Resistive temperature sensors (RTD) are based on the thermoresistive effect according to which the resistance of a material changes with temperature due to both a change in the resistivity of the bulk material and geometrical modifications. Among them, however, the latter is in metals results to be negligible [158]. Among the possible different techniques that have been proposed in the literature for the fabrication of RTDs, printed and additive manufacturing techniques such as earosol jet printing (AJP) are reported. Those allow a quick prototyping process, can be adapted to work even on non-planar/3D surfaces and offers a wide set of different materials. All these capabilities are promising for the development of smart objects [57], [159]. It's important to notice that all the printed inks are usually composed of nanoparticles suspended in a set of solvents. In order to ensure proper electrical conductivity, it's thus important to propose a proper curing process that eliminates all the spurious matter and connects the nanoparticles. In this frame, the ink producers usually provide a set of information to achieve certain resistivity values. On the other hand, however, no data is usually provided as regards the temperature coefficient of resistance (TCR) of the material. From these considerations the aim of this work is to try to compare different curing temperatures within the curing range proposed by the producers, trying to correlate the microscopic characteristics of the cured ink to the macroscopic ones (e.g. room temperature resistance and TCR) of the final device.

6.2.2.1 Sensor Design

The proposed study tries to evaluate the differences produced on materials commonly used in printed electronics related to the behavior in temperature and their sintering conditions. To avoid observing unwanted effects such as resistance variation due to bending and stretching, a rigid material was selected as the substrate. In this frame, the selected material was alumina thanks to its mechanical characteristics of stiffness and great ability to withstand high temperatures. As regards the selected functional materials, two well-known and widely used inks were selected. The first one is a silver nanoparticle-based one (SmartAero, Genesink, Rousset, France), while the second is based on gold nanoparticles (UTDAuTE, UTDOTS, Champaign, IL, USA). The sensors were then designed as in figure 6.16 in order to maximize the length/area ratio as well as to provide easily accessible pads for wiring. This first design was used for preliminary printing tests in order to provide optimal printing parameters for the two inks. Those parameters were required to be different due to the different composition and viscosity of the two inks. The main difference is the atomization process: the silver ink was atomized using the pneumatic atomizer, while the gold ink used the ultrasonic one. The preliminary tests showed that to achieve good conductivity with the gold ink more than one deposition is required. Thus, to achieve similar printing times and resistances in the same order of magnitude, the gold sample design was shortened. Then for both kinds of ink, a 6-sensor sample on a single 5x5 in alumina was prepared and then used in the production process that used the process parameters shown in table 6.1.

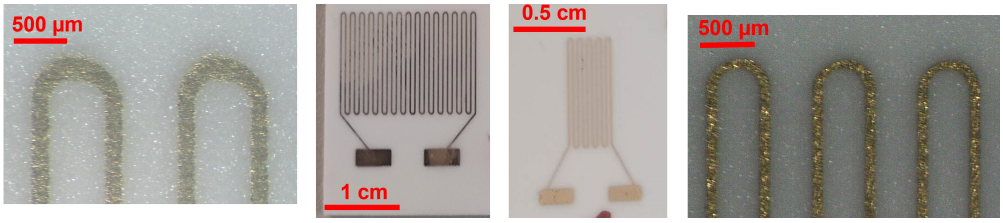

Figure 6.16: An example of the produced silver (left) and gold (right) electrodes.

6.2.2.2 Device Producion Process

Even though the two inks required different process parameters, the production process is unchanged. At first, the substrates were carefully cleaned with ethanol to remove dust particles, grease and any kind of dirt. Then all the samples were printed in series to reduce the printing variability. For each ink 5 samples were produced (30 sensors for each ink in total). In order to evaluate the differences

Table 6.1: process parameters selected for the printing of the two inks

	Ag ink	Au ink
SH (SCCM)	1240	90
ATM (SCCM)	820	23
EX (SCCM)	800	–
UA current (mA)	–	635
Plate temperature (°C)	60	70
Printing speed (mm/s)	5	5
Deposition #	1	2

Table 6.2: curing temperature for each of the produced sample for both silver and gold.

	S1	S2	S3	S4	S5
Silver	100 °C	120 °C	150 °C	200 °C	250 °C
Gold	275 °C	300 °C	325 °C	350 °C	375 °C

in the samples due to the curing temperature, each one was cured at a different temperature within the curing range proposed by the ink manufacturers for 60 minutes. The selected curing temperatures are reported in table 6.2.

All the samples underwent an accurate microscopical analysis that allowed the evaluation of the printed line width using an optical microscope (NB50T, Orma Scientific, Sesto San Giovanni, Milan, Italy). The silver ink produced on average a line width of (116 ± 9) μm while the gold ink produced a thinner line on average of (77 ± 7) μm. Those differences are related to the different processes employed in the production step and the peculiar characteristics of the inks.

After the curing process, all the sensors on each sample were measured at room temperature to assess the goodness of the printing and curing processes and the obtained process variability. The measurements were acquired by a Hewlett–Packard 34401a (HP, Palo Alto, CA, USA) digital multimeter in a 4-wire configuration. The room temperature resistance was evaluated on all the samples for both functional inks. The obtained resistive values are shown in figure 6.17. In general, the overall resistance decreases when the curing temperature increases hinting at an improved conductivity. Moreover, the overall variability within the samples tends to decrease and was evaluated by calculating the coefficient of variation within the sensors of each sample. According to the collected data, the overall variability was halved in the silver ink (from 6.83% down to 3.09%) while it was reduced from 17.76% down to 0.89% in the gold ones. However, in the latter situation, a slight increase in the coefficient of variation was observed at the last curing temperature. This effect may be due to excessive thermal stress induced on the printed tracks that

leads to random cracking and thus to higher variability [55].

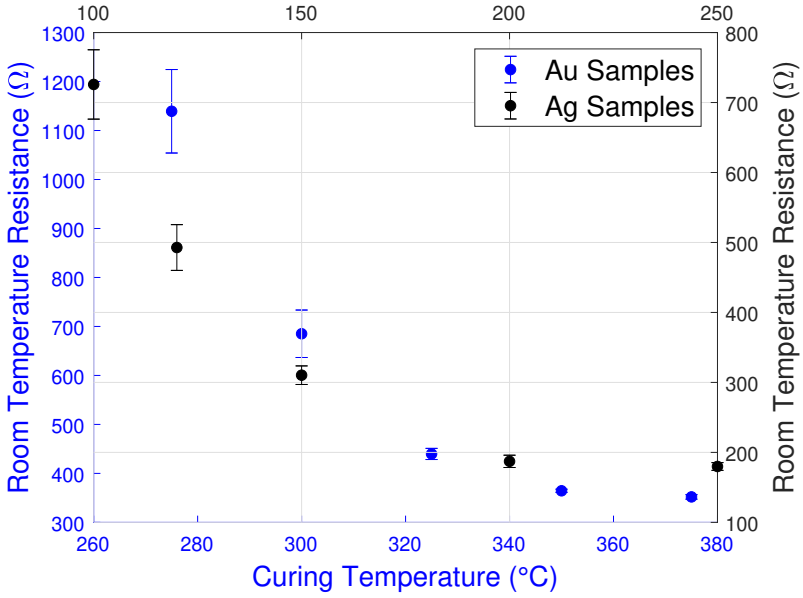

Figure 6.17: Room temperature resistance variation on the samples produced both by silver and gold ink.

After those preliminary tests, the sensors were connected to a set of cables in a 4-wires configuration that was fixed using a two-part, silver-based conductive epoxy (CW2400, Chemtronics, Kennesaw, USA). After its applications, the epoxy was oven cured at 80 °C for 60 minutes.

6.2.2.3 SEM Imaging

Morphological investigations were carried out using a field-emission scanning electron microscope (FE-SEM) MIRA-3 (TESCAN, Brno, Czech Republic) at an accelerating voltage of 5-7 kV in order to assess the differences produced by the different curing processes and selected ink. The samples were analyzed at different magnification values to evaluate the different features in the microscopic disposition of the nanoparticles as well as their agglomeration due to the curing process. Then the images were elaborated using the ImageJ software in order to evaluate the particle/pores size. Briefly, after providing the required scale to each image, the images were modified inside the program to increase the visibility of the particles. Then, the area of the particles was extracted and statistically analyzed.

The acquired SEM images produced interesting figures that allowed understanding of the different degrees of sinterization of the inks related to the applied

curing temperatures. The silver ink shows clear differences in the nanoparticle agglomeration pattern (figure 6.18). Below 120 °C the nanoparticles do not present great differences and appear to be almost unchanged. Increasing the curing temperature up to 150 °C, the nanoparticles start to agglomerate and fuse one another creating bigger clusters. Increasing again the curing temperature, the particles start to appear more and more uniform and agglomerate, presenting however a set of holes. As regards the microscopic evaluations performed on gold ink (figure 6.19), the behavior seems similar to the one already described for the previous ink. In particular, at the first tested curing temperature (275 °C) the nanoparticles are clearly visible, while they cluster in bigger groups increasing the curing temperature. The cluster size seems to reach a plateau after 325 °C. Those visual evaluations were confirmed and quantified through the ImageJ software that allowed the estimation of the particle sizes. The achieved results for silver and gold samples are shown in figure 6.18f and 6.19f respectively.

6.2.2.4 Temperature Sensitivity Evaluation

In order to evaluate the behavior of the sensors at different temperatures the sensors were placed inside a climatic chamber UC 150/70 (Advanced Material Testing S.R.L., Limbiate, Italy) programmed to change the temperature in steps in the range between -10 °C and +70 °C. All the sensors were measured by a set of Hewlett–Packard 34401a (HP, Palo Alto, CA, USA) digital multimeters in a 4-wire configuration controlled by a LabVIEW virtual instrument that sampled their value at 1 Hz. Moreover, a Pt100 standard sample was also placed close to the samples in order to provide a known and fixed temperature reference for the measurements. The collected data were then elaborated through MATLAB. A simple code that identifies all the setpoint temperatures was prepared and used to obtain statistical information on the resistance variation as well as to calculate the temperature coefficient of resistance (TCR) in all the situations. Briefly, the simplified characteristic equation 6.8 for RTD sensors, where R_0 is the resistance of the sensors at the temperature T_0, R is the resistance of the sensors at temperature T and α the TCR of the sensors is expanded to match the explicit equation of a line. Assuming $T_0 = 0$ and then $T - T_0 = \Delta T$ as the independent variable, the collected data points were fitted to a line and the two obtained parameters (m as slope and q as intercept) were matched to the ones obtained in equation 6.8 obtaining the system 6.9.

$$R = R_0 \cdot [1 + \alpha(T - T_0)] = R_0 \cdot [1 + \alpha\Delta T] = \alpha\Delta T R_0 + R_0 \tag{6.8}$$

$$\begin{cases} m = \alpha R_0 \\ q = R_0 \end{cases} \tag{6.9}$$

The obtained TCRs were then compared and evaluated to determine differences in behavior due to the curing process and selected material. The sensitivity to temperature was evaluated on five sensors for each sample in the above-mentioned climatic chamber. The results of those experiments are proposed in figure 6.20. It's possible to notice how the silver ink presents a linear correlation ($R^2 = 0.991$) between the achieved sensitivity and the curing temperature. On the other hand, the gold ink presents a TCR that initially rises with the curing temperature but then reaches a plateau when cured at 325 °C or above. Another interesting consideration is that the silver ink presents TCR values that tend to the one of the bulk material reported in the literature ($\approx 3.8 \cdot 10^{-3}\ °C^{-1}$) while the gold ink presents a maximum TCR value of around $2.5 \cdot 10^{-3}\ °C^{-1}$, lower than the value of bulk ($\approx 3.7 \cdot 10^{-3}\ °C^{-1}$).

6.2.2.5 Activity Closing Remarks

In this work, the microscopic and macroscopic behavior of different inks is evaluated at different curing temperatures as regards the room temperature resistance and the temperature coefficient of resistance (TCR). The sensors were designed as simple serpentines and then preliminary evaluated to assess the achieved linewidth and the room temperature resistance. The overall linewidth presented small variations both using the silver (CV_{Ag}=7,7%) and the gold (CV_{Au}=9,1%) inks considering all the produced sensors. The room temperature resistance on the other hand, presents a sensible reduction (71,2% for the gold samples and 75,2% for the silver ones) with increasing curing temperatures. Moreover, it's possible to observe a strong decrease in the coefficient of variation up to 95% which indicates how curing the inks at higher temperatures tends to uniform the variability of the produced sensors. Moreover, on the macroscopic scale, the behavior in temperature of the sensors was evaluated by means of a climatic chamber in the $[-10; 70]$ °C temperature range. This evaluation produced for the silver sample an increasing sensitivity with increasing curing temperatures with TCRs. On the other hand, the TCR of the gold samples reached a plateau at around $2.5 \cdot 10^{-3}\ °C^{-1}$ for all the samples cured at temperatures above 325 °C. The SEM images allowed the understanding of the different nanoparticles clustering achieved with the proposed curing temperatures. The silver ink tends to increase almost linearly the particle size up to 61.5% until it reaches a bulk-like configuration that however presents a set of cavities. Gold nanoparticles on the other hand present a plateau in the cluster size after an increase of 71.0% the size. Those microscopic characteristics

seem to reflect the macroscopic behavior of the sensitivity of the overall sensors in temperature. As suggested in [160] for the overall resistivity, this result is related to the different cluster sizes and to the number of boundaries between the different grains. In conclusion, the behavior of two materials was analyzed both from the microscopic and macroscopic points of view. The achieved results underline the need to study the effects of the curing process for any material used in additive manufacturing as a powerful process parameter to be taken into account when designing sensors or systems.

6.3 Conclusions

In this chapter, a different issue present on electrochemical sensors in e-skin application is inquired: its uncertainty sources. At first the different components and influence variables on a set of printed electrochemical sensors were considered and explored trying to understand which are the most influential in shaping the noise spectrum and how they can be correlated to the transduction principle of the device. After those first inquires, the issue of temperature influence arose and thys was deepened with a set of experiments. Those showed that with raising temperatures both the standard deviation of the measurements and the overall average output current of the sensors.

Those collected evidences introduce a serious issue that can reduce the applicability of electrochemical sensors in out of lab conditions. Thus, to address this, the effects of temperature should be compensated with the data collected through a set of sensors. Hence, the next part of the chapter was focused on two different studies that explored different aspects of the design of fully printed temperature sensors that are suitable for the target application. At first a study on two different geometries was carried on to try to reduce the effects of substrate deformation and the occupied area. This work revealed how it's possible to achieve a good variation of the resistance in temperature (up to 12%) with almost-negligible differences (≈1%) due to substrates deformation. Lastly, the materials and curing processes were evaluated taking into account both their microscopic and macroscopic characteristics achieving interesting information that can be used to improve the design of temperature sensors taking into account also the production and the curing process.

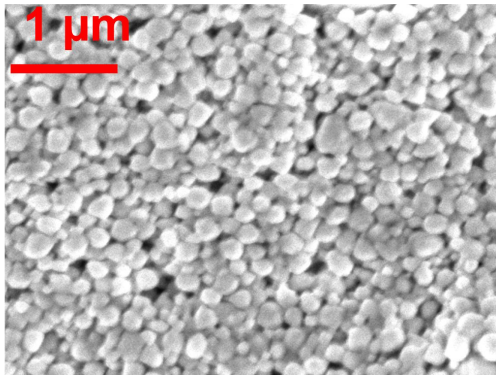

(a)

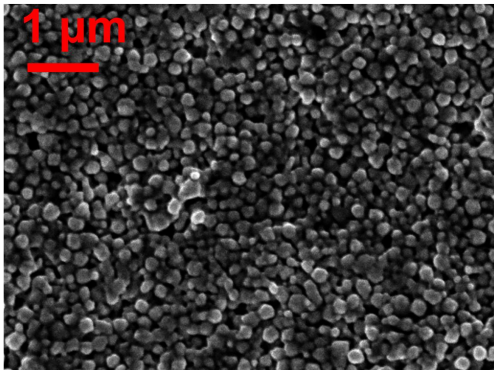

(b)

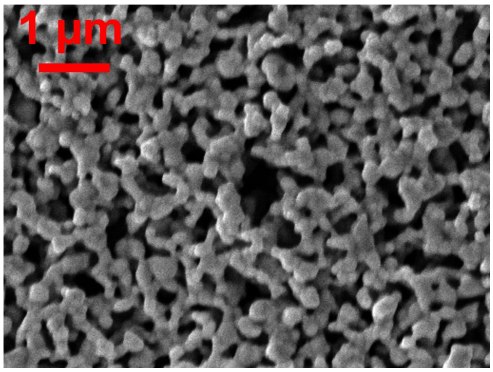

(c)

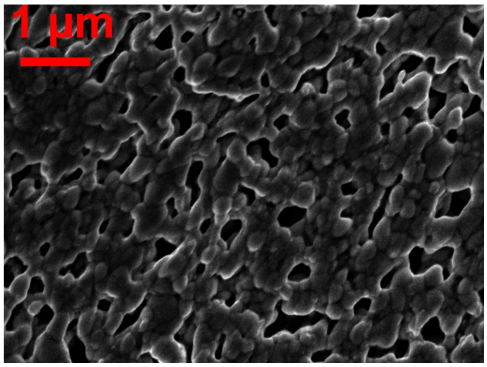

(d)

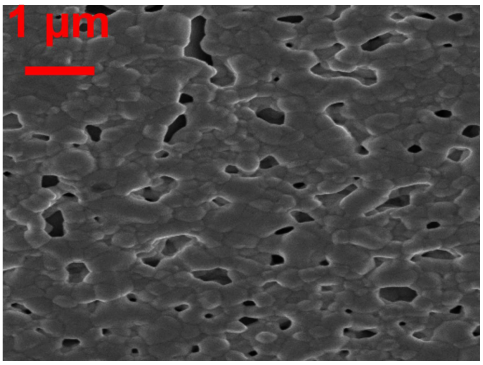

(e)

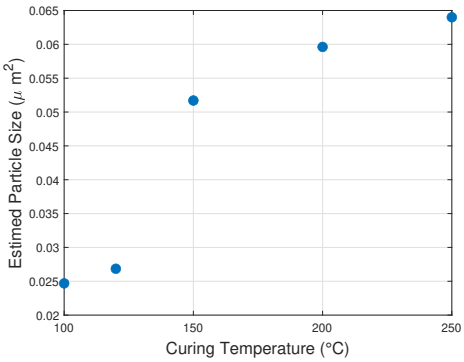

(f)

Figure 6.18: Results of the SEM evaluation performed on the silver samples cured at 100 °C (a), 120 °C (b), 150 °C (c), 200 °C (d) and 250 °C (e). In f, the estimated cluster size is plotted with respect to the curing temperature.

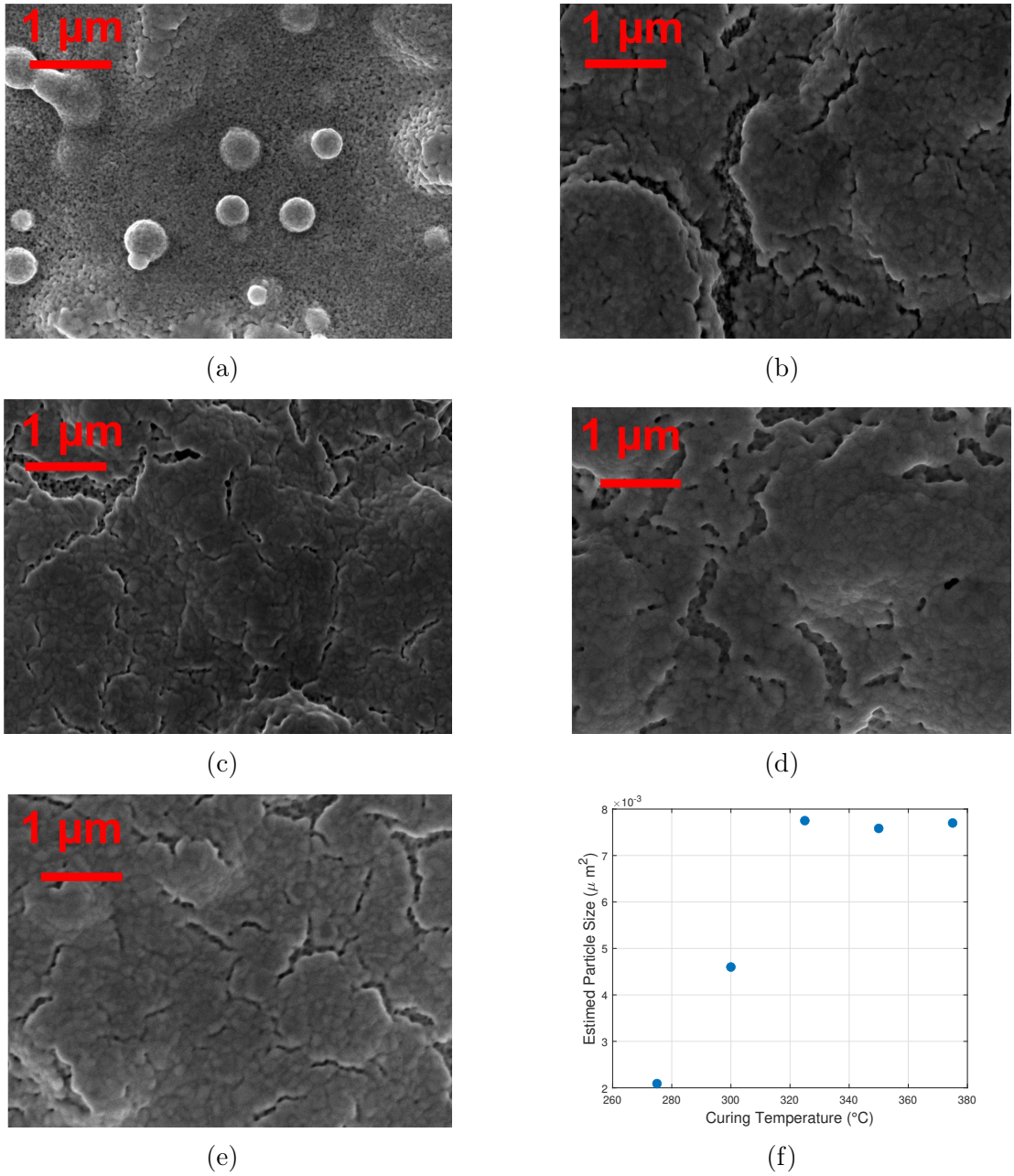

Figure 6.19: Results of the SEM evaluation performed on the gold samples cured at 275 °C (a), 300 °C (b), 325 °C (c), 350 °C (d) and 375 °C (e). In f, the estimated cluster size is plotted with respect to the curing temperature.

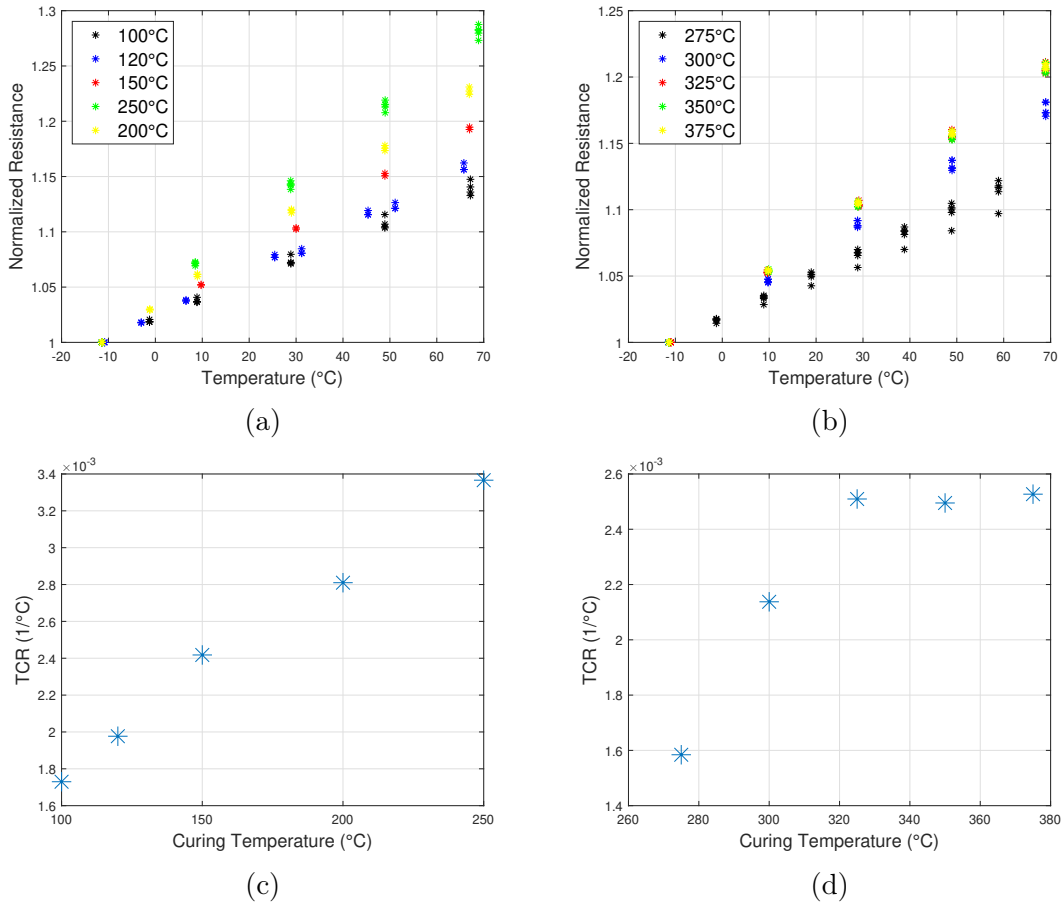

Figure 6.20: Calibration relationship achieved with silver (a) and gold (b) ink at different curing temperatures. The different TCRs obtained after the different curing temperatures were reported for silver (c) and for gold (d) ink.

Chapter 7

General Conclusions and Future Outlooks

This thesis is focused on the design and improvement of electrochemical biosensors for e-skins as a diagnostic and sports performance assessment tool. In this frame, chapters 1 and 2 summarize the literature findings in terms of e-skins and biosensors. The latter, and in particular electrochemical biosensors, were deeply analyzed to underline their transduction principle as well as their current limitations.

The first application of the literature findings was applied in chapter 3. There, a prototype of a multi-sensing patch for unobtrusive and personalized fatigue assessment, that uses both an 8-channel electromyographic (EMG) sensor and an electrochemical sensor, is presented. The achieved results on both the sensors printed on the patch provided a promising starting point to pursue a device capable of monitoring the changes of EMG features and sweat lactate during fatigue processes. The variations recorded for the EMG features suggests the possibility of monitoring muscular fatigue over a large area. On the other hand, the results achieved with the lactate sensor are a promising starting point that suggest the feasibility of the proposed approach since the device was able to track lactate concentration changes within the physiological range of interest for fatigue. However, the achieved results showed that further inquiries were needed in order to optimize the sensor design and achieve better metrological characteristics. Starting from these initial cues, the next two projects focused on the scientific evidence to try to improve the sensitivity and the limit of detection of printed electrochemical sensors using both micro- and nano- structures.

The former solution was investigated in chapter 4 where aerosol jet printing was explored as a means to achieve a micro-structuration towards the third dimension. The proposed process was able to achieve linear micro-structures that permit increasing the electrode/electrolyte surface area up to 130% without changing the substrate occupancy. The achieved result showed that this solution increased the

sensitivity of the electrodes on an average of 2.3 times with respect to bare electrodes and thus it can be adopted in applications that require high sensitivity.

On the other hand, in chapter 5, the use of two nano-structured allotropes of carbon was explored as functionalization layers. The two selected materials were multi-walled carbon nanotubes (CNT) and graphene as they are widespread in industry, relatively cheap and are suitable in electrochemistry. The different tests that were carried out revealed that both of the sensors presented similar limits of detection (7.3 μM for CNT and 8.8 μM for graphene) and increased the electrode-electrolyte interface area up to over 100 times.

In the previous work where different nanostructures were evaluated, noise was observed to add uncertainty on the overall measured signal and introduce metrological issues. Thus, in order to better understand the quality and reliability of the proposed aerosol jet printed sensors, an in-depth analysis of the uncertainty sources related to the proposed devices was developed and proposed in the beginning of chapter 6. This allowed the definition of a wide set of uncertainty components that include high-frequency interference,those related to the instrumentation and the intrinsic noise of the sensor. At first, the well known noise of sample resistors was evaluated to estimate the noise introduced by the instrumentation and the external interferences. These results were then compared to the noise level obtained in the electrochemical experiments and it was possible to distinguish clearly the two components of noise. The obtained electrochemical noise was evaluated in the frequency spectrum by calculating its power spectral density. This showed clear evidence of the superposition of effects that generates a low frequency ($f < 0.9\ Hz$) plateau caused by both thermal and shot noise, while at higher frequencies, where the mass transport processes limit the noise spectrum, flicker noise is present. Since the former part of the spectrum underlined how the temperature is one of the most relevant components of noise and thus uncertainty on those kinds of sensors, its effects were better explored in a new experiment. This showed how the standard deviation of the measurements rose with the increase of temperature and how it acts as one of the main influence parameters that can change the average output current of the sensors.

This last result is alarming since the e-skins are exposed both to the body and to environmental temperature fluctuations, making it impossible to ensure a stable working temperature. Thus, to improve the reliability of these devices it is important to be able to compensate for the effects of temperature. To do so, a reliable, in-situ temperature measurement is required. Hence, a new set of temperature sensors, to be embedded in the e-skin device and in close proximity to the previously described electrochemical sensors, was analyzed pursuing two different research paths; at first two different geometries were analyzed and compared in order to decrease the surface occupancy of the devices as well as reduce their

sensibility to bending. The second research topic that was deepened regards the materials and their curing processes. In this latter work, both the macroscopic and microscopic characteristics were evaluated and compared in order to obtain relevant information to be used in the development of new and improved temperature sensors.

Despite the many results achieved and summarized in this work, many topics still require a deeper inquiry. Among them, other nanostructures and different kinds of microstructures could be explored to further optimize the metrological characteristics (e.g. sensitivity, LOD, ...) of the sensors. After that, a set of biorecognition elements with their suitable immobilization methods can be tested to widen the set of target analytes and improve the selectivity of the system. The next possible development of the research can be the integration of different sensors in a single electrochemical sensor array to provide better diagnostic and clinical information. Those arrays can then be translated to a proper e-skin device along with other sensors (e.g. temperature, pH, humidity, ...) that could be used to gather data in order to properly compensate for the influence variables. Lastly, an electronic front-end that interfaces and properly measures all the involved sensors could be implemented and characterized. Then, the electronic front-end could be engineered so as to be printed directly on the flexible substrate of the e-skin device in order to obtain a fully functional and integrated device.

Bibliography

[1] A. C. Bunea, V. Dediu, E. A. Laszlo, *et al.*, "E-skin: The dawn of a new era of on-body monitoring systems", *Micromachines*, vol. 12, no. 9, 2021, ISSN: 2072666X. DOI: 10.3390/mi12091091.

[2] H. S. Oh, C. H. Lee, N. K. Kim, T. An, and G. H. Kim, "Review: Sensors for biosignal/health monitoring in electronic skin", *Polymers*, vol. 13, no. 15, 2021, ISSN: 20734360. DOI: 10.3390/polym13152478.

[3] K. Guk, G. Han, J. Lim, *et al.*, "Evolution of wearable devices with real-time disease monitoring for personalized healthcare", *Nanomaterials*, vol. 9, no. 6, pp. 1–23, 2019, ISSN: 20794991. DOI: 10.3390/nano9060813.

[4] K. Kim, M. Jung, B. Kim, *et al.*, "Low-voltage, high-sensitivity and high-reliability bimodal sensor array with fully inkjet-printed flexible conducting electrode for low power consumption electronic skin", *Nano Energy*, vol. 41, no. June, pp. 301–307, 2017, ISSN: 22112855. DOI: 10.1016/j.nanoen.2017.09.024. [Online]. Available: http://dx.doi.org/10.1016/j.nanoen.2017.09.024.

[5] V. J. Lumelsky, M. S. Shur, and S. Wagner, "Sensitive skin", *IEEE Sensors Journal*, vol. 1, no. 1, pp. 41–51, 2001, ISSN: 1530437X. DOI: 10.1109/JSEN.2001.923586.

[6] S. Zhang, S. Li, Z. Xia, and K. Cai, "A review of electronic skin: Soft electronics and sensors for human health", *Journal of Materials Chemistry B*, vol. 8, no. 5, pp. 852–862, 2020, ISSN: 20507518. DOI: 10.1039/c9tb02531f.

[7] G. S. Cañón Bermúdez and D. Makarov, "Magnetosensitive E-Skins for Interactive Devices", *Advanced Functional Materials*, vol. 31, no. 39, 2021, ISSN: 16163028. DOI: 10.1002/adfm.202007788.

[8] W. D. Li, K. Ke, J. Jia, *et al.*, "Recent Advances in Multiresponsive Flexible Sensors towards E-skin: A Delicate Design for Versatile Sensing", *Small*, vol. 18, no. 7, pp. 1–41, 2022, ISSN: 16136829. DOI: 10.1002/smll.202103734.

[9] K. R. Nandanapalli, D. Mudusu, J. Bae, W. Jeong, G. D. Moon, and S. Lee, "Larger, flexible, and skin-mountable energy devices with graphene single layers for integratable, wearable, and health monitoring systems", *Materials Today Chemistry*, vol. 23, Mar. 2022, ISSN: 24685194. DOI: 10.1016/j.mtchem.2021.100764.

[10] D. J. Wilson, F. J. Martín-Martínez, and L. F. Deravi, "Wearable Light Sensors Based on Unique Features of a Natural Biochrome", *ACS Sensors*, vol. 7, no. 2, pp. 523–533, Feb. 2022, ISSN: 23793694. DOI: 10.1021/acssensors.1c02342.

[11] P. Escobedo, M. Ntagios, and R. Dahiya, "Electronic Skin with Energy Autonomous Proximity Sensing for Human-Robot Interaction", in *Proceedings of IEEE Sensors*, vol. 2020-Octob, Institute of Electrical and Electronics Engineers Inc., Oct. 2020, ISBN: 9781728168012. DOI: 10.1109/SENSORS47125.2020.9278896.

[12] G. Wolterink, R. Sanders, F. Muijzer, B. J. Van Beijnum, and G. Krijnen, "3D-printing soft sEMG sensing structures", in *Proceedings of IEEE Sensors*, vol. 2017-Decem, 2017, pp. 1–3, ISBN: 9781509010127. DOI: 10.1109/ICSENS.2017.8233935.

[13] P. S. Das and J. Y. Park, "A flexible touch sensor based on conductive elastomer for biopotential monitoring applications", *Biomedical Signal Processing and Control*, vol. 33, pp. 72–82, 2017, ISSN: 17468108. DOI: 10.1016/j.bspc.2016.11.008. [Online]. Available: http://dx.doi.org/10.1016/j.bspc.2016.11.008.

[14] P. Bifulco, D. Esposito, G. D. Gargiulo, *et al.*, "A stretchable, conductive rubber sensor to detect muscle contraction for prosthetic hand control", in *2017 E-Health and Bioengineering Conference, EHB 2017*, 2017, pp. 173–176, ISBN: 9781538603581. DOI: 10.1109/EHB.2017.7995389.

[15] L. Manjakkal, C. G. Nunez, and R. Dahiya, "Energy autonomous eSkin", SPIE-Intl Soc Optical Eng, May 2019, p. 55, ISBN: 9781510626294. DOI: 10.1117/12.2520757.

[16] M. Chung, G. Fortunato, and N. Radacsi, "Wearable flexible sweat sensors for healthcare monitoring: A review", *Journal of the Royal Society Interface*, vol. 16, no. 159, 2019, ISSN: 17425662. DOI: 10.1098/rsif.2019.0217.

[17] G. Xu, C. Cheng, W. Yuan, *et al.*, "Smartphone-based battery-free and flexible electrochemical patch for calcium and chloride ions detections in biofluids", *Sensors and Actuators, B: Chemical*, vol. 297, no. January, p. 126 743, 2019, ISSN: 09254005. DOI: 10.1016/j.snb.2019.126743. [Online]. Available: https://doi.org/10.1016/j.snb.2019.126743.

[18] X. Wang, L. Dong, H. Zhang, R. Yu, C. Pan, and Z. L. Wang, "Recent Progress in Electronic Skin", *Advanced Science*, vol. 2, no. 10, pp. 1–21, 2015, ISSN: 21983844. DOI: 10.1002/advs.201500169.

[19] M. Dehghani, K. J. Kim, and R. M. Dangelico, "Will smartwatches last? factors contributing to intention to keep using smart wearable technology", *Telematics and Informatics*, vol. 35, no. 2, pp. 480–490, 2018, ISSN: 07365853. DOI: 10.1016/j.tele.2018.01.007. [Online]. Available: https://doi.org/10.1016/j.tele.2018.01.007.

[20] S. Anastasova, B. Crewther, P. Bembnowicz, *et al.*, "A wearable multisensing patch for continuous sweat monitoring", *Biosensors and Bioelectronics*, vol. 93, no. June 2016, pp. 139–145, 2017, ISSN: 18734235. DOI: 10.1016/j.bios.2016.09.038. [Online]. Available: http://dx.doi.org/10.1016/j.bios.2016.09.038.

[21] M. Jose, G. Oudebrouckx, S. Bormans, P. Veske, R. Thoelen, and W. Deferme, "Monitoring Body Fluids in Textiles: Combining Impedance and Thermal Principles in a Printed, Wearable, and Washable Sensor", *ACS Sensors*, vol. 6, no. 3, pp. 896–907, 2021, ISSN: 23793694. DOI: 10.1021/acssensors.0c02037.

[22] B. Nie, S. Liu, Q. Qu, Y. Zhang, M. Zhao, and J. Liu, "Bio-inspired flexible electronics for smart E-skin", *Acta Biomaterialia*, vol. 139, pp. 280–295, 2022, ISSN: 18787568. DOI: 10.1016/j.actbio.2021.06.018.

[23] Q. Guo, X. Qiu, and X. Zhang, *Recent Advances in Electronic Skins with Multiple-Stimuli-Responsive and Self-Healing Abilities*, 2022. DOI: 10.3390/ma15051661.

[24] Y. Qiu, S. Sun, X. Wang, *et al.*, "Nondestructive identification of softness via bioinspired multisensory electronic skins integrated onarobotic hand", *npj Flexible Electronics*, vol. 6, no. 1, 2022, ISSN: 23974621. DOI: 10.1038/s41528-022-00181-9.

[25] S. Said, M. Sheikh, F. Al-Rashidi, *et al.*, "A customizable wearable robust 3d printed bionic arm: Muscle controlled", *BioSMART 2019 - Proceedings: 3rd International Conference on Bio-Engineering for Smart Technologies*, 2019. DOI: 10.1109/BIOSMART.2019.8734266.

[26] M. Wu, K. Yao, D. Li, *et al.*, "Self-powered skin electronics for energy harvesting and healthcare monitoring", *Materials Today Energy*, vol. 21, 2021, ISSN: 24686069. DOI: 10.1016/j.mtener.2021.100786.

[27] X. Wang, Y. Gu, Z. Xiong, Z. Cui, and T. Zhang, "Silk-molded flexible, ultrasensitive, and highly stable electronic skin for monitoring human physiological signals", *Advanced Materials*, vol. 26, no. 9, pp. 1336–1342, 2014, ISSN: 09359648. DOI: 10.1002/adma.201304248.

[28] A. Al-Halhouli, A. Albagdady, J. Alawadi, and M. A. Abeeleh, "Monitoring symptoms of infectious diseases: Perspectives for printed wearable sensors", *Micromachines*, vol. 12, no. 6, pp. 1–35, 2021, ISSN: 2072666X. DOI: 10.3390/mi12060620.

[29] F. Criscuolo, I. Ny Hanitra, S. Aiassa, *et al.*, "Wearable multifunctional sweat-sensing system for efficient healthcare monitoring", *Sensors and Actuators, B: Chemical*, vol. 328, no. June 2020, 2021, ISSN: 09254005. DOI: 10.1016/j.snb.2020.129017.

[30] P. C. Ferreira, V. N. Ataíde, C. L. Silva Chagas, *et al.*, "Wearable electrochemical sensors for forensic and clinical applications", *TrAC - Trends in Analytical Chemistry*, vol. 119, 2019, ISSN: 18793142. DOI: 10.1016/j.trac.2019.115622.

[31] K. K. Yeung, T. Huang, Y. Hua, K. Zhang, M. M. Yuen, and Z. Gao, "Recent Advances in Electrochemical Sensors for Wearable Sweat Monitoring: A Review", *IEEE Sensors Journal*, vol. 21, no. 13, pp. 14 522–14 539, 2021, ISSN: 15581748. DOI: 10.1109/JSEN.2021.3074311.

[32] K. H. Ha, H. Huh, Z. Li, and N. Lu, "Soft Capacitive Pressure Sensors: Trends, Challenges, and Perspectives", *ACS Nano*, vol. 16, no. 3, pp. 3442–3448, 2022, ISSN: 1936086X. DOI: 10.1021/acsnano.2c00308.

[33] U. Pierre Claver and G. Zhao, "Recent Progress in Flexible Pressure Sensors Based Electronic Skin", *Advanced Engineering Materials*, vol. 23, no. 5, pp. 1–17, 2021, ISSN: 15272648. DOI: 10.1002/adem.202001187.

[34] D. Son, J. Kang, O. Vardoulis, *et al.*, "An integrated self-healable electronic skin system fabricated via dynamic reconstruction of a nanostructured conducting network", *Nature Nanotechnology*, vol. 13, no. 11, pp. 1057–1065, 2018, ISSN: 17483395. DOI: 10.1038/s41565-018-0244-6. [Online]. Available: http://dx.doi.org/10.1038/s41565-018-0244-6.

[35] R. Nur, N. Matsuhisa, Z. Jiang, M. O. G. Nayeem, T. Yokota, and T. Someya, "A Highly Sensitive Capacitive-type Strain Sensor Using Wrinkled Ultrathin Gold Films", *Nano Letters*, vol. 18, no. 9, pp. 5610–5617, 2018, ISSN: 15306992. DOI: 10.1021/acs.nanolett.8b02088.

[36] M. Farooq and E. Sazonov, "Strain sensors in wearable devices", *Smart Sensors, Measurement and Instrumentation*, vol. 15, pp. 221–239, 2015, ISSN: 21948410. DOI: 10.1007/978-3-319-18191-2{_}9.

[37] Y. Zhao, Y. Liu, Y. Li, and Q. Hao, "Development and application of resistance strain force sensors", *Sensors (Switzerland)*, vol. 20, no. 20, pp. 1–18, 2020, ISSN: 14248220. DOI: 10.3390/s20205826.

[38] L. Y. Ma and N. Soin, "Recent Progress in Printed Physical Sensing Electronics for Wearable Health-Monitoring Devices: A Review", *IEEE Sensors Journal*, vol. 22, no. 5, pp. 3844–3859, 2022, ISSN: 15581748. DOI: 10.1109/JSEN.2022.3142328.

[39] H. S. Jeon, J. H. Kim, M. B. Jun, and Y. H. Jeong, "Fabrication of thermochromic membrane and its characteristics for fever detection", *Materials*, vol. 14, no. 13, 2021, ISSN: 19961944. DOI: 10.3390/ma14133460.

[40] Y. Zhang, B. Lin, R. Huang, *et al.*, "Flexible integrated sensing platform for monitoring wound temperature and predicting infection", *Microbial Biotechnology*, vol. 14, no. 4, pp. 1566–1579, 2021, ISSN: 17517915. DOI: 10.1111/1751-7915.13821.

[41] J. Chen, Y. Zhu, X. Chang, *et al.*, "Recent Progress in Essential Functions of Soft Electronic Skin", *Advanced Functional Materials*, vol. 31, no. 42, pp. 1–34, 2021, ISSN: 16163028. DOI: 10.1002/adfm.202104686.

[42] J. Chen, Y. Zhu, Z. Guo, and A. G. Nasibulin, "Recent progress on thermoelectrical properties of conductive polymer composites and their application in temperature sensors", *Engineered Science*, vol. 12, pp. 13–22, 2020, ISSN: 25769898. DOI: 10.30919/es8d1129.

[43] Q. Li, L. N. Zhang, X. M. Tao, and X. Ding, "Review of Flexible Temperature Sensing Networks for Wearable Physiological Monitoring", *Advanced Healthcare Materials*, vol. 6, no. 12, pp. 1–23, 2017, ISSN: 21922659. DOI: 10.1002/adhm.201601371.

[44] J. Polena, D. Afzal, J. H. Ngai, and Y. Li, "Temperature sensors based on organic field-effect transistors", *Chemosensors*, vol. 10, no. 1, 2022, ISSN: 22279040. DOI: 10.3390/chemosensors10010012.

[45] M. Kimura and K. Toshima, "Thermistor-like pn junction temperature-sensor with variable sensitivity and its combination with a micro-air-bridge heater", *Sensors and Actuators, A: Physical*, vol. 108, no. 1-3, pp. 239–243, 2003, ISSN: 09244247. DOI: 10.1016/S0924-4247(03)00290-5.

[46] J. Zhang, J. Li, W. Cheng, *et al.*, "Challenges in Materials and Devices of Electronic Skin", *ACS Materials Letters*, pp. 577–599, 2022, ISSN: 26394979. DOI: 10.1021/acsmaterialslett.1c00799.

[47] Y. Zhang, T. Zhang, Z. Huang, and J. Yang, "A New Class of Electronic Devices Based on Flexible Porous Substrates", *Advanced Science*, vol. 9, no. 7, pp. 1–39, 2022, ISSN: 21983844. DOI: 10.1002/advs.202105084.

[48] Z. Yuan, S. T. Han, W. Gao, and C. Pan, "Flexible and Stretchable Strategies for Electronic Skins: Materials, Structure, and Integration", *ACS Applied Electronic Materials*, vol. 4, no. 1, pp. 1–26, 2022, ISSN: 26376113. DOI: 10.1021/acsaelm.1c00025.

[49] J. Li, J. Liu, W. Huo, *et al.*, "Micro and nano materials and processing techniques for printed biodegradable electronics", *Materials Today Nano*, vol. 18, 2022, ISSN: 25888420. DOI: 10.1016/j.mtnano.2022.100201.

[50] A. Pajor-Świerzy, K. Szczepanowicz, A. Kamyshny, and S. Magdassi, "Metallic core-shell nanoparticles for conductive coatings and printing", *Advances in Colloid and Interface Science*, vol. 299, no. October 2021, 2022, ISSN: 00018686. DOI: 10.1016/j.cis.2021.102578.

[51] Y. Guo, X. Wei, S. Gao, W. Yue, Y. Li, and G. Shen, "Recent Advances in Carbon Material-Based Multifunctional Sensors and Their Applications in Electronic Skin Systems", *Advanced Functional Materials*, vol. 31, no. 40, 2021, ISSN: 16163028. DOI: 10.1002/adfm.202104288.

[52] Y. Kim, O. Y. Kweon, Y. Won, and J. H. Oh, "Deformable and Stretchable Electrodes for Soft Electronic Devices", *Macromolecular Research*, vol. 27, no. 7, pp. 625–639, 2019, ISSN: 20927673. DOI: 10.1007/s13233-019-7175-4.

[53] I. H. Cho, D. H. Kim, and S. Park, "Electrochemical biosensors: Perspective on functional nanomaterials for on-site analysis", *Biomaterials Research*, vol. 24, no. 1, pp. 1–12, 2020, ISSN: 20557124. DOI: 10.1186/s40824-019-0181-y.

[54] N. G. Di Novo, E. Cantù, S. Tonello, E. Sardini, and M. Serpelloni, "Support-material-free microfluidics on an electrochemical sensors platform by aerosol jet printing", eng, *Sensors (Switzerland)*, vol. 19, no. 8, Apr. 2019, ISSN: 14248220. DOI: 10.3390/s19081842.

[55] M. Serpelloni, E. Cantù, M. Borghetti, and E. Sardini, "Printed smart devices on cellulose-based materials by means of aerosol-jet printing and photonic curing", *Sensors (Switzerland)*, vol. 20, no. 3, 2020, ISSN: 14248220. DOI: 10.3390/s20030841.

[56] R. S. Mahale, S. Vasanth, H. Krishna, and S. Peramenahalli, "Sensor-Based Additive Manufacturing Technologies", vol. 12, no. 3, pp. 3513–3521, 2022.

[57] P. Bellitti, M. Borghetti, E. Cantu, E. Sardini, and M. Serpelloni, "Resistive Sensors for Smart Objects: Analysis on Printing Techniques", *IEEE Transactions on Instrumentation and Measurement*, vol. 71, 2022, ISSN: 15579662. DOI: 10.1109/TIM.2022.3181941.

[58] C. Xu, Y. Yang, and W. Gao, "Skin-Interfaced Sensors in Digital Medicine: from Materials to Applications", *Matter*, vol. 2, no. 6, pp. 1414–1445, 2020, ISSN: 25902385. DOI: 10.1016/j.matt.2020.03.020. [Online]. Available: https://doi.org/10.1016/j.matt.2020.03.020.

[59] J. C. Yang, J. Mun, S. Y. Kwon, S. Park, Z. Bao, and S. Park, "Electronic Skin: Recent Progress and Future Prospects for Skin-Attachable Devices for Health Monitoring, Robotics, and Prosthetics", *Advanced Materials*, vol. 31, no. 48, pp. 1–50, 2019, ISSN: 15214095. DOI: 10.1002/adma.201904765.

[60] M. Ha, S. Lim, and H. Ko, "Wearable and flexible sensors for user-interactive health-monitoring devices", *Journal of Materials Chemistry B*, vol. 6, no. 24, pp. 4043–4064, 2018, ISSN: 2050750X. DOI: 10.1039/c8tb01063c.

[61] S. Jo, D. Sung, S. Kim, and J. Koo, *A review of wearable biosensors for sweat analysis*, 2021. DOI: 10.1007/s13534-021-00191-y. [Online]. Available: https://doi.org/10.1007/s13534-021-00191-y.

[62] Y. Song, D. Mukasa, H. Zhang, and W. Gao, "Self-Powered Wearable Biosensors", *Accounts of Materials Research*, vol. 2, no. 3, pp. 184–197, 2021, ISSN: 26436728. DOI: 10.1021/accountsmr.1c00002.

[63] A. J. Bandodkar, I. Jeerapan, and J. Wang, "Wearable Chemical Sensors: Present Challenges and Future Prospects", *ACS Sensors*, vol. 1, no. 5, pp. 464–482, 2016, ISSN: 23793694. DOI: 10.1021/acssensors.6b00250.

[64] M. Dervisevic, M. Alba, B. Prieto-Simon, and N. H. Voelcker, "Skin in the diagnostics game: Wearable biosensor nano- and microsystems for medical diagnostics", *Nano Today*, vol. 30, p. 100 828, 2020, ISSN: 1878044X. DOI: 10.1016/j.nantod.2019.100828. [Online]. Available: https://doi.org/10.1016/j.nantod.2019.100828.

[65] J. Heikenfeld, A. Jajack, B. Feldman, *et al.*, "Accessing analytes in biofluids for peripheral biochemical monitoring", *Nature Biotechnology*, vol. 37, no. 4, pp. 407–419, 2019, ISSN: 15461696. DOI: 10.1038/s41587-019-0040-3. [Online]. Available: http://dx.doi.org/10.1038/s41587-019-0040-3.

[66] S. Tonello, G. Giorgi, C. Narduzzi, *et al.*, "Preliminary study of a flexible printed multi-sensing platform for electromyography and lactate measuring during rehabilitation", *2021 IEEE International Symposium on Medical Measurements and Applications, MeMeA 2021 - Conference Proceedings*, 2021. DOI: 10.1109/MeMeA52024.2021.9478729.

[67] K. Promsuwan, A. Soleh, K. Saisahas, *et al.*, "Micro-colloidal catalyst of palladium nanoparticles on polyaniline-coated carbon microspheres for a non-enzymatic hydrogen peroxide sensor", *Microchemical Journal*, vol. 171, no. August, p. 106 785, 2021, ISSN: 0026265X. DOI: 10.1016/j.microc.2021.106785. [Online]. Available: https://doi.org/10.1016/j.microc.2021.106785.

[68] M. Carbone, E. Aneggi, F. Figueredo, and S. Susmel, "NiO-nanoflowers decorating a plastic electrode for the non-enzymatic amperometric detection of H2O2 in milk: Old issue, new challenge", *Food Control*, vol. 132, no. June 2021, p. 108 549, 2022, ISSN: 09567135. DOI: 10.1016/j.foodcont.2021.108549. [Online]. Available: https://doi.org/10.1016/j.foodcont.2021.108549.

[69] S. G. Rhee, T. S. Chang, W. Jeong, and D. Kang, "Methods for detection and measurement of hydrogen peroxide inside and outside of cells", *Molecules and Cells*, vol. 29, no. 6, pp. 539–549, Jun. 2010, ISSN: 10168478. DOI: 10.1007/s10059-010-0082-3. [Online]. Available: http://link.springer.com/10.1007/s10059-010-0082-3.

[70] D. (U. Harvey, *Modren analytical chemistry*. 2000, p. 816, ISBN: 0-07-237547-7.

[71] P. V. Hornbeck, "Enzyme-linked immunosorbent assays", eng, in *Current Protocols in Immunology*, vol. 2015, Jan. 2015, pp. 1–2. DOI: 10.1002/0471142735.im0201s110.

[72] O. Coskun, "Separation Tecniques: CHROMATOGRAPHY", *Northern Clinics of Istanbul*, vol. 3, no. 2, pp. 156–160, 2016, ISSN: 21484902. DOI: 10.14744/nci.2016.32757.

[73] M. A. Morales and J. M. Halpern, "Guide to Selecting a Biorecognition Element for Biosensors", *Bioconjugate Chemistry*, vol. 29, no. 10, pp. 3231–3239, 2018, ISSN: 15204812. DOI: 10.1021/acs.bioconjchem.8b00592.

[74] H. Kumar and Neelam, "Enzyme-based electrochemical biosensors for food safety: a review", *Nanobiosensors in Disease Diagnosis*, p. 29, 2016. DOI: 10.2147/ndd.s64847.

[75] X. Tang, P. Y. Wang, and G. Buchter, "Ion-selective electrodes for detection of lead (Ii) in drinking water: A mini-review", *Environments - MDPI*, vol. 5, no. 9, pp. 1–14, 2018, ISSN: 20763298. DOI: 10.3390/environments5090095.

[76] S. Datta, L. R. Christena, and Y. R. S. Rajaram, "Enzyme immobilization: an overview on techniques and support materials", *3 Biotech*, vol. 3, no. 1, pp. 1–9, 2013, ISSN: 2190-572X. DOI: 10.1007/s13205-012-0071-7.

[77] V. Perumal and U. Hashim, *Advances in biosensors: Principle, architecture and applications*, 2014. DOI: 10.1016/j.jab.2013.02.001. [Online]. Available: http://dx.doi.org/10.1016/j.jab.2013.02.001.

[78] P. Damborský, J. Švitel, and J. Katrlík, "Optical biosensors", *Essays in Biochemistry*, vol. 60, no. 1, pp. 91–100, 2016, ISSN: 00711365. DOI: 10.1042/EBC20150010.

[79] M. Pohanka, *Overview of piezoelectric biosensors, immunosensors and DNA sensors and their applications*, 2018. DOI: 10.3390/ma11030448.

[80] A. J. Bard and L. R. Faulkner, *Electrochemical Methods: Fundamentals and Applications*, 2nd. Wiley, 2001.

[81] R. Seeber, C. Zanardi, and G. Inzelt, "The inherent coupling of charge transfer and mass transport processes: the curious electrochemical reversibility", *ChemTexts*, vol. 2, no. 2, 2016, ISSN: 21993793. DOI: 10.1007/s40828-016-0027-3.

[82] N. Elgrishi, K. J. Rountree, B. D. McCarthy, E. S. Rountree, T. T. Eisenhart, and J. L. Dempsey, "A Practical Beginner's Guide to Cyclic Voltammetry", *Journal of Chemical Education*, vol. 95, no. 2, pp. 197–206, 2018, ISSN: 19381328. DOI: 10.1021/acs.jchemed.7b00361.

[83] A. Kumar, S. K. Pahuja, and A. Singh, "Real time monitoring of muscle fatigue and muscle disorder of biceps brachii using Surface Electromyography (sEMG)", in *ICSCCC 2018 - 1st International Conference on Secure Cyber Computing and Communications*, 2018, pp. 401–405, ISBN: 9781538663738. DOI: 10.1109/ICSCCC.2018.8703279.

[84] J. J. Wan, Z. Qin, P. Y. Wang, Y. Sun, and X. Liu, *Muscle fatigue: General understanding and treatment*, 2017. DOI: 10.1038/emm.2017.194.

[85] G. Tartarisco, L. Billeci, G. Ricci, L. Volpi, G. Pioggia, and G. Siciliano, "A personal monitoring architecture to detect muscular fatigue in elderly", eng, *Neuromuscular Disorders*, vol. 22, no. SUPPL. 3, pp. 192–7, Dec. 2012, ISSN: 09608966. DOI: 10.1016/j.nmd.2012.10.009.

[86] G. Gugliandolo, G. Campobello, P. P. Capra, *et al.*, "A Movement-Tremors Recorder for Patients of Neurodegenerative Diseases", *IEEE Transactions on Instrumentation and Measurement*, vol. 68, no. 5, pp. 1451–1457, 2019, ISSN: 15579662. DOI: 10.1109/TIM.2019.2900141.

[87] P. Laferriere, E. D. Lemaire, and A. D. Chan, "Surface electromyographic signals using dry electrodes", in *IEEE Transactions on Instrumentation and Measurement*, vol. 60, 2011, pp. 3259–3268. DOI: 10.1109/TIM.2011.2164279.

[88] G. Theofilidis, G. C. Bogdanis, Y. Koutedakis, and C. Karatzaferi, "Monitoring exercise-induced muscle fatigue and adaptations: Making sense of popular or emerging indices and biomarkers", eng, *Sports*, vol. 6, no. 4, Nov. 2018, ISSN: 20754663. DOI: 10.3390/sports6040153.

[89] K. Sahlin, "Muscle fatigue and lactic acid accumulation", eng, *Acta Physiologica Scandinavica*, vol. 128, no. SUPPL. 556, pp. 83–91, 1986, ISSN: 00016772.

[90] A. J. M. Wagenmakers, "Role of Amino Acids and Ammonia in Mechanisms of Fatigue", in *Medicine and Sport Science*, 2015, pp. 69–86. DOI: 10.1159/000420983.

[91] J. J. Todd, "Lactate: Valuable for physical performance and maintenance of brain function during exercise", *Bioscience Horizons*, vol. 7, Jan. 2014, ISSN: 17547431. DOI: 10.1093/biohorizons/hzu001.

[92] D. A. Sakharov, M. U. Shkurnikov, M. Y. Vagin, E. I. Yashina, A. A. Karyakin, and A. G. Tonevitsky, "Relationship between lactate concentrations in active muscle sweat and whole blood", *Bulletin of Experimental Biology and Medicine*, vol. 150, no. 1, pp. 83–85, Jul. 2010, ISSN: 00074888. DOI: 10.1007/s10517-010-1075-0.

[93] C. Liu, F. Liu, L. Zhang, Y. Su, and A. Murray, "Smart Wearables in Healthcare: Signal Processing, Device Development, and Clinical Applications", *Journal of Healthcare Engineering*, vol. 2018, p. 1 696 924, 2018, ISSN: 20402309. DOI: 10.1155/2018/1696924.

[94] G. Marco, "Low cost inkjet printing for the fast prototyping of surface EMG detection systems", in *2015 IEEE International Symposium on Medical Measurements and Applications, MeMeA 2015 - Proceedings*, 2015, pp. 79–83, ISBN: 9781479964765. DOI: 10.1109/MeMeA.2015.7145176.

[95] S. Khan, S. Ali, and A. Bermak, *Recent developments in printing flexible and wearable sensing electronics for healthcare applications*, 2019. DOI: 10.3390/s19051230.

[96] D. R. Seshadri, R. T. Li, J. E. Voos, *et al.*, "Wearable sensors for monitoring the physiological and biochemical profile of the athlete", *npj Digital Medicine*, vol. 2, no. 1, p. 72, 2019, ISSN: 23986352. DOI: 10.1038/s41746-019-0150-9.

[97] P. A. Karthick, D. M. Ghosh, and S. Ramakrishnan, "Surface electromyography based muscle fatigue detection using high-resolution time-frequency methods and machine learning algorithms", *Computer Methods and Programs in Biomedicine*, vol. 154, pp. 45–56, Feb. 2018, ISSN: 18727565. DOI: 10.1016/j.cmpb.2017.10.024.

[98] H. C. Heitkamp and A. Hipp, "Lactate in cardiac rehabilitation. [German]", *Herz*, vol. 26, no. 7, pp. 447–453, Dec. 2001. [Online]. Available: http://ovidsp.ovid.com/ovidweb.cgi?T=JS&CSC=Y&NEWS=N&PAGE=fulltext&D=emed5&AN=2001414323%5Cnhttp://sfx.scholarsportal.info/uhn?sid=OVID:embase&id=pmid:&id=doi:&issn=0340-9937&isbn=&volume=26&issue=7&spage=447&pages=447-453&date=2001&title=Herz&atitle=Lact.

[99] E. Sardini, M. Serpelloni, and S. Tonello, "Printed electrochemical biosensors: Opportunities and metrological challenges", *Biosensors*, vol. 10, no. 11, 2020, ISSN: 20796374. DOI: 10.3390/bios10110166.

[100] E. Cantu, T. Fapanni, G. Giorgi, *et al.*, "Printed Multi-EMG Electrodes on the 3D Surface of an Orthosis for Rehabilitation: A Feasibility Study", *IEEE Sensors Journal*, vol. 21, no. 13, pp. 14 407–14 417, 2021, ISSN: 15581748. DOI: 10.1109/JSEN.2021.3059308.

[101] T. Fapanni, N. F. Lopomo, E. Sardini, and M. Serpelloni, "Novel Wearable System for Surface EMG Using Compact Electronic Board and Printed Matrix of Electrodes", in *Lecture Notes of the Institute for Computer Sciences, Social-Informatics and Telecommunications Engineering, LNICST*, vol. 360, 2021, pp. 55–60, ISBN: 9783030699628. DOI: 10.1007/978-3-030-69963-5{_}4.

[102] J. M. Andrade and M. G. Estévez-Pérez, "Statistical comparison of the slopes of two regression lines: A tutorial", *Analytica Chimica Acta*, vol. 838, pp. 1–12, 2014, ISSN: 18734324. DOI: 10.1016/j.aca.2014.04.057.

[103] A. Strazza, F. Verdini, L. Burattini, S. Fioretti, and F. Di Nardo, "Time-frequency analysis of surface EMG signals for maximum energy localization during walking", in *IFMBE Proceedings*, vol. 65, Jun. 2017, pp. 494–497, ISBN: 9789811051210. DOI: 10.1007/978-981-10-5122-7{_}124.

[104] A. Phinyomark, S. Thongpanja, H. Hu, P. Phukpattaranont, and C. Limsakul, "The Usefulness of Mean and Median Frequencies in Electromyography Analysis", in *Computational Intelligence in Electromyography Analysis - A Perspective on Current Applications and Future Challenges*, Oct. 2012, pp. 195–220, ISBN: 978-953-51-0805-4. DOI: 10.5772/50639.

[105] M. M. Radhi, E. A. Jaffar Al-Mulla, and W. T. Tan, "Electrochemical characterization of the redox couple of Fe(III)/Fe(II) mediated by grafted polymer electrode", *Research on Chemical Intermediates*, vol. 40, no. 1, pp. 179–192, 2014, ISSN: 09226168. DOI: 10.1007/s11164-012-0954-6.

[106] K. Rathee, V. Dhull, R. Dhull, and S. Singh, "Biosensors based on electrochemical lactate detection: A comprehensive review", *Biochemistry and Biophysics Reports*, vol. 5, pp. 35–54, 2016, ISSN: 24055808. DOI: 10.1016/j.bbrep.2015.11.010.

[107] M. E. Payne, A. Zamarayeva, V. I. Pister, N. A. Yamamoto, and A. C. Arias, "Printed, Flexible Lactate Sensors: Design Considerations Before Performing On-Body Measurements", *Scientific Reports*, vol. 9, no. 1, p. 13 720, 2019, ISSN: 20452322. DOI: 10.1038/s41598-019-49689-7.

[108] L. J. Currano, F. C. Sage, M. Hagedon, L. Hamilton, J. Patrone, and K. Gerasopoulos, "Wearable Sensor System for Detection of Lactate in Sweat", *Scientific Reports*, vol. 8, no. 1, p. 15 890, 2018, ISSN: 20452322. DOI: 10.1038/s41598-018-33565-x.

[109] E. V. Karpova, A. I. Laptev, E. A. Andreev, E. E. Karyakina, and A. A. Karyakin, "Relationship Between Sweat and Blood Lactate Levels During Exhaustive Physical Exercise", *ChemElectroChem*, vol. 7, no. 1, pp. 191–194, Jan. 2020, ISSN: 21960216. DOI: 10.1002/celc.201901703.

[110] S. Campuzano, M. Pedrero, M. Gamella, V. Serafín, P. Yáñez-Sedeño, and J. M. Pingarrón, "Beyond sensitive and selective electrochemical biosensors: Towards continuous, real-time, antibiofouling and calibration-free devices", *Sensors (Switzerland)*, vol. 20, no. 12, pp. 1–22, 2020, ISSN: 14248220. DOI: 10.3390/s20123376.

[111] A. S. Maghsoudi, S. Hassani, M. R. Akmal, *et al.*, "An electrochemical aptasensor platform based on flower-like gold microstructure-modified screen-printed carbon electrode for detection of serpin A12 as a type 2 diabetes biomarker", *International Journal of Nanomedicine*, vol. 15, pp. 2219–2230, 2020, ISSN: 11782013. DOI: 10.2147/IJN.S244315.

[112] X. Li, M. Xu, Q. Wu, W. Wei, and X. Liu, "Photolithographic 3D microarray electrode-based high-performance non-enzymatic H2O2 sensor", *Colloids and Surfaces A: Physicochemical and Engineering Aspects*, vol. 628, no. November 2020, p. 127 249, 2021, ISSN: 18734359. DOI: 10.1016/j.colsurfa.2021.127249. [Online]. Available: https://doi.org/10.1016/j.colsurfa.2021.127249.

[113] J. Krejci, Z. Sajdlova, V. Nedela, *et al.*, "Effective Surface Area of Electrochemical Sensors", *Journal of The Electrochemical Society*, vol. 161, no. 6, B147–B150, 2014, ISSN: 0013-4651. DOI: 10.1149/2.091406jes.

[114] K. Promsuwan, C. Kaewjunlakan, J. Saichanapan, *et al.*, "Poly(phenol red) hierarchical micro-structure interface enhanced electrode kinetics for adsorption and determination of hydroquinone", *Electrochimica Acta*, vol. 377, p. 138 072, 2021, ISSN: 00134686. DOI: 10.1016/j.electacta.2021.138072. [Online]. Available: https://doi.org/10.1016/j.electacta.2021.138072.

[115] B. Liu, C. Lv, C. Chen, *et al.*, "Electrochemical performance of micropillar array electrodes in microflows", *Micromachines*, vol. 11, no. 9, 2020, ISSN: 2072666X. DOI: 10.3390/MI11090858.

[116] C. Chen, B. Ran, Z. Wang, *et al.*, "Development of micropillar array electrodes for highly sensitive detection of biomarkers", *RSC Advances*, vol. 10, no. 67, pp. 41 110–41 119, 2020, ISSN: 20462069. DOI: 10.1039/d0ra07694e.

[117] J. Movilli, R. W. Kolkman, A. Rozzi, R. Corradini, L. I. Segerink, and J. Huskens, "Increasing the Sensitivity of Electrochemical DNA Detection by a Micropillar-Structured Biosensing Surface", *Langmuir*, vol. 36, no. 16, pp. 4272–4279, 2020, ISSN: 15205827. DOI: 10.1021/acs.langmuir.0c00144.

[118] T. Fapanni, E. Sardini, M. Serpelloni, and S. Tonello, "3D Electrochemical Sensor and Microstructuration Using Aerosol Jet Printing", *Sensors*, vol. 21, no. 23, 2021, ISSN: 14248220. DOI: 10.3390/s21237820.

[119] H. Gomathl, "CHEMISTRY AND ELECTROCHEMISTRY OF IRON COMPLEXES", *Ochemisfry*, vol. 16, no. 20, pp. 459–465, 2000.

[120] A. Morrin, A. J. Killard, and M. R. Smyth, "Electrochemical characterization of commercial and home-made screen-printed carbon electrodes", *Analytical Letters*, vol. 36, no. 9, pp. 2021–2039, 2003, ISSN: 00032719. DOI: 10.1081/AL-120023627.

[121] M. Majdinasab, M. Daneshi, and J. Louis Marty, "Recent developments in non-enzymatic (bio)sensors for detection of pesticide residues: Focusing on antibody, aptamer and molecularly imprinted polymer", *Talanta*, vol. 232, no. April, p. 122 397, 2021, ISSN: 00399140. DOI: 10.1016/j.talanta.2021.122397. [Online]. Available: https://doi.org/10.1016/j.talanta.2021.122397.

[122] H. Karimi-Maleh, F. Karimi, M. Alizadeh, and A. L. Sanati, "Electrochemical Sensors, a Bright Future in the Fabrication of Portable Kits in Analytical Systems", *Chemical Record*, vol. 20, no. 7, pp. 682–692, 2020, ISSN: 15280691. DOI: 10.1002/tcr.201900092.

[123] R. M. Trujillo, D. E. Barraza, M. L. Zamora, A. Cattani-Scholz, and R. E. Madrid, *Nanostructures in hydrogen peroxide sensing*, 2021. DOI: 10.3390/s21062204.

[124] Y. Zhou, C. W. Chiu, and H. Liang, "Interfacial structures and properties of organic materials for biosensors: An overview", *Sensors (Switzerland)*, vol. 12, no. 11, pp. 15 036–15 062, 2012, ISSN: 14248220. DOI: 10.3390/s121115036.

[125] W. He, X. Ye, and T. Cui, "Flexible Electrochemical Sensor with Graphene and Gold Nanoparticles to Detect Dopamine and Uric Acid", *IEEE Sensors Journal*, vol. 21, no. 23, pp. 26 556–26 565, 2021, ISSN: 15581748. DOI: 10.1109/JSEN.2021.3122326.

[126] M. F. Md Shakhih, A. S. Rosslan, A. Mohd Noor, S. Ramanathan, A. Mat Lazim, and A. Abdul Wahab, "Review—Enzymatic and Non-Enzymatic Electrochemical Sensor for Lactate Detection in Human Biofluids", *Journal of The Electrochemical Society*, 2021, ISSN: 0013-4651. DOI: 10.1149/1945-7111/ac0360.

[127] F. Mortazavi, N. Arab, and L. Fotouhi, "Signal Amplification Based on a Polymeric Film Decorated with Nanocomposites for Sensitive Determination of Propranolol in Biological and Pharmaceutical Samples", *IEEE Sensors Journal*, vol. 21, no. 18, pp. 20 850–20 856, 2021, ISSN: 15581748. DOI: 10.1109/JSEN.2021.3097384.

[128] X. Liu, Y. Zhou, J. Liu, and H. Xia, "The intrinsic enzyme mimetic activity of platinum oxide for biosensing of glucose", *Spectrochimica Acta - Part A: Molecular and Biomolecular Spectroscopy*, vol. 248, no. 9, p. 119 280, 2021, ISSN: 13861425. DOI: 10.1016/j.saa.2020.119280. [Online]. Available: https://doi.org/10.1016/j.saa.2020.119280.

[129] Y. Hu, M. Hojamberdiev, and D. Geng, "Recent advances in enzyme-free electrochemical hydrogen peroxide sensors based on carbon hybrid nanocomposites", *Journal of Materials Chemistry C*, vol. 9, no. 22, pp. 6970–6990, 2021, ISSN: 20507526. DOI: 10.1039/d1tc01053k.

[130] M. Eryigit, B. Kurt Urhan, H. O. Dogan, T. O. Ozer, and U. Demir, "ZnO Nanosheets-Decorated ERGO Layers: An Efficient Electrochemical Sensor for Non-Enzymatic Uric Acid Detection", *IEEE Sensors Journal*, vol. 22, no. 6, pp. 5555–5561, 2022, ISSN: 15581748. DOI: 10.1109/JSEN.2022.3150088.

[131] Y. S. Huang, K. Y. Chen, Y. T. Cheng, C. K. Lee, and H. E. Tsai, "An Inkjet-Printed Flexible Non-Enzymatic Lactate Sensor for Clinical Blood Plasma Test", *IEEE Electron Device Letters*, vol. 41, no. 4, pp. 597–600, 2020, ISSN: 15580563. DOI: 10.1109/LED.2020.2973343.

[132] N. Aliakbarinodehi, I. Taurino, J. Pravin, *et al.*, "Electrochemical nanostructured biosensors: Carbon nanotubes versus conductive and semi-conductive nanoparticles", *Chemical Papers*, vol. 69, no. 1, pp. 134–142, 2015, ISSN: 13369075. DOI: 10.1515/chempap-2015-0004.

[133] L. Fan, X. Ji, G. Lin, *et al.*, "Green synthesis of stable platinum nanoclusters with enhanced peroxidase-like activity for sensitive detection of glucose and glutathione", *Microchemical Journal*, vol. 166, no. March, p. 106 202, 2021, ISSN: 0026265X. DOI: 10.1016/j.microc.2021.106202. [Online]. Available: https://doi.org/10.1016/j.microc.2021.106202.

[134] Á. Torrinha, T. M. Oliveira, F. W. Ribeiro, A. N. Correia, P. Lima-Neto, and S. Morais, "Application of nanostructured carbon-based electrochemical (Bio)sensors for screening of emerging pharmaceutical pollutants in waters and aquatic species: A review", *Nanomaterials*, vol. 10, no. 7, pp. 1–29, 2020, ISSN: 20794991. DOI: 10.3390/nano10071268.

[135] D. C. Ferrier and K. C. Honeychurch, *Carbon nanotube (CNT)-based biosensors*, eng, Nov. 2021. DOI: 10.3390/bios11120486.

[136] F. Tiziano, S. Emilio, S. Mauro, and T. Sarah, "Nano-Functionalized Electrochemical Sensors by Aerosol Jet Printing", *IEEE Sensors Journal*, 2022. DOI: 10.1109/JSEN.2022.3213349.

[137] A. M. Faria, E. B. Peixoto, C. B. Adamo, A. Flacker, E. Longo, and T. Mazon, "Controlling parameters and characteristics of electrochemical biosensors for enhanced detection of 8-hydroxy-2-deoxyguanosine", *Scientific Reports*, vol. 9, no. 1, pp. 1–10, 2019, ISSN: 20452322. DOI: 10.1038/s41598-019-43680-y.

[138] M. Chen, H. Lee, J. Yang, *et al.*, "Parallel, Multi-Material Electrohydrodynamic 3D Nanoprinting", *Small*, vol. 16, no. 13, pp. 1–7, 2020, ISSN: 16136829. DOI: 10.1002/smll.201906402.

[139] S. Tonello, F. Stradolini, G. Abate, *et al.*, "Electrochemical detection of different p53 conformations by using nanostructured surfaces", *Scientific Reports*, vol. 9, no. 1, pp. 1–14, 2019, ISSN: 20452322. DOI: 10.1038/s41598-019-53994-6. [Online]. Available: http://dx.doi.org/10.1038/s41598-019-53994-6.

[140] G. Cho, S. Azzouzi, G. Zucchi, and B. Lebental, "Electrical and electrochemical sensors based on carbon nanotubes for the monitoring of chemicals in water—a review", *Sensors*, vol. 22, no. 1, 2022, ISSN: 14248220. DOI: 10.3390/s22010218.

[141] S. S. Ghoreishizadeh, G. Nanda, S. Carrara, and G. De Micheli, "Empirical study of noise dependence in electrochemical sensors", *Proceedings of the 2013 5th IEEE International Workshop on Advances in Sensors and Interfaces, IWASI 2013*, pp. 36–39, 2013. DOI: 10.1109/IWASI.2013.6576080.

[142] S. Mutyala and J. Mathiyarasu, "A reagentless non-enzymatic hydrogen peroxide sensor presented using electrochemically reduced graphene oxide modified glassy carbon electrode", *Materials Science and Engineering C*, vol. 69, pp. 398–406, 2016, ISSN: 09284931. DOI: 10.1016/j.msec.2016.06.069. [Online]. Available: http://dx.doi.org/10.1016/j.msec.2016.06.069.

[143] D. F. de Queiroz, T. R. d. L. Dadamos, S. A. S. Machado, and M. A. U. Martines, "Electrochemical determination of norepinephrine by means of modified glassy carbon electrodes with carbon nanotubes and magnetic nanoparticles of cobalt ferrite", *Sensors (Switzerland)*, vol. 18, no. 4, pp. 1–12, 2018, ISSN: 14248220. DOI: 10.3390/s18041223.

[144] Y. Lei, B. D. Ossonon, J. Chen, J. Perreault, and A. C. Tavares, "Electrochemical characterization of graphene-type materials obtained by electrochemical exfoliation of graphite", *Journal of Electroanalytical Chemistry*, vol. 887, no. August 2020, p. 115 084, 2021, ISSN: 15726657. DOI: 10.1016/j.jelechem.2021.115084. [Online]. Available: https://doi.org/10.1016/j.jelechem.2021.115084.

[145] A. Shrivastava and V. Gupta, "Methods for the determination of limit of detection and limit of quantitation of the analytical methods", *Chronicles of Young Scientists*, vol. 2, no. 1, p. 21, 2011, ISSN: 2229-5186. DOI: 10.4103/2229-5186.79345.

[146] Z. Miao, D. Zhang, and Q. Chen, "Non-enzymatic hydrogen peroxide sensors based on multi-wall carbon nanotube/Pt nanoparticle nanohybrids", *Materials*, vol. 7, no. 4, pp. 2945–2955, 2014, ISSN: 19961944. DOI: 10.3390/ma7042945.

[147] J. Ping, Y. Wang, K. Fan, J. Wu, and Y. Ying, "Direct electrochemical reduction of graphene oxide on ionic liquid doped screen-printed electrode and its electrochemical biosensing application", *Biosensors and Bioelectronics*, vol. 28, no. 1, pp. 204–209, 2011, ISSN: 09565663. DOI: 10.1016/j.bios.2011.07.018. [Online]. Available: http://dx.doi.org/10.1016/j.bios.2011.07.018.

[148] A. Hassibi, R. Navid, R. W. Dutton, and T. H. Lee, "Comprehensive study of noise processes in electrode electrolyte interfaces", *Journal of Applied Physics*, vol. 96, no. 2, pp. 1074–1082, 2004, ISSN: 00218979. DOI: 10.1063/1.1755429.

[149] S. Woo, Y. R. Kim, T. D. Chung, Y. Piao, and H. Kim, "Synthesis of a graphene-carbon nanotube composite and its electrochemical sensing of hydrogen peroxide", *Electrochimica Acta*, vol. 59, pp. 509–514, 2012, ISSN: 00134686. DOI: 10.1016/j.electacta.2011.11.012. [Online]. Available: http://dx.doi.org/10.1016/j.electacta.2011.11.012.

[150] K. Parate, C. C. Pola, S. V. Rangnekar, *et al.*, "Aerosol-jet-printed graphene electrochemical histamine sensors for food safety monitoring", *2D Materials*, vol. 7, no. 3, 2020, ISSN: 20531583. DOI: 10.1088/2053-1583/ab8919.

[151] E. Cantù, S. Tonello, G. Abate, D. Uberti, E. Sardini, and M. Serpelloni, "Aerosol jet printed 3D electrochemical sensors for protein detection", *Sensors (Switzerland)*, vol. 18, no. 11, pp. 1–14, 2018, ISSN: 14248220. DOI: 10.3390/s18113719.

[152] H. Lee, T. K. Choi, Y. B. Lee, *et al.*, "A graphene-based electrochemical device with thermoresponsive microneedles for diabetes monitoring and therapy", *Nature Nanotechnology*, vol. 11, no. 6, pp. 566–572, 2016, ISSN: 17483395. DOI: 10.1038/nnano.2016.38.

[153] T. Fapanni, "Uncertainty Sources in Aerosol Jet Printed and Flexible Electrochemical Sensors", IEEE, 2022, pp. 245–249, ISBN: 9781665410939.

[154] S. T. Larsen, M. L. Heien, and R. Taboryski, "Amperometric noise at thin film band electrodes", *Analytical Chemistry*, vol. 84, no. 18, pp. 7744–7749, 2012, ISSN: 00032700. DOI: 10.1021/ac301136x.

[155] L. Bahadori, M. H. Chakrabarti, N. S. A. Manan, *et al.*, "The Effect of Temperature on Kinetics and Diffusion Coefficients of Metallocene Derivatives in Polyol-Based Deep Eutectic Solvents", *PLoS ONE*, vol. 10, no. 12, 2015, ISSN: 19326203. DOI: 10.1371/journal.pone.0144235.

[156] D. Prasad and V. Nath, "An overview of temperature sensors", in *Lecture Notes in Electrical Engineering*, Mccs 2017, vol. 476, Springer Singapore, 2019, pp. 777–784, ISBN: 9789811082337. DOI: 10.1007/978-981-10-8234-4{_}62. [Online]. Available: http://dx.doi.org/10.1007/978-981-10-8234-4_62%20http://link.springer.com/10.1007/978-981-10-8234-4_62.

[157] F. Tiziano, E. Sardini, and M. Serpelloni, "A Preliminary Study on Flexible Temperature Sensors for Eskin Medical Devices", 2022.

[158] T. Dinh, H. P. Phan, A. Qamar, P. Woodfield, N. T. Nguyen, and D. V. Dao, "Thermoresistive Effect for Advanced Thermal Sensors: Fundamentals, Design Considerations, and Applications", *Journal of Microelectromechanical Systems*, vol. 26, no. 5, pp. 966–986, 2017, ISSN: 10577157. DOI: 10.1109/JMEMS.2017.2710354.

[159] M. Borghetti, E. Cantù, E. Sardini, and M. Serpelloni, "Future sensors for smart objects by printing technologies in Industry 4.0 scenario", *Energies*, vol. 13, no. 22, 2020, ISSN: 19961073. DOI: 10.3390/en13225916.

[160] M. T. Rahman, J. McCloy, C. V. Ramana, and R. Panat, "Structure, electrical characteristics, and high-temperature stability of aerosol jet printed silver nanoparticle films", *Journal of Applied Physics*, vol. 120, no. 7, 2016, ISSN: 10897550. DOI: 10.1063/1.4960779. [Online]. Available: http://dx.doi.org/10.1063/1.4960779.